Copyright

by

Michael Glen Weir

2010

The Dissertation Committee for Michael Glen Weir certifies that this is the approved version of the following dissertation:

Dendrimer-Encapsulated Nanoparticles: Synthetic Methods and Characterization Including Extended X-ray Absorption-Fine Structure

Committee:

_____

Richard M. Crooks, Supervisor

_____

Allen J. Bard

_____

Anatoly I. Frenkel

_____

Graeme Henkelman

_____

Keith Johnston

_____

Katherine Willets

Dendrimer-Encapsulated Nanoparticles: Synthetic Methods and Characterization Including Extended X-ray Absorption-Fine Structure

by

Michael Glen Weir, B. S.; M. S.

Dissertation

Presented to the Faculty of the Graduate School of

The University of Texas at Austin

in Partial Fulfillment

of the Requirements

for the Degree of

Doctor of Philosophy

The University of Texas at Austin

December, 2010

Acknowledgments

I would like to thank my research advisor, Dr. Richard M. Crooks, for his guidance and instruction over the past five years. He has opened my eyes to a deeper understanding of science, and tried to teach me many of the necessary skills for a successful career. I hope I have learned enough.

I would also like to thank Dr. Allen J. Bard, Dr. Katherine Willets, Dr. Graeme Henkelman, Dr. Keith Johnston, and Dr. Anatoly I. Frenkel for being my committee members. I learned about science from them, but also about the enthusiasm and curiosity that every scientist should have.

Dr. Marc R. Knecht and Mrs. V. Sue Myers were essential in this work for both experiments and ideas. The beamline experiments and my degree would not have happened without these two and our many stressful hours on the beamline. Dr. Nebojsa Marinkovic and Dr. Adele Wang were very helpful in assisting with the beamline optics.

Additional thanks go to Ms. Emily V. Carino, Mr. David F. Yancey, and the rest of the Crooks group for enlightening discussions and assistance in the laboratory.

Finally, I would like to thank my parents, Glen and Sylvia, for pushing me down the path toward chemistry and graduate school.

Dendrimer-Encapsulated Nanoparticles: Synthetic Methods and Characterization Including Extended X-ray Absorption-Fine Structure

Publication No._____

Michael Glen Weir, Ph. D.

The University of Texas at Austin, 2010

Supervisor: Richard M. Crooks

This work describes the synthesis of dendrimer-encapsulated nanoparticles (DENs) and the expansion of the characterization ability for these materials. The dendrimer-template method for the synthesis of nanoparticles allows precise control over the size, composition and structure of nanoparticles in the 40-250 atom range. In this size regime, the surface structure of

the nanoparticles dominates their catalytic properties. The long term goal of this research is to correlate the structure of these nanoparticles to their catalytic activity, improving the ability to predict superior catalysts a priori. As a prerequisite for this analysis, the precise structure of the catalytically active nanoparticle must be determined.

Characterization of nanoparticles in the 1-2 nm region is significantly more difficult than more commonly used nanoparticles of 3-5 nm diameter or larger. Typical characterization of these nanoparticles involves UV-vis spectroscopy for Mie absorbance and transmission electron microscopy for size analysis. This work involves the use of extended X-ray absorption-fine structure (EXAFS) to determine the local structure of the nanoparticles. For monometallic Pt DENs, EXAFS was combined with UV-vis, TEM, X-ray photoelectron spectroscopy (XPS) and electrochemistry to determine that the Pt system is not simply nanoparticles but a more complex, bimodal state.

EXAFS has also been used to differentiate between different bimetallic structures. For PdAu DENs, there are two synthetic methods used. When both metals are reduced

simultaneously, the resulting nanoparticles have a quasi-random alloy structure. These nanoparticles were then extracted from the dendrimer into an organic solvent by use of alkanethiols. The extraction process changed the alloy structure into Au-core/Pd-shell. When Pd and Au were reduced in sequence, the DENs were formed as a Au-core/Pd-shell material, regardless of the order of the reduction of the metals. The Au-core/Pd-shell structure was also present after extraction.

In addition to structural analysis to determine the result of different synthetic methods, EXAFS was also used *in situ* to measure the structure of Pt DENs during the oxidation of absorbed CO. These *in situ* measurements are important for determining the structure of the actual catalyst rather than the precursor nanoparticle. In this case, the Pt DENs changed from a bimodal distribution into fully reduced nanoparticles by the application of a reducing potential. The binding of CO to the Pt DENs and subsequent oxidation did not cause measurable agglomeration of the nanoparticles.

This reduction of the Pt system by electrochemical means was also explored as a synthetic method. The Pt-

dendrimer complex was placed on a TEM grid for electrochemical treatment. A potential step was shown to reduce some of the Pt-dendrimer complexes into Pt nanoparticles of the expected size. However, most of the complexes were not reduced. Therefore, only the standard chemical reduction followed by electrochemical treatment is sufficient to fully reduce the nanoparticle samples.

This work has explored additional synthetic methods for the synthesis of monometallic and bimetallic DENs. The use of EXAFS, as well as other advanced characterization techniques, has advanced knowledge of the structure of various DENs. Both the characterization toolset and the synthetic methods will provide a basis for investigations of catalytically active materials.

Table of Contents

List of Tables

List of Figures

List of Schemes

Chapter 1: Introduction

1.1 Dendrimer-Encapsulated Nanoparticles

The last 20 years have witnessed an explosion in the synthesis and use of nanoparticles.[1] This interest is due to the unique properties of nanoparticles beyond those of their bulk counterparts. Small differences in the size and composition of a particle can produce changes in the physical and chemical properties of the material. This is especially true for particles below 2 nm in diameter. For example, nanoparticles in this size range sometimes exhibit enhanced catalytic behavior.

Since it was first used in 1998, the dendrimer templating technique has proven to be one of the most versatile methods for producing well defined nanoparticles of a specific composition smaller than 2 nm.[2] The primary advantage of the DEN technique is the ability to synthesize well-defined nanoparticle systems. Significant focus has gone into careful characterization of the DEN product. This precise characterization is crucial to the larger goal of understanding nanoparticle size effects.

Dendrimers are a class of regular, highly branched, and highly symmetrical polymers. For further details on the broad field of dendrimer chemistry the reader is referred to a text published on the topic in 2009.[3] The generation of a dendrimer is the number of repeating branch points as traced from the dendrimer center to the periphery. Terminal functional groups of a dendrimer may be modified to control the solubility of the material. A dendrimer of generation n with a terminal functional group of R is notated Gn-R. The dendrimer most frequently used for the synthesis of DENs is poly(amidoamine) (PAMAM) dendrimer, although there have been several studies that utilize other dendrimer structures, most significantly poly(propylene imine) (PPI).[4]

In solution, there is significant pH dependent folding of the branches of the PAMAM dendrimer.[5] The terminal primary amines and interior tertiary amines can also be selectively protonated by pH modification. This can produce an electrostatic gradient between the dendrimer interior and surrounding solvent which may be important for sequestration of the metal ions. The mechanism of the complexation of metal ions to the dendrimer interior is

metal dependent and has been investigated in several theoretical[6-9] and empirical[10-13] studies.

Generally speaking, DENs are synthesized in a two-step process. First, metal ions are complexed to the dendrimer interior. The ratio of metallic precursor to dendrimer can be modified to control the size of the product nanoparticle. Second, the metal ions are reduced to form zerovalent particles encapsulated within the dendrimer structure. Bimetallic materials may be produced through co-complexation of the metal precursors or by complexing and reducing the second metal onto seed DENs of the first metal. Galvanic exchange of the metal nanoparticle by a more noble metal added to the solution has also been proposed as a method to produce bimetallic DENs. In this chapter, monometallic DENs are denoted Gn-R(A_x) and bimetallic DENs are denoted Gn-R(A_xB_y) where A and B are the metals used and x and y are the metal ion/dendrimer ratios used in the synthesis. Metal ion/dendrimer complexes are denoted Gn-R(A^{n+})$_x$ where n is the oxidation state of the metal.

DEN synthesis offers several advantages over other standard synthesis techniques. The size and composition of

the desired product may be easily selected by modification of the starting materials. After synthesis, the dendrimer shell prevents agglomeration of the metal particles. Importantly, it has been found that the dendrimer interacts weakly with the metal surface, leaving it open for catalysis and other surface reactions.[14,15] Modification of the terminal functional groups allows for tuning of the dendrimer solubility and provides a means of immobilization on a substrate. The dendrimer templating technique can produce particles in a size range not easily accessible to standard synthesis techniques. Finally, DENs are typically highly monodisperse in size.

To maintain a manageable length, the scope of this chapter has been limited to new synthesis and characterization techniques as well as to catalytic applications for DENs developed since a review article published in 2005.[4] Not included is the use of DENs for biological applications.[16,17] Dendrimer stabilized nanoparticles (DSNs) are also not included in this chapter. DSNs differ from DENs in that they are located external to the dendrimer and will have two or more dendrimers acting as capping agents.

1.2 Survey of DENs Research

Synthesis of New Materials. The materials for which the dendrimer encapsulation method has proven to be effective is continually expanding. As detailed in a previous report, DENs have been synthesized with a broad array of monometallic and bimetallic compositions and even one semiconductor material.[18] Recent advances include the expansion of the synthesis method to produce DENs in organic solvents and the use of the dendrimer encapsulation method to produce well-defined supported metal oxide particles.

Hydrophobic DENs

The synthesis of DENs in organic solvents allows DENs to be produced using reactive metals that would not be stable in aqueous media. In the previously mentioned review, the extraction of DENs into organic solvents by use of appropriate ligands, usually alkanethiols, was discussed. This extraction process removes the nanoparticle from the dendrimer and forms a monolayer protected cluster (MPC) (Scheme 1.1).[19,20] These MPCs have a metal center surrounded

by a protective layer of ligands. Similar materials prepared by direct reduction of the metal salt in the presence of alkanethiols have been studied extensively by Murray and others.[21] However, direct synthesis of the DENs in organic solvent has recently been achieved.[22] Hydrophobic dendrimers have been produced by modification of some of the terminal amine groups of PAMAM with dodecyl groups. Subsequent synthesis of DENs in these hydrophobic dendrimers avoids the restrictions of the aqueous system and maintains the high monodispersity which is a primary advantage of the dendrimer templating technique.

Knecht et al. synthesized Au DENs via direct dendrimer templating in G4-C_{12} in toluene.[22] Aqueous Au DENs had previously been characterized.[25] UV-vis and TEM indicate the organic-phase DENs are equivalent to the aqueous DENs. Additionally, organic-phase DENs were extracted from the hydrophobic dendrimer into an aqueous phase by use of tiopronin and glutathione. This synthesis established the general synthetic method used for more oxophilic metals.

Scheme 1.1

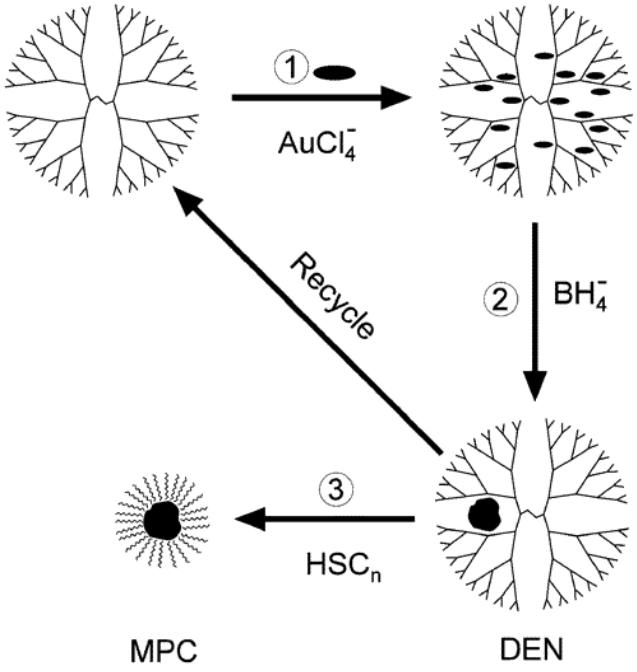

The hydrophobic dendrimer synthesis was applied to magnetic materials. Specifically, Ni[26] and Fe[27] were investigated. Both metals were protected from oxidation by water and oxygen by the toluene solvent and bubbling with N_2, respectively. The characterization of these materials was accomplished using UV-vis spectroscopy, TEM, and energy dispersive spectroscopy (EDS). Magnetic studies using SQUID revealed that the Ni DENs were ferromagnetic while the Fe particles vary from superparamagnetic to ferromagnetic depending on the particle size. These studies provide another example of dramatic changes in properties with a small change in nanoparticle size.

Characterization. Two of the advantages to DENs, their small size and their location in the interior of a bulky framework, make the materials very difficult to characterize. Often, characterization of new DEN materials will require state-of-the-art analytical techniques. During the last several years our group has focused on improving and expanding the instrumental techniques available to better define DEN systems. Structural probes of bimetallic materials and *in situ* measurements of the

materials are two areas of particular interest. Precise characterization of the nanoparticles is crucial to the understanding of size and structural effects on catalytic and other properties of the materials.

Structural

Structural characterization of DENs includes determining the crystallinity and degree of disorder in the materials as well as the nature and degree of mixing in bimetallic materials. In the later case, this means differentiating between core-shell and alloyed structures. Because catalytic reactions occur on particle surfaces, this is essential to understanding the catalytic properties of bimetallic materials. The small size of DENs precludes structural characterization techniques that require long range order. Extended X-ray Absorption Fine Structure (EXAFS) and X-ray Diffraction-Pair Distribution Function (XRD-PDF) are two techniques that can probe materials of this size.

EXAFS provides information about the local environment of an absorbing atom such as the number, type, and bond

distances of coordinating atoms. Because small nanoparticles have very high surface/interior atom ratios and because this ratio is highly size dependent, the total metal-metal coordination of a nanoparticle can be an estimate of particle size or shape. XRD-PDF measures the distribution of mass in a sample. The experimental PDF is given by the following relation.

(1) $$G(r) = 4\pi r(\rho(r)-\rho_0)$$

Where $\rho(r)$ and ρ_0 are the local and atomic number density. Experimental functions can be compared to theoretical structural models. G6-(Au_{147}) DENs were characterized by EXAFS and XRD-PDF. The first shell Au-Au coordination number (CN) was found to be 9.0(9) for a dried sample and 8.9(7) for a solution sample, close to the theoretical values of 8.98 and 9.09 for a 147 atom cuboctahedron and 140 atom truncated octahedron particle, respectively. Au-Au bond distances were measured at 2.832(6) Å and 2.836(4) Å for the dried and wet samples, slightly contracted from the bulk value of 2.87 Å. The XRD-PDF spectra are given in Figure 1.1. The nanoparticle spectra share features with the bulk Au data. However, the peaks are broadened and dampened at high r, indicating increased disorder and lack

of long range structure. It was found that highly ordered fcc structures could not be used to fit the experimental data. Reverse Monte Carlo simulations were used to determine structures consistent with the data. These models were then relaxed into more energetically stable configurations by DFT calculations. The resulting, disordered models approximated the data well.

The structural properties of Pt DENs were also investigated and discussed in Chapter 3. Briefly, the Pt DENs system was found to consist of two separate states: reduced particles and unreduced Pt^{2+}/dendrimer complexes. EXAFS is also a suitable probe to discern between various bimetallic structures. Core-shell and alloyed structures will have differentiable homo and hetero metal-metal CNs. So far, we have investigated the PdAu[33,34] and PdCu[35] systems. PdAu DENs synthesized by different methods are discussed in Chapters 4 and 5. One interesting but unexplained conclusion from this work is that the two synthetic methods have different endpoints for the nanoparticle structures.

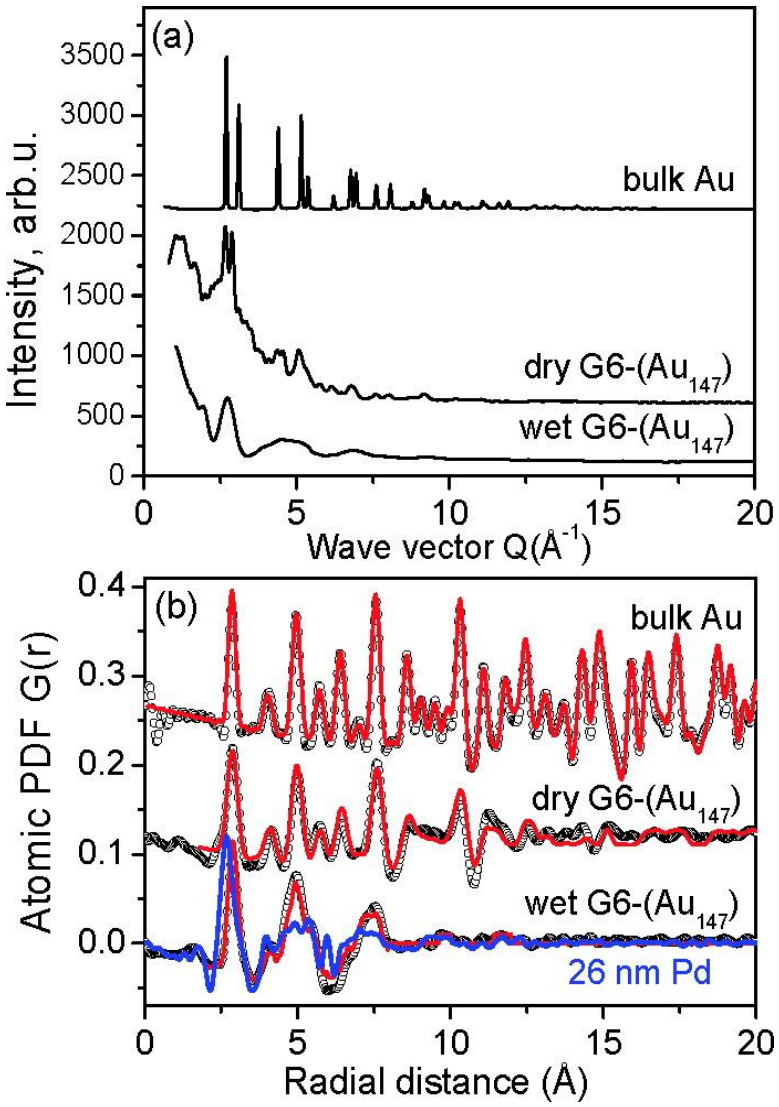

Figure 1.1. Experimental XRD (a) and the corresponding PDFs G(r) for 1.6-nm Au particles (b). Best model PDFs (red) and an experimental PDF for 26-nm Pd particles (in blue) are shown as well.

Encapsulation

One premise of the dendrimer templating technique is that by controlling the metal-ion-to-dendrimer complexation, it is possible to control the encapsulated nanoparticle. An assumption is that the encapsulated particles are largely isolated from each other by the dendrimer shell during and after reduction. Circumstantial evidence that the particles are located within the dendrimer and not at the dendrimer surface was given by an early TEM study of Au DENs in high generation dendrimers.[36]

High resolution NMR studies of Pd DENs also demonstrate that the particles are encapsulated to the interior of the dendrimer and indicate that the interaction between the dendrimer and the particle surface is relatively weak.[14] Figure 1.2 shows the methylene region of ^{1}H-NMR spectra of G4-OH, G4-OH$(Pd^{2+})_{55}$, and G4-OH(Pd_{55}) as well as the peak assignments of the PAMAM dendrimer structure. Peak assignments were made through a combination of ^{1}H, ^{1}H-^{1}H COSY, ^{1}H-^{15}N HMBC, ^{1}H-^{13}C HSQC, and ^{1}H-^{13}C HMBC NMR. As indicated in the figure, terminal methylene peaks are shifted slightly (and in the case of D/d peaks dramatically) from the overlapping internal

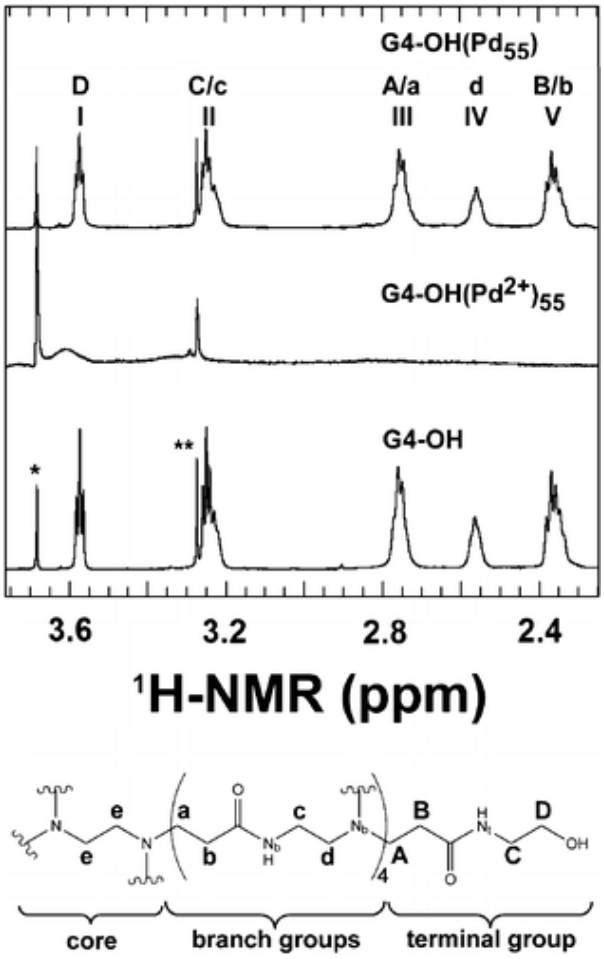

Figure 1.2. (Top) ^{1}H NMR spectra of G4-OH, G4-OH$(Pd^{2+})_{55}$, and G4-OH(Pd_{55}). The peak marked with a single asterisk arises from the dioxane internal standard, and the peak marked with a double asterisk arises from residual methanol. (Bottom) Schematic representation of G4-OH indicating the lettering scheme used to identify the methylene and nitrogen groups referred to in the text.

methylene peaks. Upon addition of Pd^{2+} salt to the dendrimer, nearly all of the ^{1}H peaks disappear. This is likely due to the breaking of the dendrimer symmetry by the complexed Pd. The spectrum after reduction is nearly identical to the pure dendrimer. However, upon careful examination it may be observed that the relative intensity of the internal methylene groups is lessened. This indicates a partial breaking of the symmetry inside of the dendrimer. If the Pd DEN is extracted from the dendrimer by short chain thiols, the peak intensities return to the initial free dendrimer values. This is strong evidence that the Pd particle is encapsulated by the dendrimer.

Pulsed-field gradient spin-echo NMR was also used to determine the hydrodynamic radius of the free dendrimer and of the DEN. In both instances it was measured as 1.7 ± 0.2 nm. This is further evidence that the particle is located to the dendrimer interior and that each particle is stabilized by one dendrimer.

The particle surface is not significantly passivated by the interior groups of the PAMAM dendrimer for many metal systems. Indirect evidence for this is given by the high catalytic rates achievable by DENs.[2,31] A recent EXAFS

study on G6-OH(Au_{147}) measured an upper limit of 15 N/O bonds to the surface of the 1.6(3) nm particles (as determined by TEM).[15] This indicates at least 84% of the surface remains unbound.

Size Probes

TEM is the standard method for measuring the size of DENs. Other standard nanocharacterization techniques for this size regime, e.g. AFM, are hindered by the presence of the dendrimer shell. TEM is an effective means for size determination; however, it suffers from two primary drawbacks. 1) For the smaller DEN materials, particularly those composed of lower mass elements, contrast is poor and imaging can be difficult. 2) TEM samples must be dried which excludes *in situ* studies. Furthermore, changes to the particles caused by the drying process remain a possibility.

As described in the previous section, the relative intensity of the internal functional group peaks in a DEN 1D ^{1}H-NMR spectrum are lessened by the presence of the metal particle. Gomez et al. found a correlation between the

particle size and the dampening of the signal.[37] They compared the D/d ratio (Figure 1.2) for G6-OH(Pd_n) (n = 55, 147, 200, 250) and found it scaled linearly with particle size. This method of characterization may provide useful for groups without access to a high resolution TEM. Furthermore, this experimental method may be modified to allow for *in-situ* characterization of the materials.

It has been demonstrated that size-monodisperse Au MPCs undergo quantized double layer capacitive charging that can serve as an accurate measure of particle size for small (< 5nm) particles.[38] Au particles 1.1 nm and smaller exhibit more complex, molecule-type behavior. The capacitive behavior of the MPCs results in a series of current peaks in Differential Pulse Voltammetry (DPV) whose spacing is given by the following relation.

(2) $$\Delta V = 4\pi\varepsilon\varepsilon_0(r/d)(r+d)$$

Where ε is the dielectric of the surrounding organic shell, r is the radius of the particle, and d is the length of the alkane thiol chain. Our group prepared Au DENs containing an average of 140 and 225 atoms and Pd DENs containing an

average of 40, 80, and 140 atoms. These materials were extracted to MPCs by *n*-hexanethiols (denoted MPC-6) and used without further purification. The calculated size and the experimental measurements (TEM and DPV) were in good agreement with the exception of the smallest Pd particles. MPC-6(Pd_{40}) was significantly larger as measured by TEM which may be an effect of the difficulty of resolving very small Pd particles in the TEM. Interestingly, the 1.1 nm Pd particles did not exhibit the molecular-type behavior of 1.1 nm Au particles.

Applications for Catalysis

Electrochemical

Electrochemical catalysis studies are a specialized form of heterogeneous catalysis where the catalyst is immobilized on an electrode surface. The DENs review discusses the attachment of DENs to planar electrode surfaces.[4] The dendritic architecture is an especially useful handle for attaching DENs to structures while preserving the both nanostructure and access to the nanoparticle surface.

The immobilization of DENs on planar electrodes has also facilitated studies on the relationship between nanostructure and properties on an atomic scale. The effects of nanoparticle size and compositions on kinetics and specific activities have been investigated. G6-OH(Pt_n) (n = 55, 100, 147, 200, 240) DENs were immobilized on glassy carbon rotating disk electrodes and used to catalyze the oxygen reduction reaction (ORR).[45] Rotating disk voltammetry (RDV) was used to obtain the mass-transfer limited current, and the kinetic current was found from the Koutecky-Levich equation. Interestingly, the smallest two

particles had decreased mass-transfer limited currents. This may indicate the two electron mechanism for ORR is significant for very small particles. Surface areas of the immobilized Pt DENs were obtained by CO stripping and H desorption and compared to theoretical calculations based on the surface area of the clusters and the expected monolayer coverage. The specific activities of the Pt DENs were found by dividing the kinetic current by the experimentally determined surface area. The specific activities of the Pt DENs were found to decrease with decreasing particle size.

This methodology was also tested on bimetallic PtPd DENs to deduce the effects of elemental composition on kinetics.[46] EDS of individual nanoparticles provided information about the elemental composition of the nanoparticles. The importance of this particular elemental analysis technique is worth noting. TEM images confirming particle monodispersity with subsequent EDS analysis of the visualized particles established that catalytic properties could be assigned to the DENs of given compositions. Analysis of the RDV of the PtPd DENs revealed three important results. Firstly, Tafel plots showed the ORR

mechanism was the same for PtPd DENs of varying elemental concentrations. Secondly, the atomic ratio of Pd in each bimetallic influenced the relative mass activity of Pt atoms for the ORR. The relative mass activity for Pt atoms in bimetallic DENs is found by normalizing the kinetic current to the fractional amount of Pt in the particle. Lastly, the Pt atoms in DENs containing Pd:Pt atomic ratios of 30:150 and 60:120 showed superior relative mass activities compared to the pure Pt DENs.

Stevenson and co-workers outfitted N-doped CNTs with Pt DENs in NH_3 terminated dendrimers and used the supported nanoparticles to catalyze the ORR.[47] After synthesis and characterization of CNTs and Pt DENs, they monitored the decrease in Pt DEN concentration in solution as DENs adsorbed to the CNTs by UV-vis following centrifugal separation of the CNT-supported DENs from Pt DENs remaining in the supernatant. Adsorption isotherms revealed that the affinity of the Pt DENs for adsorption increases with increasing edge-plane sites on the CNTs. This work is of considerable importance to the outfitting of nanomaterials' surfaces with DENs. In another study, G4-(Pd_{40}) DENs were adhered to chemically oxidized multiwalled carbon nanotubes

(MWNTs) through covalent attachment of the terminal amine groups to carboxyl groups on the MWNT. [48] These materials were found to be catalytically active for hydrazine oxidation.

1.3 Research Summary and Accomplishments

My dissertation focuses on the development of synthetic techniques for preparing DENs and the use of new characterization tools to determine their structure. The one tool central to this analysis is EXAFS. Chapter 3 describes the Pt DENs system. In this case, different characterization techniques gave seemingly incompatible results. Some techniques including UV-vis spectroscopy, XPS, and EXAFS indicated that there was more than one reduction state for the Pt ion-dendrimer complex. Other techniques such as TEM and XRD-PDF detected nanoparticles of the expected, fully reduced size. The combination of information led to the hypothesis of a bimodal distribution of reduced nanoparticles and unreduced complexes.

Chapters 4 and 5 represent the study of bimetallic nanoparticles using EXAFS. Chapter 4 describes the

synthesis of PdAu nanoparticles by simultaneous reduction of the two metals. In this case the DENs were found to take an alloy structure. When extracting the nanoparticles from the protective dendrimer into an organic phase using alkanethiols, the particles changed structure to a Au@Pd core-shell structure.

Chapter 5 covers the sequential reduction of the two metals for the PdAu system. Regardless of the order of reduction, the DENs form a Au@Pd core-shell structure. This structure was stable upon reduction. The catalysis of resazurin to resorufin on Au was investigated as a probe of surface structure. The catalytic results agree with the EXAFS results.

Chapter 6 returns to the Pt DENs system. An in-situ cell was developed to measure the structure of the Pt DENs during electrocatalytic oxidation of CO. The in-situ experiments are important to determine whether the catalyst material is the same as that characterized ex-situ. The CO oxidation experiment was chosen for its control of the reaction rate on the time scale needed for EXAFS measurements (hours). The Pt DENs were found to fully reduce on the application of a reducing potential.

Further, this reduced state was stable during the immobilization of CO on the Pt surface and its subsequent oxidation. This in-situ measurement identifies the active catalytic structure for the Pt DENs system.

References

1. Foss, C. A., Jr.; Feldheim, D. L. *Metal Nanoparticles: Synthesis Characterization & Applications* Marcel Dekker: New York, 2002.

2. Zhao, M.; Sun, L.; Crooks, R. M. *J. Am. Chem. Soc.* **1998**, *120*, 4877-4878.

3. Vögtle, F.; Richardt, G.; Werner, N. *Dendrimer Chemistry: Concepts, Syntheses, Properties, Applications*. Wiley-VCH: Weinheim, 2009.

4. Scott, R. W. J.; Wilson, O. M.; Crooks, R. M. *J. Phys. Chem. B* **2005**, *109*, 692-704.

5. Liu, Y.; Bryantsev, V. S.; Diallo, M. S.; Goddard Iii, W. A. *J. Am. Chem. Soc.* **2009**, *131*, 2798-2799.

6. Tarazona-Vasquez, F.; Balbuena, P. B. *J. Phys. Chem. B* **2008**, *112*, 4172-4181.

7. Tarazona-Vasquez, F.; Balbuena, P. B. *J. Phys. Chem. B* **2008**, *112*, 4182-4193.

8. Sun, L.; Crooks, R. M. *J. Phys. Chem. B* **2002**, *106*, 5864-5872.

9. Tarazona-Vasquez, F.; Balbuena, P. B. *J. Phys. Chem. B* **2005**, *109*, 12480-12490.

10. Krot, K. A.; de Namor, A. F. D.; Aguilar-Cornejo, A.; Nolan, K. B. *Inorg. Chim. Acta* **2005**, *358*, 3497-3505.

11. Tran, M. L.; Gahan, L. R.; Gentle, I. R. *J. Phys. Chem. B* **2004**, *108*, 20130-20136.

12. Alexeev, O. S.; Siani, A.; Lafaye, G.; Williams, C. T.; Ploehn, H. J.; Amiridis, M. D. *J. Phys. Chem. B* **2006**, *110*, 24903-24914.

13. Diallo, M. S.; Christie, S.; Swaminathan, P.; Balogh, L.; Shi, X.; Um, W.; Papelis, C.; Goddard, W. A.; Johnson, J. H. *Langmuir* **2004**, *20*, 2640-2651.

14. Gomez, M. V.; Guerra, J.; Velders, A. H.; Crooks, R. M. *J. Am. Chem. Soc.* **2009**, *131*, 341-350.

15. Petkov, V.; Bedford, N.; Knecht, M. R.; Weir, M. G.; Crooks, R. M.; Tang, W.; Henkelman, G.; Frenkel, A. *J. Phys. Chem. C* **2008**, *112*, 8907-8911.

16. Xiangyang, S.; Su He, W.; Inhan, L.; Mingwu, S.; James, R. B., Jr. *Biopolymers* **2009**, *91*, 936-942.

17. Shi, X.; Wang, S. H.; Shen, M.; Antwerp, M. E.; Chen, X.; Li, C.; Petersen, E. J.; Huang, Q.; Weber, W. J.; Baker, J. R. *Biomacromolecules* **2009**, *10*, 1744-1750.

18. Lemon, B. I.; Crooks, R. M. *J. Am. Chem. Soc.* **2000**, *122*, 12886-12887.

19. Garcia-Martinez, J. C.; Scott, R. W. J.; Crooks, R. M. *J. Am. Chem. Soc.* **2003**, *125*, 11190-11191.

20. Garcia-Martinez, J. C.; Crooks, R. M. *J. Am. Chem. Soc.* **2004**, *126*, 16170-16178.

21. Templeton, A. C.; Wuelfing, W. P.; Murray, R. W. *Acc. Chem. Res.* **1999**, *33*, 27-36.

22. Knecht, M. R.; Garcia-Martinez, J. C.; Crooks, R. M.. *Langmuir* **2005**, *21*, 11981-11986.

23. Niu, Y.; Crooks, R. M. *Chem. Mater.* **2003**, *15*, 3463-3467.

24. Yeung, L. K.; Crooks, R. M. *Nano Lett.* **2000**, *1*, 14-17.

25. Kim, Y. G.; Oh, S. K.; Crooks, R. M. *Chem. Mater.* **2004**, *16*, 167-172.

26. Knecht, M. R.; Garcia-Martinez, J. C.; Crooks, R. M. *Chem. Mater.* **2006**, *18*, 5039-5044.

27. Knecht, M. R.; Crooks, R. M. *New J. Chem* **2007**, *31*, 1349-1353.

28. Satoh, N.; Nakashima, T.; Kamikura, K.; Yamamoto, K. *Nat. Nano* **2008**, *3*, 106-111.

29. Knecht, M. R.; Weir, M. G.; Myers, V. S.; Pyrz, W. D.; Ye, H.; Petkov, V.; Buttrey, D. J.; Frenkel, A. I.; Crooks, R. M. *Chem. Mater.* **2008**, *20*, 5218-5228.

30. Ozturk, O.; Black, T. J.; Perrine, K.; Pizzolato, K.; Williams, C. T.; Parsons, F. W.; Ratliff, J. S.; Gao, J.; Murphy, C. J.; Xie, H.; Ploehn, H. J.; Chen, D. A. *Langmuir* **2005**, *21*, 3998-4006.

31. Ye, H.; Crooks, R. M. *J. Am. Chem. Soc.* **2005**, *127*, 4930-4934.

32. Zhao, M.; Crooks, R. M. *Adv. Mater.* **1999**, *11*, 217-220.

33. Knecht, M. R.; Weir, M. G.; Frenkel, A. I.; Crooks, R. M. *Chem. Mater.* **2008**, *20*, 1019-1028.

34. Weir, M. G.; Knecht, M. R.; Frenkel, A. I.; Crooks, R. M. *Langmuir* **2009**.

35. Myers, S. V.; Frenkel, A. I.; Crooks, R. M. *Chem. Mater.* **2009**, *21*, 4824-4829.

36. Grohn, F.; Bauer, B. J.; Akpalu, Y. A.; Jackson, C. L.; Amis, E. J. *Macromolecules* **2000**, *33*, 6042-6050.

37. Gomez, M. V.; Guerra, J.; Myers, V. S.; Crooks, R. M.; Velders, A. H. *J. Am. Chem. Soc.* **2009**, *131*, 14634-14635.

38. Murray, R. W. *Chem. Rev.* **2008**, *108*, 2688-2720.

39. Wilson, O. M.; Knecht, M. R.; Garcia-Martinez, J. C.; Crooks, R. M. *J. Am. Chem. Soc.* **2006**, *128*, 4510-4511.

40. Bernechea, M. a.; de Jesus, E.; Lopez-Mardomingo, C.; Terreros, P. *Inorg. Chem.* **2009**, *48*, 4491-4496.

41. Carino, E. V.; Knecht, M. R.; Crooks, R. M. *Langmuir* **2009**, *25*, 10279-10284.

42. Lang, H.; May, R. A.; Iversen, B. L.; Chandler, B. D. *J. Am. Chem. Soc.* **2003**, *125*, 14832-14836.

43. Lafaye, G.; Siani, A.; Marecot, P.; Amiridis, M. D.; Williams, C. T. *J. Phys. Chem. B* **2006**, *110*, 7725-7731.

44. Huang, W.; Kuhn, J. N.; Tsung, C.-K.; Zhang, Y.; Habas, S. E.; Yang, P.; Somorjai, G. A. *Nano Lett.* **2008**, *8*, 2027-2034.

45. Ye, H.; Crooks, J. A.; Crooks, R. M. *Langmuir* **2007**, *23*, 11901-11906.

46. Ye, H.; Crooks, R. M. *J. Am. Chem. Soc.* **2007**, *129*, 3627-3633.

47. Vijayaraghavan, G.; Stevenson, K. J. *Langmuir* **2007**, *23*, 5279-5282.

48. Shen, Y.; Xu, Q.; Gao, H.; Zhu, N. *Electrochem. Commun.* **2009**, *11*, 1329-1332.

Chapter 2: Experimental

2.1 Chemicals

All chemicals used in this work are described in the appropriate individual chapters.

2.2 Techniques

Beam Optics on X18B: Alignment for EXAFS

The alignment of the beam optics for synchrotron based analytical techniques is a necessary precursor to experimentation and can be the difference between acceptable and unusable signal to noise. This alignment procedure is specific to beamline X18B at the National Synchrotron Light Source at Brookhaven National Lab.

The first step in beginning the beam alignment is to determine what energies are needed for the intended experiments. While Pt (11.565 keV L_3) and Au (11.919 keV L_3) are virtually identical, measuring Cu (8.979 keV K) or Pd (24.35 keV K) may require more adjustments. Either the K or L_3 edge should be chosen to be in the range of 7 – 30

keV. After this, the monochromater angle should be adjusted so that the proper energies are available. On the lower end, as little as 200 eV below the lowest edge can be used, but 500 eV is preferred. The higher end of the energy range requires as much as 2 keV above the edge, as the fine structure information is at a higher energy than the edge jump. These constants, and other beamline specific measurements, can be found in manuals at the beamline.

Before further alignment, the detectors must be prepared and operating. These detectors are found inside the hutch, the experimental area which is walled to protect the user from scattered X-rays. Typical X-ray detectors are a 30 cm gas-ion chamber. A high voltage power source is attached across the chamber. As X-rays enter the chamber, they will ionize the gas inside, allowing a current to flow. This current is amplified and becomes the detector signal. The gas chosen for each detector is dependent on the energy used and the position of the detector. The first detector (I_o) is chosen so that ~10% of the X-rays are absorbed in the chamber. The second detector (I_t) is placed in series with the first, but behind

the sample. This detector should absorb ~70% of the incident X-rays. These two detectors are the basis of a transmission measurement. The first detector absorbs fewer X-rays so that the sample is strongly illuminated. The second detector absorbs a greater percentage as some of the X-rays will be absorbed or scattered by the sample and the first detector. The final detector in series is generally placed behind the reference foil and contains flowing Ar. This detector is not adjusted, as the reference foil has a strong signal and is only used for energy alignment.

Once the detectors are filled with the appropriate gas and placed in position, the remaining beamline optics can be aligned. The white slit is closest to the synchrotron and is upstream of the monochromater. A reference foil of the appropriate element is placed at the sample position in the beamline. Then the hutch slits are opened vertically so that optics further upstream may be adjusted. The first slit is the white slit and is adjusted to a width dependent on the energy. This width may range from 0.1 to 1.5 mm. The slit helps define the energy resolution by limiting both intrinsic and extrinsic energy broadening, and therefore is chosen to be the widest possible that

maintains energy resolution. The position of the slit is adjusted so that the beam is centered in the slit.

The silicon crystals of the monochromater are then detuned, or removed from parallel alignment. The two crystals are adjusted until they are fully aligned/parallel (highest signal in I_0). At this point, the chosen wavelength is transmitted, but higher harmonics of this wavelength are also present. These higher harmonics have a greater relative effect for lower chosen energies, as the intensity of the X-ray beam from the synchrotron peaks at ~ 7 keV. Therefore, the intensity of the higher harmonics for lower chosen energies will be higher than the intensity of the equivalent harmonics for a higher chosen energy. The silicon crystals are detuned until the signal in I_0 is lowered to an energy dependent percentage of the original value. For Pt or Au, this is typically 80% while Pd is not detuned. The Pd edge is at a high enough energy that any higher harmonics are negligible.

Finally, the hutch slits are closed vertically and symmetrically until each edge reduces the total intensity at I_0 by 10%. These slits are closed to define the size of the X-ray beam on the sample. At this point, the sample

position is adjusted both vertically and horizontally for the specific experimental apparatus. The beamline is ready to use.

Chapter 3: Synthesis and Characterization of Pt Dendrimer-Encapsulated Nanoparticles: Effect of the Template on Nanoparticle Formation

3.1 Synopsis

In this chapter, we provide a detailed description of the synthesis and properties of Pt dendrimer-encapsulated nanoparticles (DENs) prepared using sixth-generation, hydroxyl-terminated, PAMAM dendrimers (G6-OH) and three different $PtCl_4^{2-}$:G6-OH ratios: 55, 147, and 240. Results obtained from UV-vis spectroscopy, X-ray photoelectron spectroscopy, electron microscopy, X-ray absorption spectroscopy, and high-energy X-ray diffraction show that a relatively small percentage of the Pt^{2+}/dendrimer precursors are reduced by BH_4^- and that the reduction process is highly heterogeneous. That is, after reduction each Pt^{2+}/dendrimer precursor complex is either fully reduced, to yield a DEN having a size and structure consistent with the original $PtCl_4^{2-}$:dendrimer ratio used for the synthesis, or the precursor is not reduced at all. This result is consistent

with an autocatalytic process that entails slow formation of a nascent catalytic Pt seed within the dendrimer, followed by rapid, catalytic reduction of nearby Pt^{2+} ions. Details concerning the formation of the Pt^{2+}/dendrimer precursor are also discussed.

3.2 Introduction

We report the atomic-level physical characterization of Pt dendrimer-encapsulated nanoparticles (DENs)[1] with an emphasis on the relationship between the Pt^{2+}/dendrimer composite starting material and the structural properties of the corresponding DENs. Here, Pt^{2+} refers to any form of Pt^{2+} regardless of its ligand field. This is a timely study, because it has recently been found that the use of slightly different synthetic methods for preparing Pt DENs leads to different products.[2-5] The purpose of this chapter is to reconcile these reports using a combination of time-resolved UV-vis spectroscopy, X-ray photoelectron spectroscopy (XPS), high-resolution transmission electron microscopy (HRTEM), extended x-ray absorption fine structure (EXAFS) spectroscopy, and high-energy x-ray diffraction (XRD) coupled with pair-distribution function

analysis (PDF). The combination of these analytical methods, which provide complementary information, is important because DENs are good models for studying the effect of nanoparticle size, composition, and structure on catalytic activity.[6-17] However, to extract useful correlations of this sort, it is necessary that there be consensus on the DEN structure.

The key findings of this study are as follows. First, time-resolved UV-vis spectroscopy indicates that the Pt species required for dendrimer binding is $PtCl_n(H_20)_{4-n}^{2-n}$, where $n < 4$. Second, the UV-vis and XPS data indicate that reduction of the Pt^{2+}/dendrimer complexes with BH_4^- is incomplete. Third, EXAFS results indicate relatively low Pt-Pt coordination numbers (CNs) that are consistent with the UV-vis and XPS data. Fourth, HRTEM and XRD/PDF analyses indicate that Pt DENs possess a face-centered cubic (fcc)-type structure and sizes that correlate very well to the initial $PtCl_4^{2-}$:dendrimer ratio used for the synthesis. To summarize, results obtained from TEM and XRD/PDF indicate the presence of fully reduced Pt DENs, while UV-vis, XPS, and EXAFS spectroscopic data are consistent with incomplete reduction of the Pt^{2+}/dendrimer precursors. Here we show how these seemingly inconsistent results can be unified

with a single model that invokes a bimodal distribution of products.

The DEN synthesis is carried out in two steps. First, metal ions are introduced to a solution of dendrimers, which results in complexation of the ions with interior tertiary amines of the dendrimer. Second, the encapsulated metal ions are chemically reduced, which usually results in formation of zerovalent DENs. Using this method, monometallic DENs (Au, Pd, Pt, Cu, Ag, Ni, and Fe),[1,13,15,18-26] bimetallic alloy and core-shell DENs (PdPt, PdAu, AuAg, and PtCu),[7,10,12,27-30] and semiconducting quantum dots (CdS) have been prepared.[31] These materials, which range in size from just a few atoms[32,33] to perhaps 1000 atoms, are often nearly monodisperse in size, composition, and structure.[6-13,34,35] Moreover, because the dendrimers are highly permeable and do not passivate the surface of the encapsulated nanoparticles, DENs are also good model catalysts.[1,6,12]

There are some interesting differences between Pt DENs and other monometallic DENs.[3,5,34] Most notably, the Pt DEN synthesis requires a significantly longer period of time to complete (~4 d) compared to other types of DENs (typically ~1 h).[18,19] On the basis of several recent reports, we

believe the rate-limiting process in the DEN synthesis is complexation between Pt^{2+} and tertiary amines within the dendrimer.[2,4,5,34,36] $PtCl_4^{2-}$ is typically the source of Pt^{2+} for the synthesis of Pt DENs, and in this case the complexation process likely involves two steps: water substitution of one or more Pt-Cl bonds followed by Pt-amine bond formation. Murphy and coworkers have reported NMR data suggesting the presence of numerous mono- and bidentate binding motifs between Pt^{2+} and sites within second- and fourth-generation, hydroxyl-terminated PAMAM dendrimers (G2-OH and G4-OH, respectively).[36] We believe their model is generally correct, but they did not invoke the $PtCl_4^{2-}$ ligand exchange step which we will show here to be a requirement for complexation. Indeed, this sequence of reactions (Pt-Cl bond exchange for water followed by reaction with an amine) has been previously observed for related compounds.[37,38] Recent EXAFS results from Amiridis and coworkers have provided support for the NMR results.[5] This group also studied the reactivity of $PtCl_4^{2-}$ with water in the absence of dendrimer, and interpreted the results in terms of ligand substitution of two Pt-Cl bonds.[5]

Another aspect of the Pt DEN synthesis that distinguishes it from other types of DENs is that a larger

excess of reductant (BH_4^-) is required and that the reduction must be carried out in a sealed container.[3] These requirements are necessary to ensure that a partial pressure of H_2, which is a by-product of the aqueous BH_4^- reduction step, is retained within the reaction vessel. In solutions saturated with N_2 or air, conversion of the Pt^{2+}/dendrimer complexes to zerovalent DENs does not occur.[5] However, even when the reduction is carried out under favorable conditions, we[2] and others[4] have observed that complete reduction of intradendrimer Pt^{2+} may still not take place. For example, the positions of the Pt($4f_{7/2}$) peaks in XPS spectra are shifted positive from the positions corresponding to zerovalent, bulk Pt. Such shifts may correspond to the presence of unreduced Pt^{2+} [4] or from quantum effects associated with these very small metal nanoparticles.[2,39-41]

In this chapter, we provide a detailed description of the synthesis and properties of Pt DENs prepared using sixth-generation, hydroxyl-terminated, PAMAM dendrimers (G6-OH) and three different $PtCl_4^{2-}$:G6-OH ratios: 55, 147, and 240. Our principal finding is that a relatively small percentage of the total number of Pt^{2+} ions encapsulated within the dendrimers is reduced, but that the reduction

process is highly heterogeneous. In other words, after reduction each Pt^{2+}/dendrimer precursor is either fully reduced, to yield a DEN having a size and structure consistent with the original $PtCl_4^{2-}$:dendrimer ratio used for the synthesis, or the precursor is not reduced at all. That is, the product resulting from exposure to BH_4^- is a bimodal mixture of precursor that is fully reduced and precursor that is not reduced at all (Scheme 3.1). This counter-intuitive result is consistent with an autocatalytic process that entails slow formation of a nascent catalytic Pt seed within the dendrimer, followed by rapid, catalytic reduction of nearby Pt^{2+} ions.

3.3 Experimental

Chemicals. G6-OH dendrimers were purchased from Dendritech, Inc. (Midland, MI) as 10.0 wt% solutions in MeOH. Prior to use, the dendrimer stock solution was dried under vacuum and then redissolved in sufficient deionized water to make a 100 μM solution. The K_2PtCl_4, $NaBH_4$, and KCl were purchased from Sigma-Aldrich (Milwaukee, WI) and used as received. Aqueous solutions were prepared using 18 MΩ·cm Milli-Q water (Millipore, Bedford, MA).

Scheme 3.1

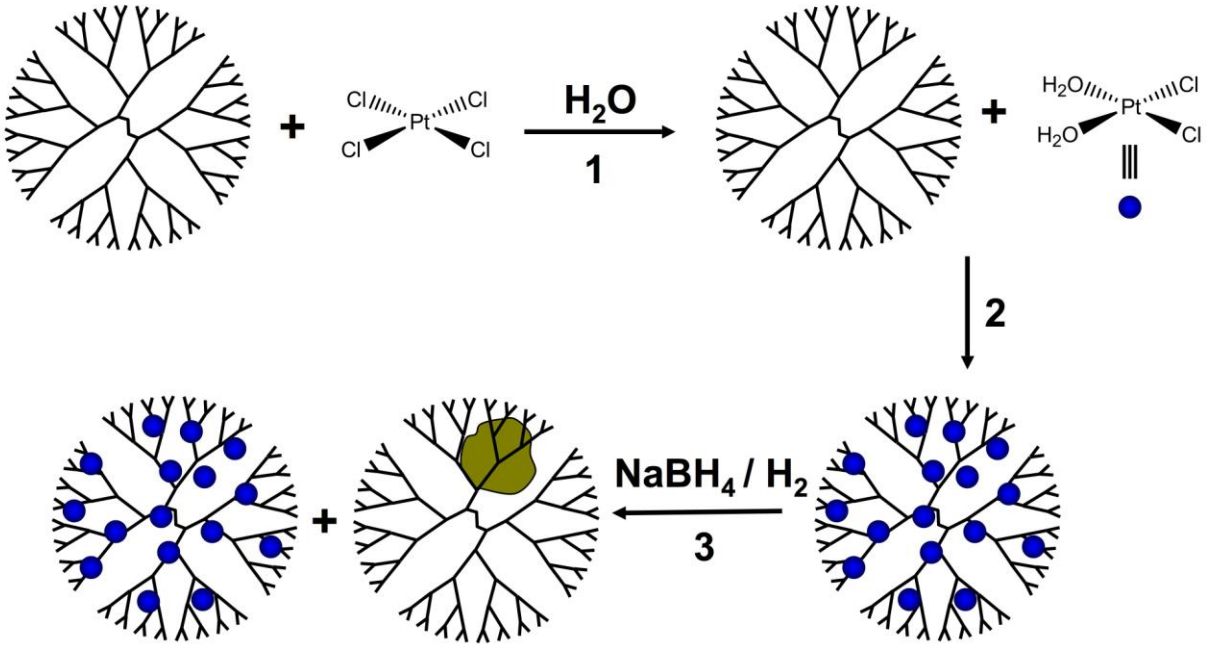

Synthesis of Pt DENs. Pt DENs were prepared using previously described methods.[3] Briefly, an aqueous solution of G6-OH was prepared. To this solution, 55, 147, or 240 equiv. of a freshly prepared 100 mM K_2PtCl_4 aqueous solution were added to yield the G6-OH$(Pt^{2+})_n$ (n = 55, 147, or 240) Pt^{2+}/dendrimer complexes, respectively. Unless otherwise indicated, the solutions were allowed to stir for 3.0 d to ensure complete complexation of Pt^{2+} to the tertiary amines present within the dendrimer interior. Note that there are 254 tertiary amines within G6-OH. These precursor complexes were then reduced using at least a 10-fold molar excess of $NaBH_4$ from a freshly prepared aqueous 0.50 M stock solution. The final concentration of dendrimer in all cases was 10.0 μM. Reduction was allowed to proceed for 24.0 h in a sealed reaction vessel prior to subsequent analysis. Powder samples of the DENs were obtained by lyopholization (Freezone 12, Labconco Corp.). The notation for the reduced DENs is G6-OH$(Pt)_n$ (n = 55, 147, or 240). Note that subscript n refers to the Pt^{2+}:G6-OH ratio used for the synthesis and is not meant to imply that each DEN has this exact composition.

Characterization. UV-vis spectra were obtained using a photodiode array UV-vis spectrometer (Model 8453, Agilent Technologies) and 1.00 cm or 0.200 cm quartz cuvets. All spectra were background corrected using a spectrum obtained from an aqueous 10.0 μM dendrimer solution. XPS data were collected using a Kratos Axis Ultra DLD spectrometer having a monochromatic Al Kα X-ray source. Spectra were collected in charge-compensation mode at a pass energy of 20 eV, a resolution of 0.1 eV, and a dwell time of 1.00 s. The samples were prepared by submerging Au-coated Si wafers in a freshly prepared 10.0 μM DEN solution for 3.00 h.[42] The DEN-modified wafers were then removed from the solution and dried under vacuum. To correct for charging, peak locations were referenced to the most intense carbon peak assumed to be present at 286.0 eV. This peak has previously been associated with the C-N bond.[1,2]

TEM analyses were performed using a JEOL 2010F microscope equipped with a Schottky field-emission gun operated at 200 keV with an ultra-high resolution pole piece providing a point resolution of 0.19 nm. HAADF imaging was completed using a 0.7 nm probe at a camera length of 20 cm. Samples were prepared using 200- or 300-

mesh Cu grids coated with an ultra-thin carbon film (Electron Microscopy Sciences, UltraThin Carbon-Coated Cu Grids). Samples were prepared by placing a Cu grid onto filter paper, applying 1-5 drops of the appropriate Pt DEN solution, and allowing the specimen to dry in air.

EXAFS spectra were obtained at beamline X18B of the National Synchrotron Light Source at the Brookhaven National Laboratory. The samples were measured either in solution or dried to a powder and then dispersed on adhesive tape. The tape samples were then folded multiple times to ensure sample homogeneity. All samples were measured in transmission mode and data analysis was subsequently completed using the IFEFFIT software package.[43]

High-energy XRD experiments were carried out at the 11-ID-B beamline (Advanced Photon Source, Argonne National Laboratory) using synchrotron radiation of 90.48 keV (λ=0.1372 Å) at room temperature. Both wet and dry Pt DENs were measured. The scattered radiation was collected with a large-area detector (General Electric). The experimental XRD data were reduced to atomic PDFs, $G(r) = 4\pi r(\rho(r) - \rho_0)$, where $\rho(r)$ and ρ_0 are the local and average atomic number densities, respectively, and r is the radial distance.

3.4 Results and Discussions

UV-vis spectroscopic analysis. Formation of the Pt^{2+}/dendrimer complex is the first step of the DEN synthesis. K_2PtCl_4 is usually the source of Pt^{2+}, but previous studies have shown that under most conditions it undergoes ligand substitution with water.[5,44] To determine the form of Pt^{2+} that binds to the tertiary amine groups of the dendrimer, we carried out time-resolved UV-vis studies of the $PtCl_4^{2-}$ ligand exchange and the subsequent reaction between the dendrimer and Pt^{2+} (Steps 1 and 2, Scheme 3.1). Recall that here Pt^{2+} represents any form of unreduced Pt^{2+}. Parts a-c of Figure 3.1 show time-resolved spectra obtained from 110, 294, and 480 μM aqueous $PtCl_4^{2-}$ solutions, respectively. These are the same concentrations used for the synthesis of 2.00 μM DEN solutions containing 55, 147, and 240 Pt atoms, respectively (*vide infra*).

Figure 3.1a confirms water substitution of $PtCl_4^{2-}$ present at the concentration used to prepare G6-OH$(Pt^{2+})_{55}$. The black spectrum, taken immediately after solution preparation, reveals absorbances at 215 and 230 nm, which are characteristic of $PtCl_4^{2-}$.[44] The intensity of these peaks

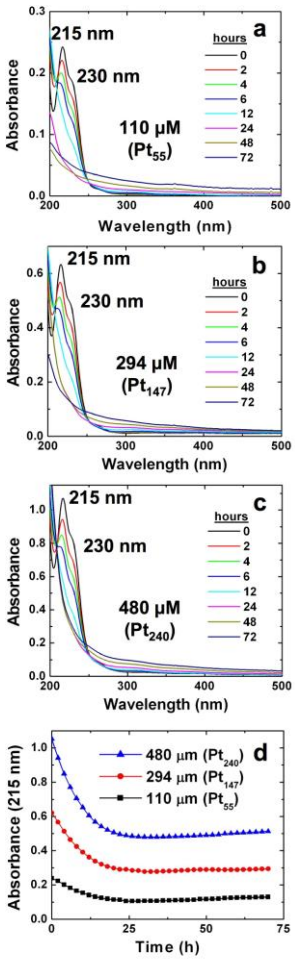

Figure 3.1. Time-resolved UV-vis spectra showing the water substitution of K_2PtCl_4 at concentrations of (a) 110 μM, (b) 294 μM, and (c) 480 μM, which represent the concentrations used for the synthesis of G6-OH(Pt_n), n = 55, 147, and 240, DENs, respectively. (d) Plots of the absorbance at λ = 215 nm (from parts a – c) as a function of time for the data shown in parts (a) – (c). The reduction in the intensity of this peak corresponds to water substitution of $PtCl_4^{2-}$.

decreases for ~15 h and then achieves a nearly constant value (Figure 3.1d). The decrease in absorbance is directly attributable to the ligand exchange of $PtCl_4^{2-}$ to yield $PtCl_n(H_20)_{4-n}^{2-n}$ ($n < 4$).[44] Another important feature of these spectra is that at times > 24 h, the absorbance at high wavelengths increases. We believe this is attributable to absorption and scattering of light associated with aggregation and/or polymerization of aquated $PtCl_n(H_20)_{4-n}^{2-n}$.[36] Indeed, a black precipitate is observed after 72 h. Spectra similar to those obtained for 110 μM are observed at 294 μM (Figure 3.1b) and 480 μM Pt^{2+} (Figure 3.1c). The initial and final (t > 20 h) absorbances of all three solutions (Figure 3.1d) scale approximately linearly with the initial concentration of $PtCl_4^{2-}$. The slight deviation from Beer's law is attributable to the overlapping absorbance at 230 nm and the associated difficulty of accurately subtracting the background absorbance. Figure 3.1d indicates that the ligand exchange reaction reaches equilibrium within 20 h. To determine the kinetic rate constant of the water substitution reaction, the absorbance of the $PtCl_4^{2-}$ solution (see Figure 3.1) at 215 nm was plotted against time in three different formats.

Specifically, absorbance vs. time, ln(absorbance) vs. time, and the reciprocal of the absorbance vs. time were each fitted using linear least squares regression to a linear trendline. As is customary, the data points at long times (48 and 72 h) were not considered. The first-order fit, ln(A) vs. time, had an R^2 value of 0.999, which was significantly better than fits to the other two models. The absorbance was converted to concentration units using Beer's law, and then ln[$PtCl_4^{2-}$] was plotted vs. time (Figure 3.2). The pseudo-first-order rate constant, k, derived from this plot is 1.20×10^{-5} s^{-1}. These kinetic results are reproducible and in good agreement with previous studies.[45,46]

In addition to studying the water substitution of $PtCl_4^{2-}$, we also carried out a spectroscopic study of the reaction between the G6-OH dendrimer and Pt^{2+}.[2,3,34] As discussed earlier, this is a two-step process in which $PtCl_4^{2-}$ first undergoes ligand exchange and then the product reacts with interior tertiary amines of the dendrimer to form a covalent bond (Scheme 3.1).[2,3,34,37,38,47,48] Figure 3.3a shows time-resolved spectra obtained during preparation of

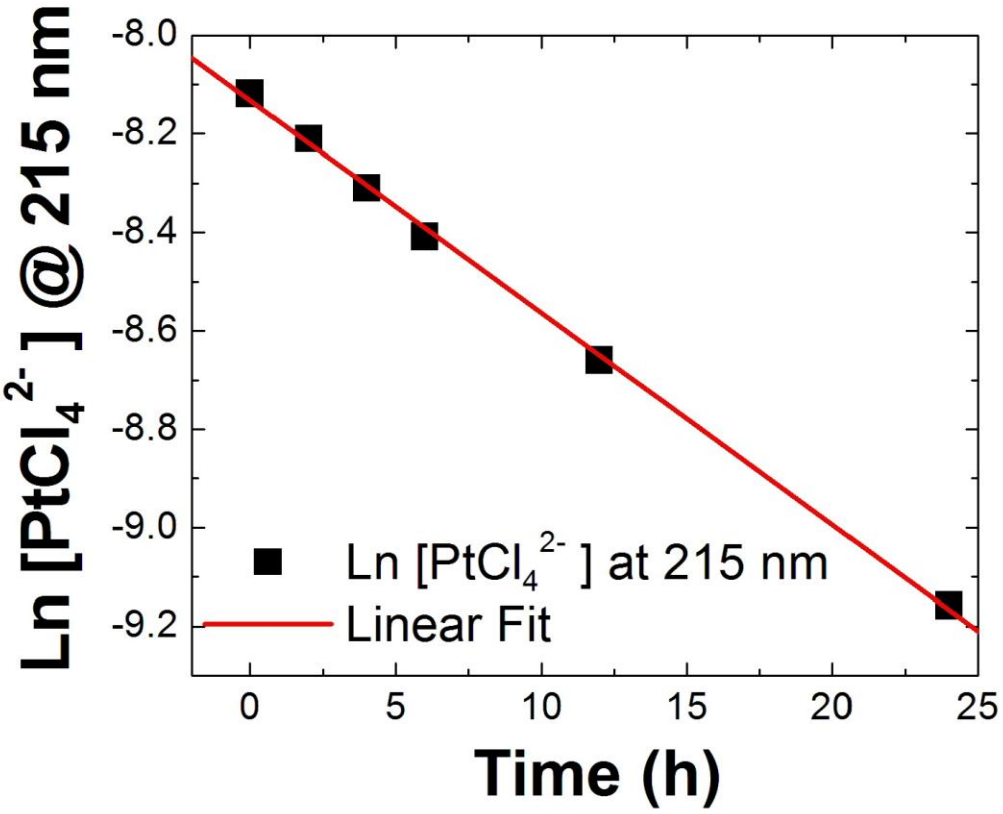

Figure 3.2. Pseudo-first order kinetics analysis of the data from Figure 3.1.

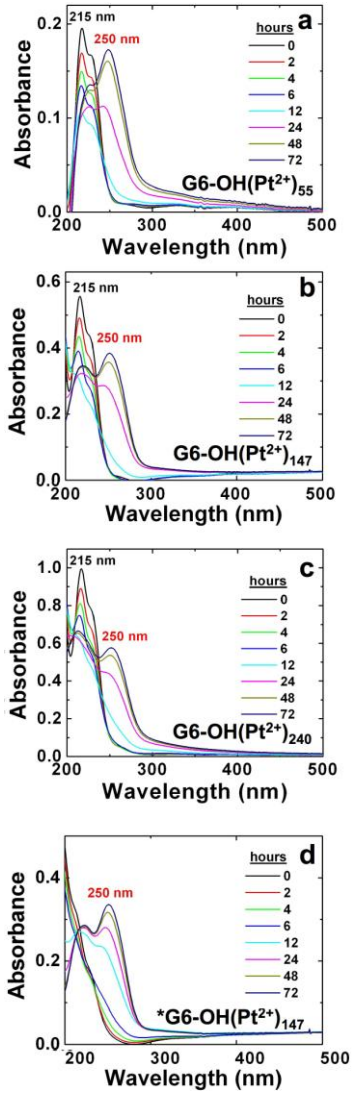

Figure 3.3. Time-resolved UV-vis spectra indicating formation of (a) G6-OH$(Pt^{2+})_{55}$, (b) G6-OH$(Pt^{2+})_{147}$, and (c) G6-OH$(Pt^{2+})_{240}$ complexes. A freshly prepared K_2PtCl_4 solution was used in parts (a) - (c) prior to mixing with the dendrimer solution. (d) Time-resolved UV-vis spectra for the synthesis of G6-OH$(Pt^{2+})_{147}$ using a K_2PtCl_4 solution prepared 12 h prior to complex formation.

G6-OH(Pt^{2+})$_{55}$. The first spectrum was obtained immediately after addition of an appropriate aliquot of freshly prepared, aqueous 10.0 mM K_2PtCl_4 to a 2.00 μM G6-OH dendrimer solution. As discussed earlier, the peaks at 215 and 230 nm are attributable to $PtCl_4^{2-}$.[44] These peaks decrease in intensity for approximately 10 h, at which time a peak at 250 nm begins to develop. This new band arises from the ligand-to-metal charge transfer (LMCT) from the tertiary amines of the dendrimer to bound Pt^{2+},[2,34,49] and it continues to grow for an additional 20 h. After a total of 30 h, the absorbance of the LMCT band achieves a nearly time-independent value (black curve, Figure 3.4a). As discussed later, there is no observable precipitation of zero-valent Pt metal when BH_4^- is added to Pt^{2+}/dendrimer solutions that have been allowed to react for 3 d, and therefore we conclude that the reaction between Pt^{2+} and the dendrimers is complete within this time period.

Figures 3.3b and 3.3c provide time-resolved spectra for formation of the G6-OH(Pt^{2+})$_{147}$ and G6-OH(Pt^{2+})$_{240}$ complexes, respectively, and the corresponding changes in the LMCT bands are provided in Figure 3.4a (red and blue curves, respectively). These complexes, which have the highest Pt^{2+}:dendrimer ratios, exhibit LMCT bands having a

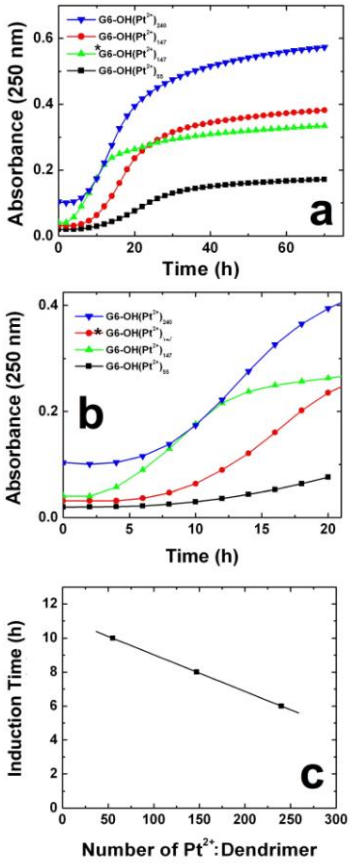

Figure 3.4. (a) Plots of the absorbance of the LMCT band (λ = 250 nm) for G6-OH$(Pt^{2+})_n$ (n= 240 blue, 147 red, 55 black, 55* green) as a function of time derived from the results shown in Figure 3.3. (b) Same as (a), except on an expanded time scale. (c) Plot of the induction time for formation of the Pt^{2+}/dendrimer complex as a function of the Pt^{2+}:dendrimer ratio. The induction time is defined as the time required for a 1% increase in the initial absorbance at λ = 250 nm. * refers to pre-aquated Pt^{2+}. See text for details.

slight (≤ 2 nm) shift to higher wavelength. The increase in the steady-state absorbance of the three complexes is simply a consequence of the increasing Pt^{2+}:dendrimer ratio.

Figure 3.4b provides plots of the absorbance of the LMCT band as a function of time during the first 20 h of the reaction between Pt^{2+} and the dendrimers. The model (Scheme 3.1) predicts an induction period for the LMCT band corresponding to the time required for ligand exchange of $PtCl_4^{2-}$ (step 1), and this induction period is clearly observed in Figure 3.4b. The induction period, which is plotted in Figure 3.4c, is defined as the time required for a 1% increase in the initial absorbance at 250 nm. The induction period decreases as the Pt^{2+}:dendrimer ratio increases, because there is more aquated $PtCl_4^{2-}$ present in the more concentrated solutions at any specified time[50] and hence reaction with the dendrimer is detected sooner. From the experiments represented by Figures 3.1-3.4, we can draw three important conclusions. First, $PtCl_4^{2-}$ must undergo water substitution prior to reacting with the dendrimer. Second, formation of the complex is kinetically controlled and hence depends on the concentration of the aquated Pt^{2+} precursor in solution. Third, regardless of the

Pt^{2+}:dendrimer ratio, reaction between $PtCl_n(H_2O)_{4-n}^{2-n}$ ($n < 4$) and G6-OH is complete within 30 h.

To confirm the validity of these three conclusions, three key control studies were carried out. The first experiment is represented by Figure 3.3d. Here, a 10.0 mM stock solution of K_2PtCl_4 was prepared, but it was allowed to undergo water substitution for 12 h before it was mixed with the G6-OH solution. Notice that in this case, a small absorbance at 250 nm (corresponding to the Pt^{2+}/G6-OH complex) is observed after just 2 h (Figure 3.3d). The use of preaquated K_2PtCl_4 should eliminate the induction period observed for freshly prepared K_2PtCl_4 solutions, and the rate of complex formation should only be limited by the reaction between $PtCl_n(H_2O)_{4-n}^{2-n}$ ($n < 4$) and the dendrimer. Indeed, a comparison of the red (not preaquated) and green (preaquated) curves in Figures 3.4a and 3.4b, clearly indicates that formation of the Pt^{2+}/dendrimer complex occurs more quickly when $PtCl_4^{2-}$ is preaquated.

A second control experiment was carried out in which freshly prepared K_2PtCl_4 and G6-OH solutions were mixed in an effort to prepare G6-OH$(Pt^{2+})_{147}$, but this time 1.00 M KCl was also present. It is known that under these conditions the common-ion effect prevents ligand exchange of $PtCl_4^{2-}$.[45]

Time-resolved spectra corresponding to this experiment are provided in Figure 3.5. No changes in these spectra are observed even after 72 h, confirming that no reaction takes place between Pt^{2+} and the dendrimer in the absence of $PtCl_4^{2-}$ ligand exchange (Scheme 3.1).

The third control experiment was intended to confirm that all, or nearly all, of the Pt^{2+} reacts irreversibly with the dendrimer. This experiment was carried out as follows. First, two solutions were prepared consisting of aquated $PtCl_4^{2-}$ and G6-OH$(Pt^{2+})_{147}$. Second, these solutions were passed through Millipore Centricon centrifugal filters having a molecular weight cut-off of 10 kDa. Third, the UV-vis absorbance spectra of the original solutions were compared to those of the filtrates. The resulting spectra are provided in Figure 3.6.

For aquated Pt^{2+}, nearly all of the Pt^{2+} is recovered in the filtrate, but for the Pt^{2+}/dendrimer complex the amount of Pt^{2+} observed in the filtrate is below the detection limit. Accordingly, we conclude that all, or nearly all, Pt^{2+} is strongly associated with the dendrimer.

Following reaction of Pt^{2+} with the dendrimer, addition of $NaBH_4$ results in formation of DENs. Figure 3.7a compares the UV-vis spectra of G6-OH$(Pt^{2+})_{55}$ before and after

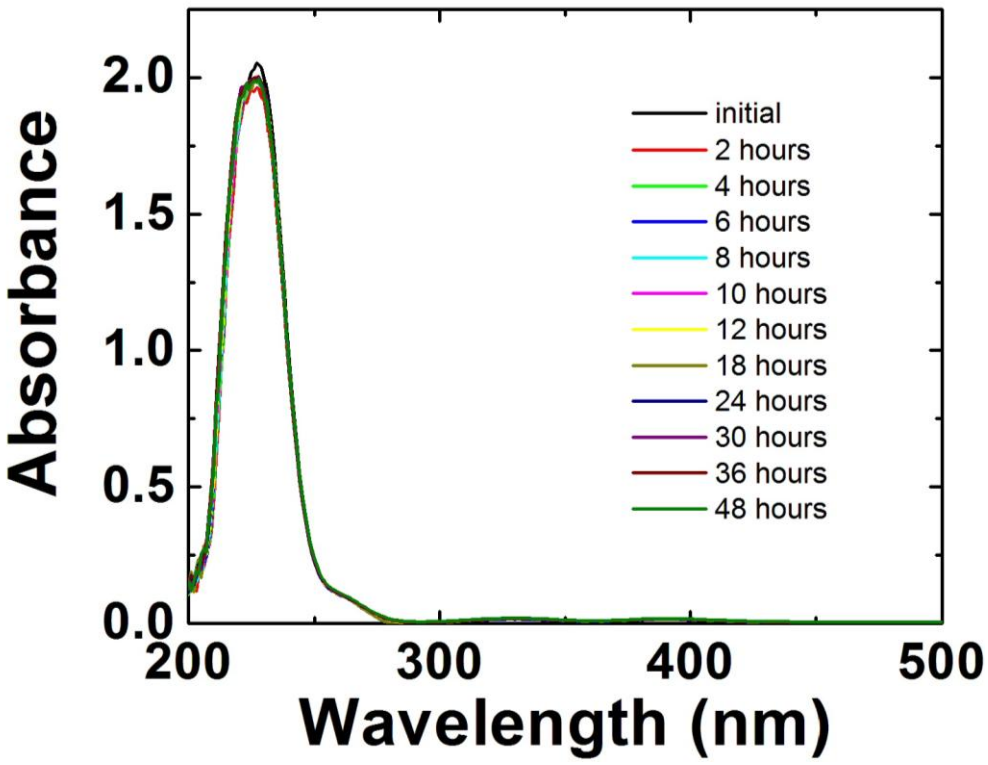

Figure 3.5. Time-resolved UV-vis spectra obtained after mixing 2.00 μM G6-OH dendrimer with 147 equiv. (298 μM) K_2PtCl_4 in the presence of 1.00 M KCl. A freshly prepared K_2PtCl_4 solution was used as the Pt^{2+} source. The results indicate that $PtCl_4^{2-}$ does not undergo water substitution under these conditions, and hence no Pt^{2+}/dendrimer complex forms.

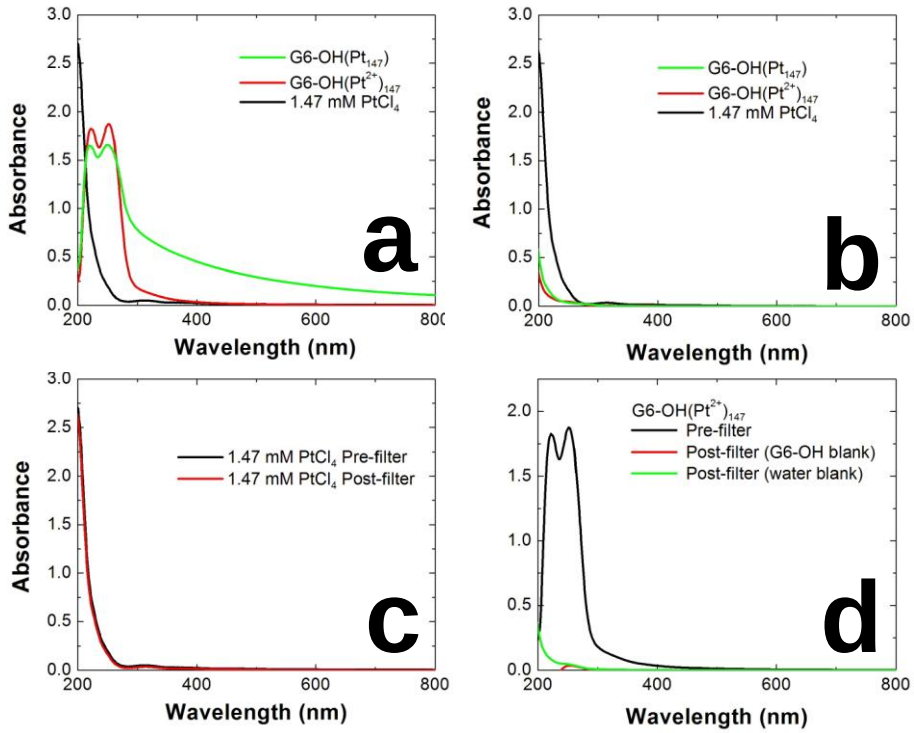

Figure 3.6. UV-vis spectra were obtained before (a) and after (b) filtration. Direct comparison of the spectra for $PtCl_4^{2-}$ before and after filtration (Frame c) demonstrates that all $PtCl_4^{2-}$ is recovered in the filtrate after filtration. The same comparison is provided in Frame d for the G6-OH$(Pt^{2+})_{147}$ complex, and it shows all of the Pt^{2+} present in solution is retained by the filter.

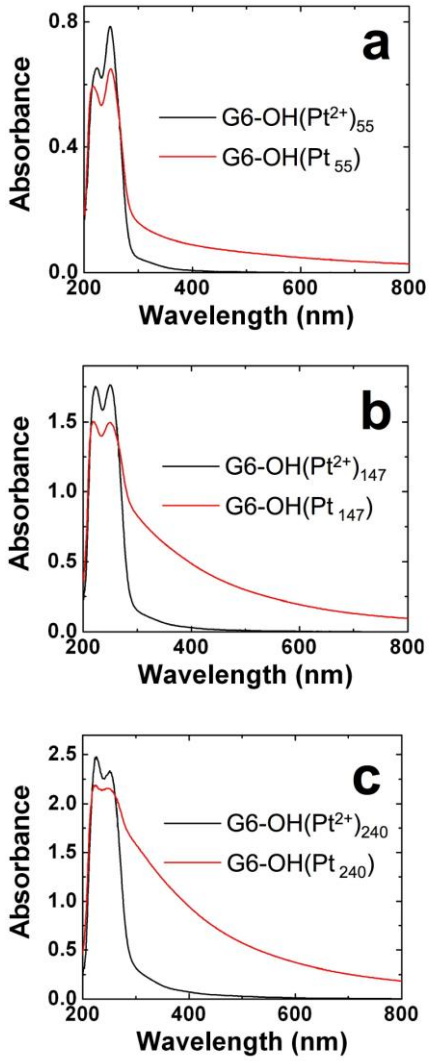

Figure 3.7. UV-vis spectra for the (a) G6-OH$(Pt^{2+})_{55}$, (b) G6-OH$(Pt^{2+})_{147}$, and (c) G6-OH$(Pt^{2+})_{240}$ complexes before and after reduction with BH_4^-. In all cases the G6-OH concentration was 10.0 μM, and $PtCl_4^{2-}$ was allowed to react with the dendrimer for 3 d prior to reduction.

reduction. Reduction leads to two significant spectral changes. First, the LMCT band at 250 nm decreases, and second, there is an increase in absorbance at longer wavelengths.[51] As we have pointed out previously, these observations are consistent with only partial reduction of the Pt^{2+}/dendrimer complex.[2] These same observations apply to the G6-OH$(Pt^{2+})_{147}$ and G6-OH$(Pt^{2+})_{240}$ precursors. Unfortunately, it is not possible to obtain quantitative information about the extent of reduction from these spectra for the following two reasons. First, there is no way to prepare a 100%-reduced solution of the Pt DENs (*vide infra*), and therefore it is not possible to determine the extinction coefficients of the pure compounds. Second, because of the extensive overlap of the spectra before and after reduction, there is no means to determine the background signal originating from the partially reduced DENs and hence the absorbance arising from just the unreduced precursor. Accordingly, it is not possible to accurately determine the percentage absorbance arising from the unreduced DENs at λ_{max} for the precursor. However, the extent of reduction can be extracted from the EXAFS data discussed later. One final note: we carried out a

filtration experiment for G6-OH(Pt_{147}) like that described in the previous paragraph for G6-OH(Pt^{2+})$_{147}$ and found no detectable level of Pt^{2+} in the filtrate. This experiment shows that even after reduction all forms of platinum are associated with the dendrimer.

X-ray Photoelectron Spectroscopy. XPS was used to confirm partial reduction of the Pt^{2+}/dendrimer complex. Before discussing the data, however, we wish to point out that there was a significant degree of charging in these samples, and therefore the positions of the Pt(4f) peaks were referenced to the location of the most intense carbon peak. The position of this peak (286.0 eV) was previously reported by Chen and coworkers for G4-OH PAMAM dendrimers, and therefore binding energies reported here can be directly compared to their results.[4] Nevertheless, the absolute binding energies reported here should be viewed with caution, although the relative shifts of the Pt(4f) peaks are reliable.

Figure 3.8a shows the Pt(4f) region of the unreduced complexes for the three Pt:G6-OH dendrimer ratios examined in this study. The Pt($4f_{7/2}$) peak lies at 72.9 eV for all three G6-OH(Pt^{2+})$_n$ complexes. This binding energy is close

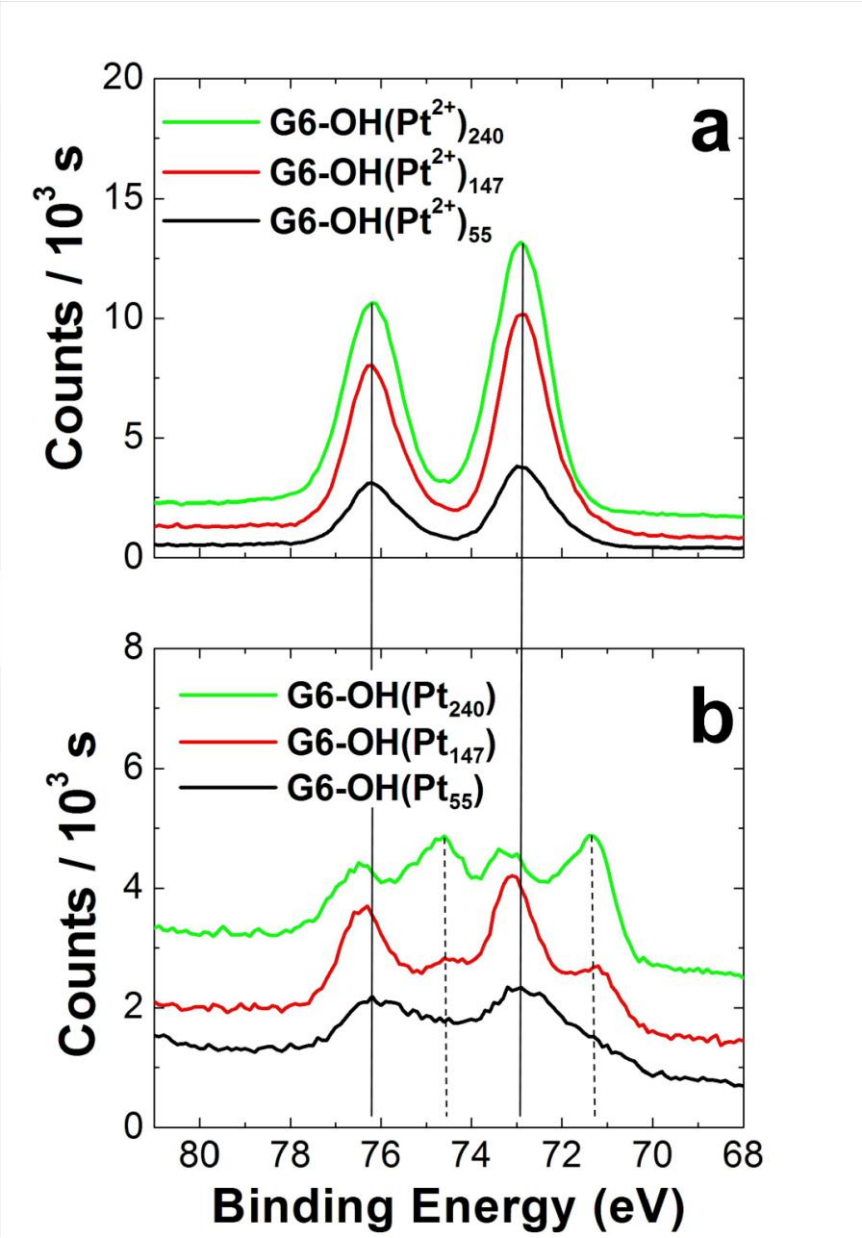

Figure 3.8. XPS spectra in the Pt(4f) region of the G6-$OH(Pt^{2+})_n$ complexes (a) before and (b) after reduction with BH_4^-.

to the NIST database value of 73.4 eV reported for the $PtCl_4^{2-}$ starting material.[52] The slight shifts to lower binding energy observed for G6-OH$(Pt^{2+})_n$ are consistent with a strong LMCT interaction between Pt^{2+} and the dendrimer as EXAFS results have previously shown.[5] Note also that this binding energy is the same as we previously reported for G4-OH$(Pt^{2+})_{60}$[53] and close to that of several related Pt^{2+}-N complexes (73.1 – 73.5).[54]

Pt is present in two distinct oxidation states after addition of BH_4^- (Figure 3.8b), confirming only partial reduction of the Pt^{2+}/dendrimer complexes. The positions of the pair of Pt($4f_{7/2}$) and Pt($4f_{5/2}$) peaks at higher binding energy closely correlate to the positions observed prior to reduction, but they are shifted very slightly to higher energy. This might suggest selective reduction of Pt^{2+} in specific metal-binding configurations within dendrimers, but the shift is so small that even this degree of speculation may be unwarranted. The Pt($4f_{7/2}$) and Pt($4f_{5/2}$) peaks at lower binding energy presumably correspond to reduced Pt in the form of DENs. Regardless of the size of the DENs, the Pt($4f_{7/2}$) peak is present at 71.3 ± 0.1 eV which is consistent with the value for bulk Pt (71.2 eV).[52]

Gao and coworkers reported a similar binding energy (71.4 eV) for nanoparticles of comparable size.[55] A previous study by Chen and coworkers reported the binding energy of the Pt($4f_{7/2}$) peak for a G4-OH(Pt_{40}) DEN monolayer at 73.3 eV.[4] We previously reported binding energies of 73.0 eV[2] and 71.3 eV[53] for G4-NH_2(Pt_{30}) and G4-OH(Pt_{60}) DENs, respectively. The absolute values for reduced Pt will depend on a number of factors, but the important result is that the XPS data clearly indicate just partial reduction of the Pt^{2+}/dendrimer precursor complex by BH_4^-.

TEM Analysis. Pt DENs nominally consisting of 55, 147, and 240 atoms were analyzed by TEM. Samples were prepared by applying several drops of a DEN solution onto a Cu grid coated with an ultra-thin carbon film. Figure 3.9 shows representative bright field (BF) and high-angle annular dark field (HAADF) micrographs of the Pt DENs at moderate magnifications. HAADF imaging was used in addition to conventional BF imaging to provide enhanced *Z*-contrast for Pt, which significantly improved detection of the smallest nanoparticles. In all images, the majority of the nanoparticles have a nearly isometric morphology; however, there is a minority of agglomerated particles. At this

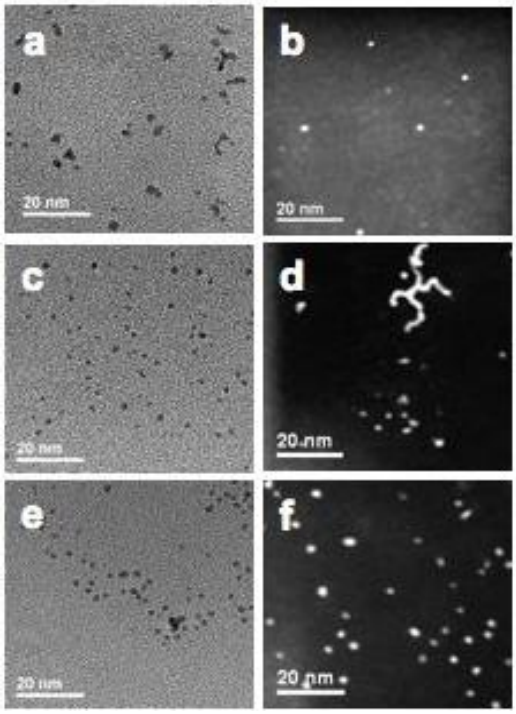

Figure 3.9. Representative bright-field micrographs of (a) G6-OH(Pt_{55}), (c) G6-OH(Pt_{147}), and (e) G6-OH(Pt_{240}), and (b), (d), and (f) the corresponding HAADF micrographs, respectively.

time we are uncertain whether these structures exist in solution, or whether they form during drying prior to TEM analysis. Typical chain lengths are equivalent to 2-5 linearly aggregated nanoparticles, but occasionally long irregularly shaped chains are observed, such as that shown at the top of Figure 3.9d.

The measured sizes for the G6-OH(Pt_{55}), G6-OH(Pt_{147}), and G6-OH(Pt_{240}) DENs are 1.3 ± 0.3, 1.6 ± 0.3, and 2.0 ± 0.4 nm, respectively. The pixel resolution used for these measurements ranged between 0.05 nm to 0.25 nm and agglomerates were not counted. These values can be compared to the theoretical values for the diameters of cuboctahedral particles containing these same numbers of atoms: 1.2, 1.6, and 1.9 nm,[16] respectively. This high level of agreement is consistent with complete reduction of the Pt^{2+}/dendrimer precursors but contrary to the UV-vis and XPS results discussed earlier.

HREM imaging of the reduced DENs clearly show that they are relatively well ordered at the atomic scale. Figure 3.10 displays high-resolution images of all three DENs with their respective diffraction pattern obtained from FFT analysis. From this analysis (insets in Figure 3.10), characteristic distances, d, between Pt atoms inside

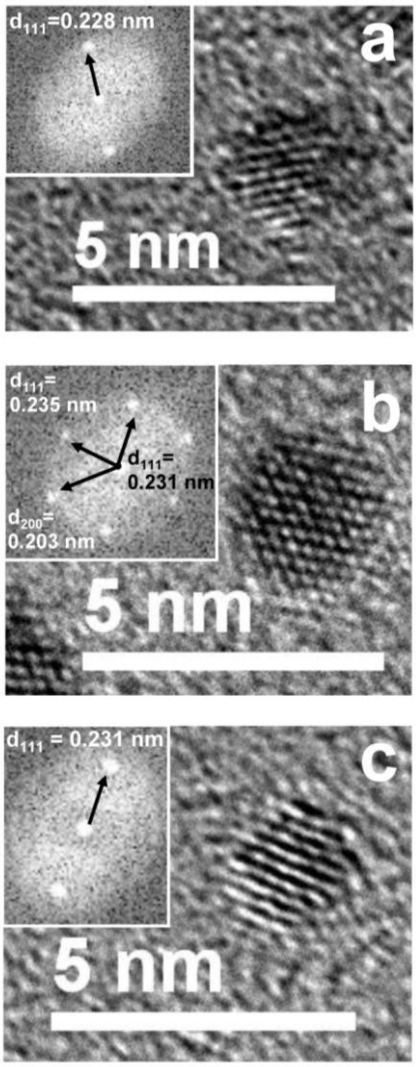

Figure 3.10. HREM micrographs of (a) G6-OH(Pt_{55}), (b) G6-OH(Pt_{147}), and (c) G6-OH(Pt_{240}). The insets show the FFT patterns for each particle and the measured d-spacing.

DENs have been determined. The distances are found to be very close to interplanar spacing d_{111}= 2.27 Å and d_{200}= 1.96 Å observed in bulk fcc Pt.

One final note about the TEM analysis of Pt DENs: we were concerned that the electron beam itself might reduce the Pt^{2+}/dendrimer DEN precursors. We have examined grids prepared with a complex (G6-OH$(Pt^{2+})_{147}$), a partially reduced sample (2h reduction time), and a DENs sample (G6-OH(Pt_{147})). A sample of the results is shown in Figure 3.11. In each case, EDS was used to detect Pt in the same area as the images. No growth of Pt nanoparticles was observed for these samples for 1 h, long enough to burn the C film on the grid. Therefore we conclude that under the conditions used to obtain the results reported here the influence of the electron beam on the formation of DENs is negligible.

EXAFS Analysis. EXAFS studies were conducted on Pt DENs in the solid state and dissolved in water (DEN concentration = 100 μM), which we refer to as "dry" and "wet" DENs, respectively. This comparison provides an opportunity to determine how the presence of water might affect the DEN structure, extent of reduction, and

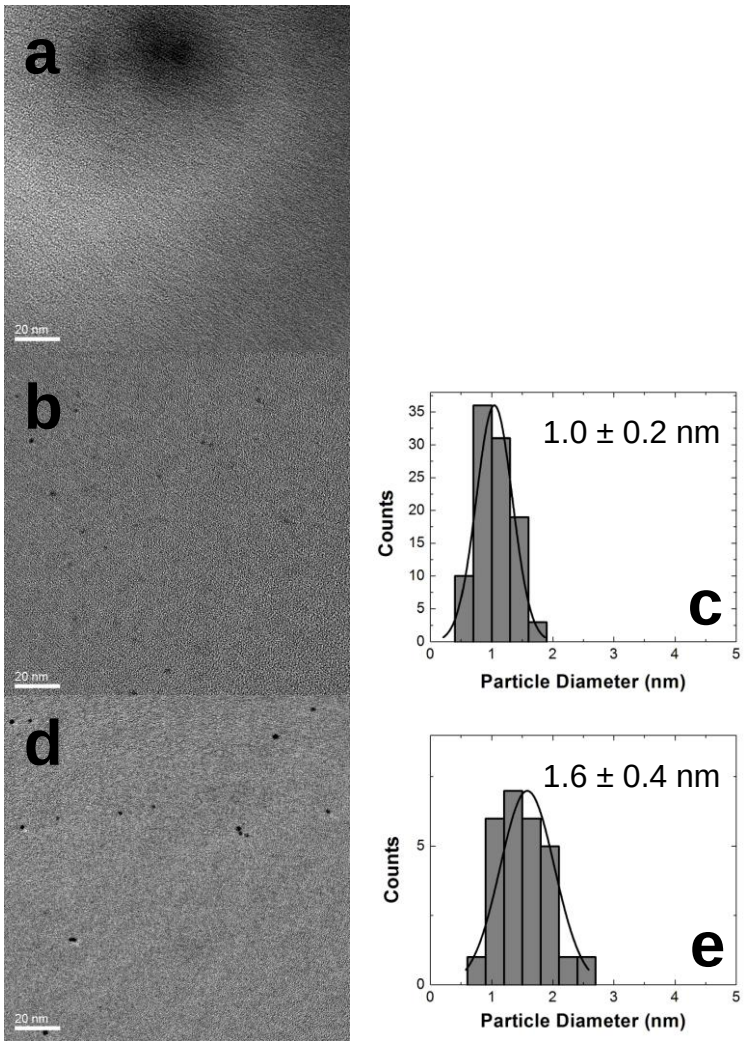

Figure 3.11. Representative TEM images and size distribution histograms demonstrating that the electron beam does not reduce the G6-OH$(Pt^{2+})_{147}$ precursor. Histograms are provided for the (d) seeds and (e) DENs from an initial image of a nearby area before EDS.

stability.[5] The EXAFS analyses for dry and wet G6-OH(Pt_n) (n = 55, 147, and 240) DENs are provided in Figure 3.12, and the corresponding data for n = 100 and 200 (wet samples only) is given in Figure 3.13. In all cases, the black curves represent the experimentally obtained and Fourier-transformed EXAFS data, and the red curves are the fits obtained using FEFF6 theory[56] and the Artemis analysis program.[57] Each data set was obtained as an average of four independent energy scans to improve the signal-to-noise ratio.

The important conclusion from the EXAFS study is that the experimentally determined coordination numbers (CNs) of the dry DENs are clearly related to the Pt^{2+}:dendrimer ratio used for the synthesis. Specifically, a Pt-Pt CN of 1.07 ± 0.55 was determined for the dry G6-OH(Pt_{55}) DENs (Figure 3.12a), which is quite low for a Pt particle consisting of 55 atoms. This observation indicates that only a small fraction of the total Pt^{2+} initially present in the G6-OH(Pt^{2+})$_{55}$ precursor solution is reduced. Indeed, we can estimate the percentage of Pt^{2+} ions that are reduced by comparing the experimental value of the CN (1.07) with the value calculated for a particle with a cuboctahedral shape

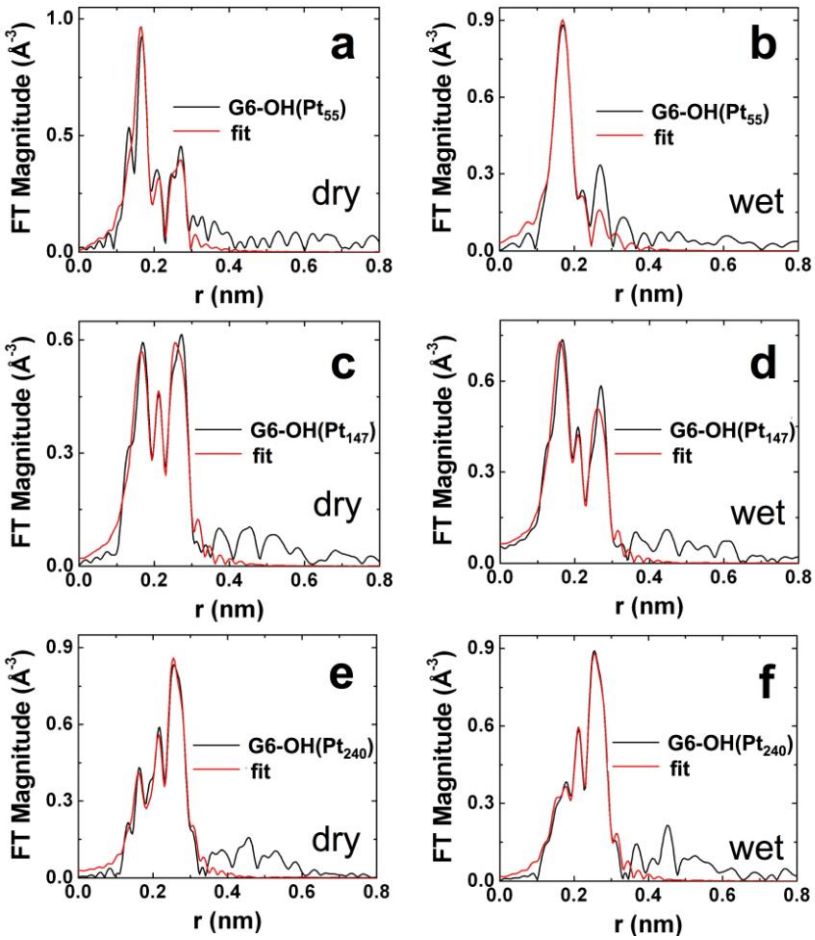

Figure 3.12. EXAFS analysis of (a and b) G6-OH(Pt_{55}), (c and d) G6-OH(Pt_{147}), and (e and f) G6-OH(Pt_{240}). The black curves represent the experimentally obtained data, and the red curves correspond to the calculated fits.

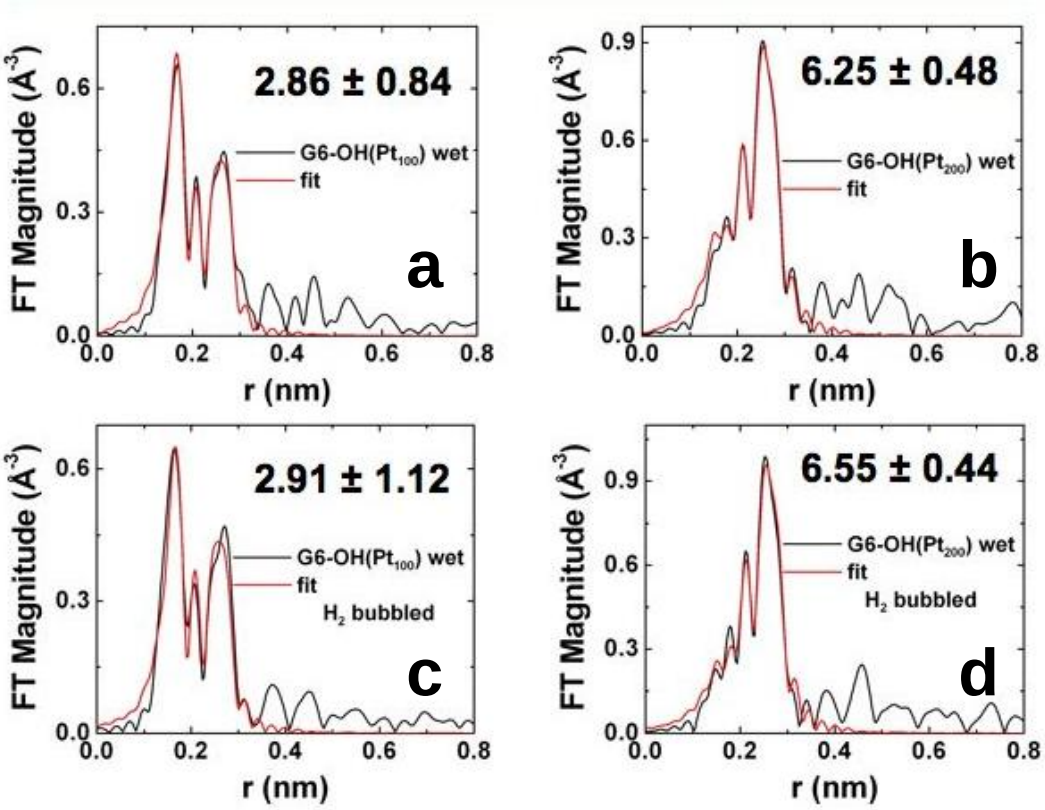

Figure 3.13. EXAFS analysis of nominal solutions of (a and c) G6-OH(Pt_{100}) and (b and d) G6-OH(Pt_{200}). The spectra obtain in (c and d) were obtain from the same solutions used in (a and b), but after bubbling H_2 through the solution for 20 h. The black curves represent the experimentally obtained data, and the red curves correspond to the fits.

consisting of 55 atoms (7.86).[58] This calculation reveals that only 14% of the total number of encapsulated Pt^{2+} ions are reduced during the preparation of G6-OH(Pt_{55}) DENs. However, EXAFS does not provide information on how the reduced fraction of Pt^{2+} is distributed between dendrimers. It may seem intuitive that each dendrimer would contain roughly equal numbers of reduced and unreduced Pt^{2+}, but the TEM results, and the XRD results discussed later, indicate this is not true. Rather, a minority of dendrimers contain fully reduced DENs (that is, G6-OH(Pt_{55})) and a majority of dendrimers contain Pt^{2+} that is not reduced at all (that is, G6-OH(Pt^{2+})$_{55}$).

As the Pt^{2+}:G6-OH ratio increases to 147 and 240, the overall Pt-Pt CN increases to 3.99 ± 0.61 and 6.09 ± 0.42, respectively (the CNs for the dry DENs are plotted as a function of the Pt^{2+}:dendrimer ratio in Figure 3.14a). These values can be compared to theoretical Pt-Pt CNs for regular cuboctahedra of 8.98 and 9.52, respectively (Figure 3.14c).[58] Using the experimental and calculated values of the CNs, it is possible to use the approach discussed in the previous paragraph to estimate the fraction of encapsulated Pt^{2+} ions reduced by BH_4^- for the higher

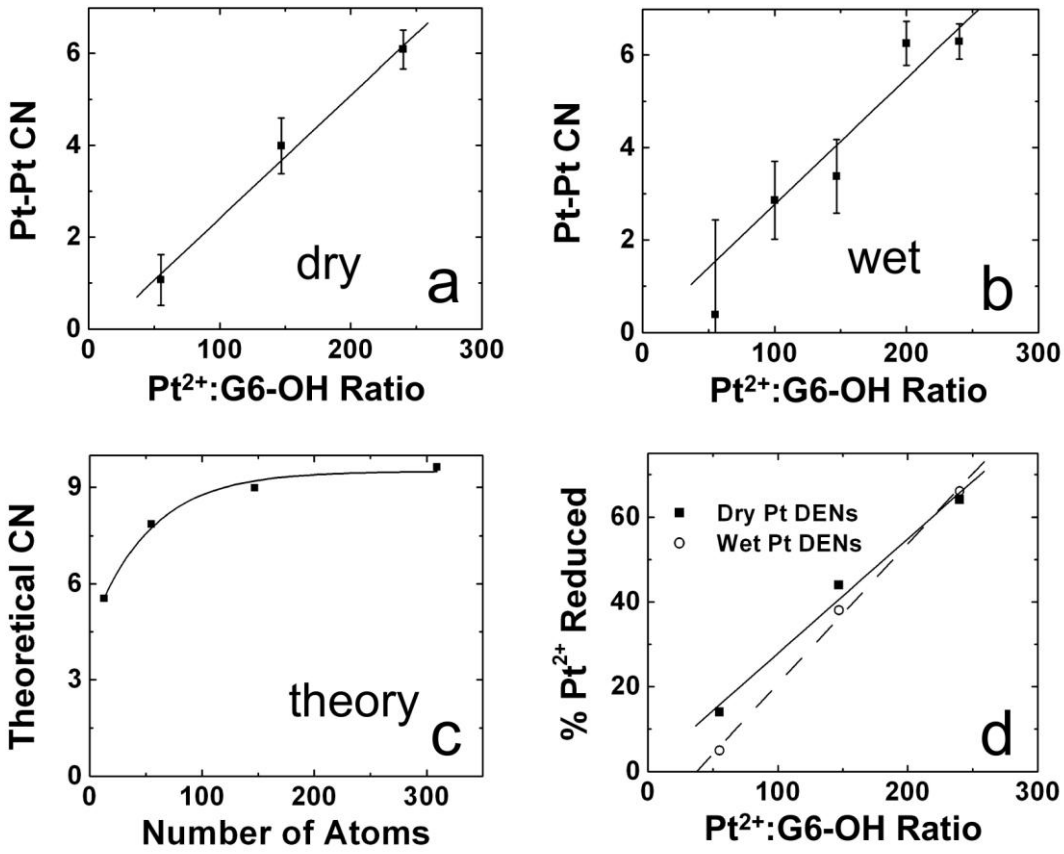

Figure 3.14. Comparison of the Pt-Pt CNs for (a) dry and (b) wet Pt DENs at the indicated Pt^{2+}:G6-OH ratios. (c) Calculated M-M CNs for cuboctahedral particles in this size range. (d) A plot of the percentage of Pt reduced as a function of the Pt^{2+}/G6-OH ratio.

Pt^{2+}:G6-OH ratios. These values are 44% and 64% reduction of the total Pt^{2+} originally present in G6-OH$(Pt^{2+})_{147}$ and G6-OH$(Pt^{2+})_{240}$, respectively. Figure 3.14d is a plot of the percentage of Pt^{2+} reduced as a function of the Pt^{2+}:G6-OH ratio for all three Pt^{2+}:G6-OH ratios examined in this study. It shows that as the Pt^{2+}:G6-OH ratio increases, the total percentage of Pt^{2+} reduced increases. We will return to this observation later.

The trend in CNs for wet DENs (Figures 3.12, 3.13, and 3.14b) is similar to that observed for the dry Pt DENs. Here, the Pt-Pt CNs are 0.39 ± 2.05, 2.86 ± 0.84, 3.38 ± 0.80, 6.25 ± 0.48, and 6.29 ± 0.38 for G6-OH$(Pt^{2+})_n$ (n = 55, 100, 147, 200, and 240, respectively). Using the same set of assumptions discussed in the previous two paragraphs, the percentage of reduced Pt can be calculated for the wet DENs. These values are 5%, 38%, and 66% for the G6-OH$(Pt^{2+})_n$ (n = 55, 147, 240) precursors, respectively. Within the uncertainty of the measurements, these values are very close to those obtained for the dry DENs: as the Pt^{2+}:G6-OH ratio increases, the percentage of Pt^{2+} reduced increases (Figure 3.14d).

We attempted to induce a higher percentage of Pt^{2+} reduction by bubbling H_2 through the G6-OH(Pt_{100}) and G6-OH(Pt_{200}) solutions of wet DENs for 20 h after the initial EXAFS analysis. The fitting analyses of these data are provided in Figure 3.13. However, no change in the Pt-Pt CN is observed for either sample, indicating that no further reduction occurs for these DENs in the presence of a saturated, aqueous H_2 solution.

XRD/PDF Analysis. To better understand the structure of the Pt DENs, we performed high-energy XRD/PDF analyses[59] of the wet and dry Pt DENs. As shown in Figure 3.15, the PDF for bulk Pt exhibits well-defined peaks to high interatomic distances. This characteristic reflects the perfect fcc-type structure of crystalline metallic materials. Dry G6-OH(Pt_{147}) DENs exhibit similarly well-defined PDFs (sharp peaks), which indicate they are also crystalline and may be approximated in terms of a finite particle having an fcc-type lattice that is only moderately strained due to surface relaxation. Additionally, decay of the dry G6-OH(Pt_{147}) PDF indicates a correlation length of 1.7 nm (CN = 10), which is consistent with both the

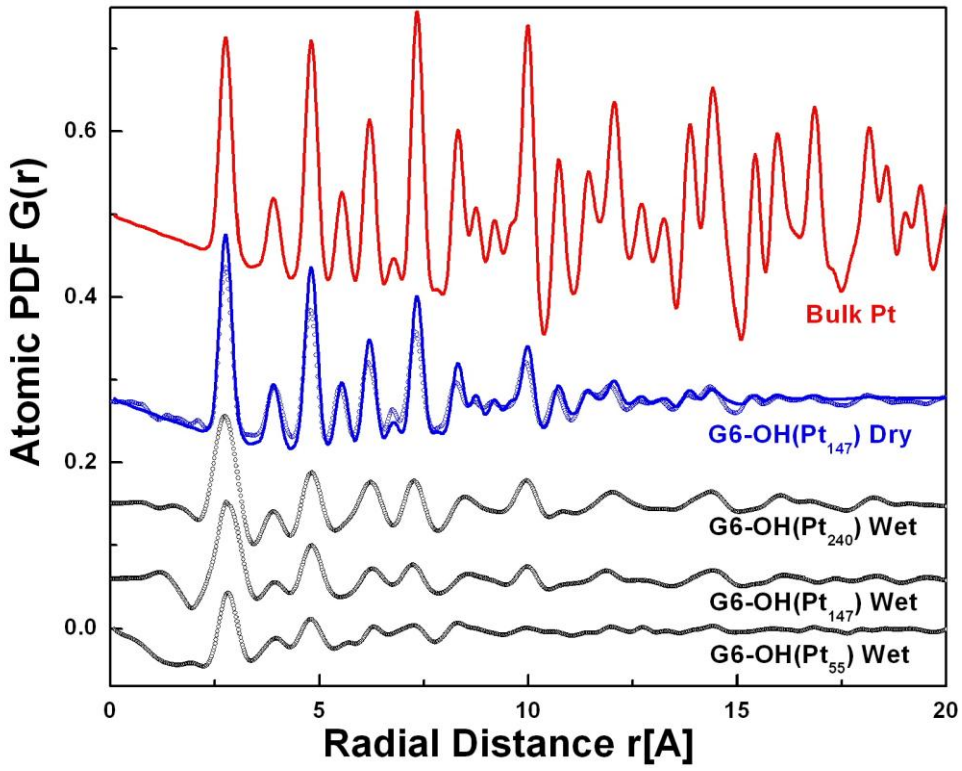

Figure 3.15. Experimental PDFs (symbols) for the indicated wet and dry Pt DENs. Model PDFs for bulk Pt (red plot) and a hypothetical 1.7 nm Pt particle with an fcc-type structure (blue plot) are also shown.

expected (1.6 nm) and measured (TEM: 1.6 ± 0.3 nm) values for the diameters of the G6-OH(Pt_{147}) DENs.

The experimental PDFs for wet Pt DENs resemble that of dry Pt DENs, but the plots are not as well-defined (broader peaks than for dry G6-OH(Pt_{147}) and bulk Pt). Also, the PDFs for wet DENs decay to zero at distances somewhat less than the average DEN size (0.9, 1.5, and 1.9 nm correlation lengths for the G6-OH(Pt^{2+})$_n$ (n = 55, 147, 240) wet DENs, respectively). Clearly, the atomic ordering in wet Pt DENs resembles that of an fcc-type structure, but they also exhibit considerable local structural distortions and/or strain. This may result in atomic ordering with a broken periodicity, as we have previously discussed.[60]

There are two other very important points relating to the XRD/PDF analyses. First, we have previously shown that the size of Au DENs (G6-OH(Au_{147})) measured by TEM (1.7 nm) and XRD/PDF is fully consistent with CNs determined by EXAFS.[60] That is, the CNs determined by EXAFS for dry and wet G6-OH(Au_{147}) DENs were found to be 9.6 and 9.0, respectively, which are very close to the CNs calculated for a 147-atom regular cuboctahedron (8.98) and that determined by XRD/PDF for dry and wet G6-OH(Au_{147}) (9 ± 1

nm). These results for Au DENs represent an important control experiment that unambiguously demonstrates that upon full reduction of all metal-ion/dendrimer complexes, TEM, EXAFS, and XRD/PDF yield identical results within the error limits inherent to these methods. This means that the differences in the EXAFS and XRD/PRF results measured for Pt DENs are real.

The second important point is that EXAFS measures the average CN for all metal atoms present in a sample: both Pt^{2+} and Pt^{0}. Therefore, the low CNs determined for the Pt DENs discussed here are consistent with partial reduction, but as mentioned earlier they do not provide information about the distribution of the reduced Pt. In contrast, and this is important, XRD/PDF is primarily sensitive to reduced Pt particles. Hence, taken together, the EXAFS and PDF data are fully consistent with a bimodal distribution of fully reduced and fully unreduced Pt DENs. Interestingly, Figure 3.14d clearly shows that the extent of reduction depends on the loading of the dendrimer with Pt^{2+}: higher loadings yield a higher percentage of reduced Pt^{2+}.

3.5 Summary and Conclusions

We undertook this study to reconcile previous reports from our lab[2] and others[4,5] that dendrimer complexes with Pt^{2+} are not fully reduced when exposed to BH_4^- in aqueous solutions. We expected to discover that each dendrimer consisted of the same average number of reduced and unreduced Pt^{2+} complex ions. However, the use of five powerful analytical methods: UV-vis spectroscopy, XPS, TEM, EXAFS, and XRD/PDF are consistent only with a model that invokes a bimodal distribution of reduced and unreduced intradendrimer Pt^{2+} (Scheme 3.1). Specifically, the UV-vis, XPS, and EXAFS data, which provide information about all Pt present within the sample regardless of its chemical state, indicate only partial reduction of G6-OH$(Pt^{2+})_n$. In contrast, TEM and XRD/PDF provide information only about reduced Pt^{2+} in the form of Pt nanoparticles. Because both TEM and XRD/PDF results reveal the presence of fully reduced DENs (that is, DENs having the correct size predicted based on the initial Pt^{2+}:G6-OH ratio used in the synthesis), we conclude that some dendrimers contain fully reduced DENs and some contain only Pt^{2+}. Importantly, TEM, EXAFS, and XRD/PDF studies carried out on Au DENs are internally self-consistent and all three methods indicate the presence of fully reduced Au

DENs.[60] This important set of control experiments instills confidence in the methodology used in the present study and the resulting conclusions.

We are left to ponder the seemingly counter-intuitive model that results from this study (Scheme 3.1). It may be reasonable to conclude that we are observing a stochastic, autocatalytic, intradendrimer nucleation and growth process. That is, for reasons we do not presently understand, BH_4^- is apparently capable of reducing Pt^{2+} complexed to the dendrimer via specific motifs.[36,46] Once reduction begins, however, it may become autocatalytic. That is, Pt^{2+} ions that are not directly susceptible to BH_4^- reduction may be catalytically reduced on the nascent Pt DEN. There is certainly ample prior evidence that Pt DENs are catalytic for hydrogenation reactions[28,34] and for decomposition of dendrimers,[4,61] which might support this hypothesis. Perhaps structural differences between dendrimers (that is, defect structures which are known to exist in PAMAM dendrimers to a substantial degree)[62] or different binding modalities between Pt^{2+} and the dendrimer[5,36] might account for this emergent heterogeneity. Certainly the data shown in Figure 9d, which shows that a

higher percentage of Pt^{2+} is reduced in dendrimers having a higher loading of Pt^{2+}, is consistent with this view. That is, from a purely statistical viewpoint, higher loadings of Pt^{2+} provide more opportunities for a nascent Pt^{0} nucleus to form.

Finally, we note that this bimodal reduction model is also consistent with our recently published study of the effect of Pt DEN size on the kinetics of the oxygen reduction reaction (ORR).[16] Specifically, this study indicated a monotonic trend in which smaller Pt particles resulted in slower ORR kinetics. This observation is more consistent with a bimodal distribution of Pt DEN catalysts that are fully formed (fully reduced), and hence catalytic, and a second distribution, which are unreduced and thus not catalytically active. If Pt within individual dendrimers was substantially present in multiple oxidation states, it is unlikely that catalytic activity approaching that of bulk Pt (for G6-OH(Pt_{240})) would have been observed because EXAFS indicates that such particles would have CNs on the order of 6. This CN corresponds to regular cuboctahedra consisting of just 13 atoms, which surely would have vastly different catalytic properties than bulk Pt.

References

1. Scott, R. W. J.; Wilson, O. M.; Crooks, R. M. *J. Phys. Chem. B* **2005**, *109*, 692-704.

2. Ye, H.; Scott, R. W. J.; Crooks, R. M. *Langmuir* **2004**, *20*, 2915-2920.

3. Ye, H.; Crooks, R. M. *J. Am. Chem. Soc.* **2005**, *127*, 4930-4934.

4. Ozturk, O.; Black, T. J.; Perrine, K.; Pizzolato, K.; Williams, C. T.; Parsons, F. W.; Ratliff, J. S.; Gao, J.; Murphy, C. J.; Xie, H.; Ploehn, H. J.; Chen, D. A. *Langmuir* **2005**, *21*, 3998-4006.

5. Alexeev, O. S.; Siani, A.; Lafaye, G.; Williams, C. T.; Ploehn, H. J.; Amiridis, M. D. *J. Phys. Chem. B* **2006**, *110*, 24903-24914.

6. Garcia-Martinez, J. C.; Lezutekong, R.; Crooks, R. M. *J. Am. Chem. Soc.* **2005**, *127*, 5097-5103.

7. Hoover, N. N.; Auten, B. J.; Chandler, B. D. *J. Phys. Chem. B* **2006**, *110*, 8606-8612.

8. Narayanan, R.; El-Sayed, M. A. *J. Phys. Chem. B* **2004**, *108*, 8572-8580.

9. Niu, Y.; Yeung, L. K.; Crooks, R. M. *J. Am. Chem. Soc.* **2001**, *123*, 6840-6846.

10. Scott, R. W. J.; Wilson, O. M.; Oh, S.-K.; Kenik, E. A.; Crooks, R. M. *J. Am. Chem. Soc.* **2004**, *126*, 15583-15591.

11. Wilson, O. M.; Knecht, M. R.; Garcia-Martinez, J. C.; Crooks, R. M. *J. Am. Chem. Soc.* **2006**, *128*, 4510-4511.

12. Chandler, B. D.; Gilbertson, J. D. *Top. Organomet. Chem.* **2006**, *20*, 97-120.

13. Vijayaraghavan, G.; Stevenson, K. J. *Langmuir* **2007**, *23*, 5279-5282.

14. Ye, H.; Crooks, R. M. *J. Am. Chem. Soc.* **2007**, *129*, 3627-3633.

15. Korkosz, R. J.; Gilbertson, J. D.; Prasfika, K. S.; Chandler, B. D. *Catal. Today* **2007**, *122*, 370-377.

16. Ye, H.; Crooks, J. A.; Crooks, R. M. *Langmuir* **2007**, *23*, 11901-11906.

17. Astruc, D. *Nanoparticles and Catalysis*; Wiley: New York, 2007.

18. Zhao, M.; Sun, L.; Crooks, R. M. *J. Am. Chem. Soc.* **1998**, *120*, 4877-4878.

19. Scott, R. W. J.; Ye, H.; Henriquez, R. R.; Crooks, R. M. *Chem. Mater.* **2003**, *15*, 3873-3878.

20. Knecht, M. R.; Garcia-Martinez, J. C.; Crooks, R. M. *Chem. Mater.* **2006**, *18*, 5039-5044.

21. Knecht, M. R.; Crooks, R. M. *New J. Chem.* **2007**, *31*, 1349-1353.

22. Kim, Y.-G.; Oh, S.-K.; Crooks, R. M. *Chem. Mater.* **2004**, *16*, 167-172.

23. Gröhn, F.; Bauer, B. J.; Akpalu, Y. A.; Jackson, C. L.; Amis, E. J. *Macromolecules* **2000**, *33*, 6042-6050.

24. Mark, S. S.; Bergkvist, M.; Yang, X.; Angert, E. R.; Batt, C. A. *Biomacromolecules* **2006**, *7*, 1884-1897.

25. Zhu, H.; Zhu, Y.; Yang, X.; Li, C. *Chem. Lett.* **2006**, *35*, 326-327.

26. Tran, M. L.; Zvyagin, A. V.; Plakhotnik, T. *Chem. Commun.* **2006**, *2006*, 2400-2401.

27. Knecht, M. R.; Weir, M. G.; Frenkel, A. I.; Crooks, R. M. *Chem. Mater.* **2008**, *20,* 1019-1028.

28. Scott, R. W. J.; Datye, A. K.; Crooks, R. M. *J. Am. Chem. Soc.* **2003**, *125*, 3708-3709.

29. Scott, R. W. J.; Sivadinarayana, C.; Wilson, O. M.; Yan, Z.; Goodman, D. W.; Crooks, R. M. *J. Am. Chem. Soc.* **2005**, *127*, 1380-1381.

30. Wilson, O. M.; Scott, R. W. J.; Garcia-Martinez, J. C.; Crooks, R. M. *J. Am. Chem. Soc.* **2005**, *127*, 1015-1024.

31. Lemon, B. I.; Crooks, R. M. *J. Am. Chem. Soc.* **2000**, *122*, 12886-12887.

32. Zheng, J.; Dickson, R. M. *J. Am. Chem. Soc.* **2002**, *124*, 13982-13983.

33. Zheng, J.; Petty, J. T.; Dickson, R. M. *J. Am. Chem. Soc.* **2003**, *125*, 7780-7781.

34. Zhao, M.; Crooks, R. M. *Angew. Chem., Int. Ed. Engl.* **1999**, *38*, 364-366.

35. Yeung, L. K.; Crooks, R. M. *Nano Lett.* **2001**, *1*, 14-17.

36. Pellechia, P. J.; Gao, J.; Gu, Y.; Ploehn, H. J.; Murphy, C. J. *Inorg. Chem.* **2004**, *43*, 1421-1428.

37. Lippard, S. J.; Berg, J. M. *Principals of Bioinorganic Chemistry*; 1 ed.; University Science Books: Mill Valley, California, 1994.

38. Rochon, F. D.; Fleurent, L. *Inorg. Chim. Acta* **1988**, *143*, 81-87.

39. Fu, X.; Wang, Y.; Wu, N.; Gui, L.; Tang, Y. *J. Colloid Interface Sci.* **2001**, *243*, 326-330.

40. Eberhardt, W.; Fayet, P.; Cox, D. M.; Fu, Z.; Kaldor, A.; Sherwood, R.; Sondericker, D. *Phys. Rev. Lett.* **1990**, *64*, 780-783.

41. You, T.; Niwa, O.; Horiuchi, T.; Tomita, M.; Iwasaki, Y.; Ueno, Y.; Hirono, S. *Chem. Mater.* **2002**, *14*, 4796-4799.

42. Tokuhisa, H.; Zhao, M.; Baker, L. A.; Phan, V. T.; Dermody, D. L.; Garcia, M. E.; Peez, R. F.; Crooks, R. M.; Mayer, T. M. *J. Am. Chem. Soc.* **1998**, *120*, 4492-4501.

43. Newville, M. *J. Synchrotron Rad.* **2001**, *8*, 322-324.

44. Elding, L. I.; Olsson, L. F. *J. Phys. Chem.* **1978**, *82*, 69-74.

45. Cotton, F. A.; Wilkinson, G.; Murillo, C. A.; Bochmann, M. *Advanced Inorganic Chemistry*; Wiley: New York, 1999.

46. Tarazona-Vasquez, F.; Balbuena, P. B. *J. Phys. Chem. A* **2007**, *111*, 945-953.

47. Zhang, Y.; Guo, Z.; You, X.-Z. *J. Am. Chem. Soc.* **2001**, *123*, 9378-9387.

48. Baik, M.-H.; Friesner, R. A.; Lippard, S. J. *J. Am. Chem. Soc.* **2003**, *125*, 14082-14092.

49. Fanizzi, F. P.; Intini, F. P.; Maresca, L.; Natile, G. *J. Chem. Soc., Dalton Trans.* **1990**, 199.

50. Grantham, L. R.; Elleman, T. S.; Martin, D. S. *J. Am. Chem. Soc.* **1955**, 77, 2965-2971.

51. Creighton, J. A.; Eadon, D. G. *J. Chem. Soc., Faraday Trans.* **1991**, *87*, 3881-3891.

52. Wagner, C. D.; Riggs, W. M.; Davis, L. E.; Moulder, J. F. *Handbook of X-Ray Photoelectron Spectroscopy*; Perkin-Elmer Corporation: Chanhassen, MN, 1995.

53. Zhao, M.; Crooks, R. M. *Adv. Mater.* **1999**, *11*, 217-220.

54. Matsumoto, K.; Sakai, K.; Nishio, K.; Tokisue, Y.; Ito, R.; Nishide, T.; Shichi, Y. *J. Am. Chem. Soc.* **1992**, *114*, 8110-8118.

55. Wang, J. J.; Ying, G. P.; Zhang, J.; Wang, Z. B.; Gao, Y. Z. *Electrochim. Acta* **2007**, *52*, 7042-7050.

56. Rehr, J. J.; Albers, R. C.; Zabinsky, S. I. *Phys. Rev. Lett.* **1992**, *69*, 3397-3400.

57. Ravel, B.; Newville, M. *J. Synchroton Rad.* **2005**, *12*, 537-541.

58. Glasner, D.; Frenkel, A. I. *XAFS13 Conference Proceedings* **2007**, *882*, 746-748.

59. Egami, T.; Billinge, S. J. L. *Underneath the Bragg Peaks*; Pergamon Press: Amsterdam, 2003.

60. Petkov, V.; Bedford, N.; Knecht, M. R.; Weir, M. G.; Crooks, R. M.; Tang, W.; Henkelman, G.; Frenkel, A. I. *J. Phys. Chem. C,* **2008**, *112*, 8907-8911.

61. Singh, A.; Chandler, B. D. *Langmuir* **2005**, *21*, 10776-10782.

62. Tomalia, D. A.; Baker, H.; Dewald, J.; Hall, M.; Kallos, G.; Martin, S.; Roeck, J.; Ryder, J.; Smith, P. *Polym. J.* **1985**, *17*, 117-132.

Chapter 4: Structural Rearrangement of Bimetallic Alloy PdAu Nanoparticles within Dendrimer Templates to Yield Core/Shell Configurations

4.1 Synopsis

Here we present evidence for an oxidation-driven structural conversion of quasi-alloy PdAu dendrimer-encapsulated nanoparticles (DENs) to a Au-core/Pd-shell configuration. The initial quasialloy was prepared by co-complexation of $PdCl_4^{2-}$ and $AuCl_4^-$ within a sixth-generation, poly(amidoamine) dendrimer template followed by chemical reduction. Exposure to air resulted in selective reoxidation of the Pd atoms and subsequent re-reduction led to deposition of a Pd-rich shell on the surface of the remaining Au core. The core/shell nanoparticles were extracted as monolayer-protected clusters (MPCs) from within the dendrimer templates using dodecanethiol. The resulting materials were characterized by UV—vis spectroscopy, transmission electron microscopy, and extended X-ray absorption fine structure (EXAFS) spectroscopy.

4.2 Introduction

Here we report a detailed, atomic-level structural study of bimetallic nanoparticles containing an average of 147 atoms synthesized using dendrimer templates.[1] Extended X-ray absorption fine structure (EXAFS) spectroscopy indicates that co-complexation of two metal complexes (K_2PdCl_4 and $HAuCl_4$) with the dendrimer followed by chemical reduction results in formation of zerovalent PdAu quasi-random, dendrimer-encapsulated nanoparticle (DEN) alloys.[1-3] The elemental composition of these DENs reflects the stoichiometry of the Pd and Au complexes used for the synthesis.[4,5] Extraction of the nanoparticles from the dendrimers using alkanethiols results in conversion of the PdAu alloy DENs to monolayer-protected clusters (MPCs)[6-9] having a Au-rich core and a Pd-rich shell (Scheme 4.1). The results reported here are significant for two reasons. First, PdAu DENs synthesized by co-complexation[1] result in a quasirandom alloy structure, regardless of the relative ratios of the two metals used for the synthesis. Second, EXAFS analysis before and after extraction provides direct evidence for oxidation-driven conversion of a quasirandom alloy nanoparticle to a core/shell structure.

Scheme 4.1

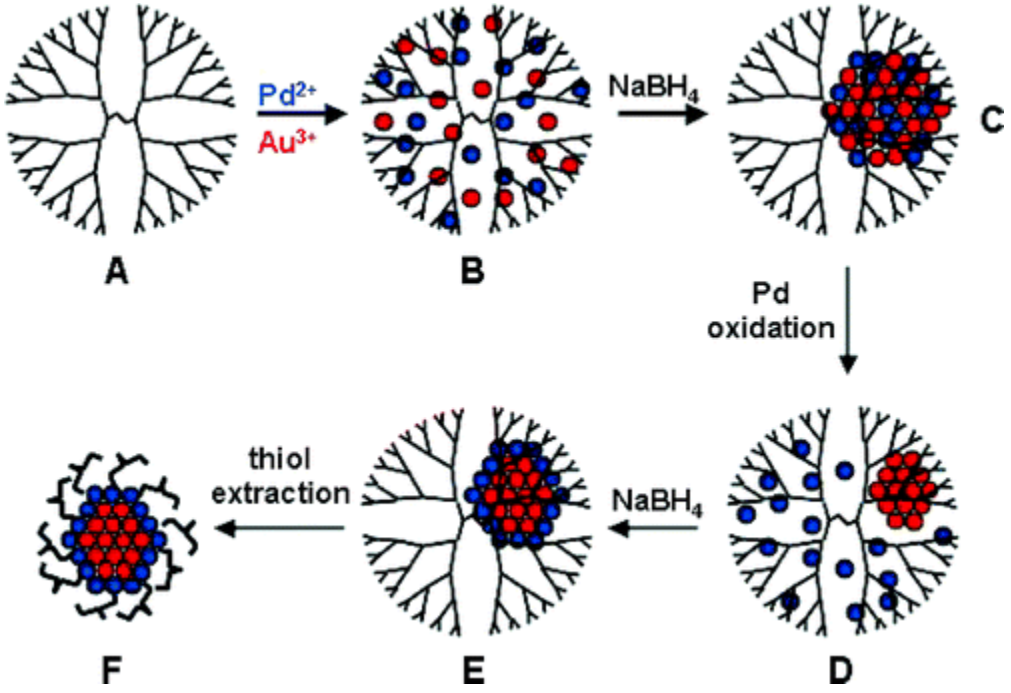

Multimetallic nanoparticles and surfaces often improve the selectivities and rates of metal-catalyzed reactions.[2,5,10,11] For example, the hydrogenation rate of simple olefins is increased in the presence of Pd catalysts containing 20% Au compared to monometallic Pd catalysts.[5, 11-14] This increase in activity has been attributed to the electronegativity of the Au atoms, which renders the Pd atoms electron deficient and thus enhances their interaction with the olefinic double bond. Additionally, Pârvulescu et al. have shown that PdAu alloy nanoparticles selectively catalyze the hydrogenation of cinnamaldehyde to cinnamyl alcohol over 3-phenyl-1-propanol, which is the preferred product in the presence of monometallic Pd catalysts.[15] Selectivity effects such as this are of particular interest for reactions in which multiple reactive functional groups are present on the same substrate molecule. Finally, Goodman and co-workers have studied the PdAu-catalyzed conversion of potassium acetate to vinyl acetate (VA) and found that the reaction rate was maximized when 0.07 monolayers of Pd were alloyed into a Au(100) surface.[16] There are many other examples demonstrating interesting catalytic properties of PdAu bimetallic surfaces and nanoparticles.[4,5,11-25]

A number of methods have been developed for synthesizing PdAu bimetallic nanomaterials, but one of two general approaches is typically used: simultaneous[4,5,13,15,22,26-30] or sequential[5,20,31,32] reduction of appropriate precursors. For simultaneous reduction, a solution containing Pd^{2+}, Au^{3+}, and a surface passivant is prepared, and reduction is then usually initiated using the polyol method[12,17,20] or by addition of borohydride.[5,15,28,33] Polyol reduction often results in formation of Au-core/Pd-shell nanoparticles[12,13,26,27,29] because of the difference in the reduction potentials of the two metal ions: Au reduces more easily and provides a seed for the reduction of the Pd shell. The sizes of both the core and shell can be controlled by the ratio of Pd:Au used for the synthesis.[13] Conversely, reduction using borohydride derivatives, either in aqueous or organic solvents, typically produces PdAu alloy nanoparticles,[15,28,33] but at least one group has reported formation of a Au-core/Pd-shell structure.[30] The difference between the two reduction methods is likely attributable to differences in relative reducing power of aldehyde groups (polyol synthesis) versus borohydride; the former is a weaker reducing agent than the latter and thus it preferentially initiates the reduction of Au first.

The second approach for preparing bimetallic nanoparticles relies on sequential reduction of two different types of metal ions. In this method, a monometallic core is synthesized first, and then in a second step, the second metal is reduced onto the core surface. This method has been used to synthesize PdAu alloy,[20] Au-core/Pd-shell,[31] and Pd-core/Au-shell[21,32] nanoparticles. Interestingly, the polyol process has been used to sequentially reduce first Pd^{2+} and then Au^{3+} in the presence of a polymer stabilizer at temperatures ranging from 100 to 190 °C.[20] However, because of the elevated temperature, an alloy, rather than a Pd-core/Au-shell structure, resulted from this synthesis.

We have previously reported a template method for synthesizing nanoparticles ranging in size from just a few atoms to about 300.[1,3] This approach has been used to prepare monometallic nanoparticles,[34-36] alloy and core–shell bimetallic nanoparticles,[2,5,6,10,47-49] and semiconducting quantum dots.[50] These DENs are synthesized in two steps. First, metal ions are mixed with the dendrimer template, and in favorable cases, fixed stoichiometries of the metal ions complex with interior functional groups of the

dendrimer. Second, a reducing agent is added to this mixture, which results in reduction of the ions within the dendrimer. Subsequently, the atoms agglomerate to yield particles having sizes that reflect the initial metal-ion-to-dendrimer ratio. Variations of this basic approach can lead to multimetallic core/shell or alloy nanoparticles.[2,5,6,10,47-49] Because the dendrimer is porous, the surface of DENs have been found to be catalytically active for homogeneous[2,40,42,45,51,52] and electrocatalytic[43,49,53] reactions. Finally, it is possible to remove the dendrimer and carry out catalytic reactions on the naked nanoparticles.[4,38,47,48,54]

Because of their small size, the characterization of DENs presents some interesting analytical challenges. For simple, monometallic DENs, electron microscopy and UV–vis spectroscopy are useful; however, more sophisticated methods are required to achieve a complete understanding of these materials and particularly of the more complex multimetallic DENs. For example, NMR, EXAFS, and X-ray photoelectron spectroscopy (XPS) have been used to characterize DENs before and after reduction.[43,55-57] Additionally, we have introduced two chemical

characterization methods based on selective catalytic reactions[5,11] and selective extraction that complement instrumental methods of analysis.[6-9] These approaches are particularly useful for understanding the structure and composition of multimetallic DENs. For example, in the extraction method, an aqueous DEN solution is mixed with an organic phase containing a hydrophobic ligand that binds preferentially with one of the two metals comprising the particle. If the ligand is selective for a metal present on the surface, then it will adsorb to the nanoparticle surface and in many cases extract the particle from within the dendrimer template.[8,9] This extraction method has been used to speciate nanoparticle mixtures,[7] determine the surface oxidation states of nanoparticles,[6] and distinguish between core and shell metals.[6]

Here we use the DEN extraction method, EXAFS, TEM, and UV–vis spectroscopy to better understand the properties of PdAu bimetallic DENs prepared by co-complexation. DENs consisting of an average of 147 atoms and having five different Pd:Au ratios were synthesized and characterized. EXAFS results indicate that co-complexation of $AuCl_4^-$ and $PdCl_4^{2-}$ with sixth-generation, hydroxyl-terminated

poly(amidoamine) (PAMAM) dendrimers (G6-OH) followed by chemical reduction results in formation of zerovalent PdAu DENs having a quasirandom alloy structure regardless of the metal-ion-to-dendrimer ratio used. After extraction of the DENs into hexanes using dodecanethiol ligands, EXAFS indicates that a structural rearrangement occurs that yields MPCs[58] having Au-rich cores and Pd-rich shells (Scheme 4.1). The structural model for both the DENs and MPCs are supported by TEM and UV–vis results.

4.3 Experimental

Chemicals

G6-OH PAMAM dendrimers were purchased from Dendritech, Inc. (Midland, MI) as an 11.47 wt% solution in methanol. Prior to use, the methanol was removed under a vacuum at 25 °C, and a 100 μM stock solution was prepared in water. $HAuCl_4 \cdot 3H_2O$, K_2PdCl_4, $NaBH_4$, and dodecanethiol were purchased from Sigma-Aldrich (Milwaukee, WI). Hexanes and methanol were purchased from Fisher Scientific (Pittsburgh, PA), and absolute ethanol was purchased from Aaper Chemical Co. (Shelbyville, KY). Unless otherwise noted, all chemicals

were used as received. 18.0 MΩ cm Milli-Q water (Millipore, Bedford, MA) was used throughout.

Characterization

UV–vis absorbance spectra were obtained using a Hewlett-Packard HP8453 spectrometer and quartz cuvettes having an optical path length of 1.00 cm. Depending on the sample, a spectrum of either 2.00 μM G6-OH in water or neat hexanes (no dendrimer) was used as the background. TEM micrographs were obtained using a JEOL-2010F TEM operating at 200 kV. Samples were prepared by dropwise addition of the solution-phase materials onto a 20 nm thick, carbon-coated, 400 mesh Cu grid (EM Sciences, Gibbstown, NJ) followed by solvent evaporation under a vacuum.

EXAFS analysis was conducted at beamline X18B of the National Synchrotron Light Source at the Brookhaven National Laboratory. The nanoparticle samples were dried to a powder and then dispersed onto adhesive tape. The tapes were folded multiple times to ensure homogeneity. The samples were measured in fluorescence mode, using an Ar-filled, five-grid Lytle detector, with the sample positioned at a 45° angle relative to the incident beam. X-

ray absorption coefficients were measured from 150 eV below to 1100 and 1250 eV above the Pd K and Au L_3-edges, respectively. The X-ray energy was calibrated prior to examination of each metallic edge by analysis of the corresponding bulk metal foil. EXAFS data were analyzed using the IFEFFIT software package.[59]

Synthesis of PdAu Alloy DENs

Synthesis of G6-OH($Pd_xAu_{(147-x)}$) (x = 118, 87, 73, 60, 29) DENs generally followed standard literature procedures, but larger volumes were required to provide enough material for EXAFS analysis.[5] For example, the synthesis of G6-OH($Pd_{118}Au_{29}$) was carried out as follows, and except for differences in the metal-ion-to-dendrimer ratio, an identical procedure was used for the other DENs. First, 5.0 mL of a 100 μM G6-OH stock solution was diluted in 237.0 mL of water. Second, 118 equiv of a freshly prepared 10.0 mM K_2PdCl_4 solution in water (5.90 mL) was added to this solution to yield the metal-ion/dendrimer complex denoted as G6-OH(Pd^{2+})$_{118}$. The solution was allowed to stir for 30 min to ensure complete complexation. Third, 29 equiv of a 10.0 mM $HAuCl_4$ solution in water (1.45 mL) was added to the G6-OH(Pd^{2+})$_{118}$ solution. Finally, after the solution was

stirred for <1 min, a 10-fold molar excess of a 1.00 M $NaBH_4$ solution, prepared in 0.30 M NaOH, was added to reduce the metal ions within the dendrimer. The final volume of the solution was 250 mL. Reduction was allowed to proceed for at least 15 min prior to analysis. Note that hydroxyl functionalities are known to reduce Au salts to zerovalent metals,[35,60] and therefore, it is important that the $NaBH_4$ reduction be carried out quickly after addition of $HAuCl_4$. DEN samples used for EXAFS were dried by lyopholization (Freezone 12, Labconco Corp.) for ~15 min after initiation of reduction.

Extraction of DENs

Extraction of the PdAu alloy DENs (part C and D of Scheme 4.1) was carried out 2 h after the initial reduction using a previously described method.[6,8,9] The solutions were exposed to air during this period and during the extraction process, which results in deactivation (oxidation) of the BH_4^- and oxidation of zerovalent Pd within the DENs. Briefly, 125 mL of an aqueous 2.00 μM DEN solution was placed into a separatory funnel. Second, a 100-fold excess of solid $NaBH_4$ was added with respect to the total metal concentration. Next, 125 mL of a 29.4 mM dodecanethiol

solution, prepared in hexanes, was layered atop the aqueous solution. The separatory funnel was shaken vertically and vigorously for 5 min, and then allowed to settle for ~10 min. After settling, the organic phase was removed and concentrated on a rotary evaporator to a volume of ~5.00 mL. The resulting MPCs were then precipitated with absolute ethanol to separate them from excess dodecanethiol, and the precipitate was collected by centrifugation. The supernatant was decanted and the MPCs were redissolved in a minimal volume of hexanes. The concentrated solution was then evaporated under a vacuum at 35 °C until dry.

4.4 Results and Discussions

Synthesis of PdAu DENs

As discussed in the Experimental Section, the metal-ion/dendrimer precursor was prepared by sequential addition first of $PdCl_4^{2-}$ and then, after 30 min,[41] $AuCl_4^-$, followed by co-reduction. This was necessary because completion of the reaction between $PdCl_4^-$ and the interior tertiary amines of the dendrimer takes ~15 min, but reduction of the metal-ion/dendrimer complex must be carried out immediately after addition of $AuCl_4^-$ (which enters the dendrimer very quickly)

because $AuCl_4^-$ can be prematurely reduced by hydroxyl groups present on the dendrimer periphery. If that happens, large Au aggregates form that are stabilized by multiple dendrimers adsorbed to the metal surface.[35,60,61] Reduction of the metal-ion/dendrimer composite resulted in an immediate color change from pale yellow to brown.

Basic Characterization of PdAu DENs

UV–vis spectroscopy was used to monitor the reaction progress of DEN formation, beginning with Pd-ion complexation and concluding with metal-ion reduction. The UV–vis absorbance spectra of the G6-OH$(Pd^{2+})_n$ (n = 29, 60, 73, 87, and 118) species prior to addition of Au^{3+} are shown in Figure 4.1a. The prominent band at 221 nm arises from a ligand-to-metal charge transfer (LMCT) between interior amines of the dendrimer and Pd^{2+}.[41] The absorbance of this peak as a function of concentration is linear, indicating an uncomplicated interaction between the Pd complex and the dendrimer. It was not possible to obtain UV–vis spectra of the dendrimer composite with both $PdCl_4^{2-}$ and $AuCl_4^-$, because as mentioned previously, hydroxyl groups on the surface of the dendrimer reduce the Au complex within a shorter period of time than is required to obtain a reliable spectrum.

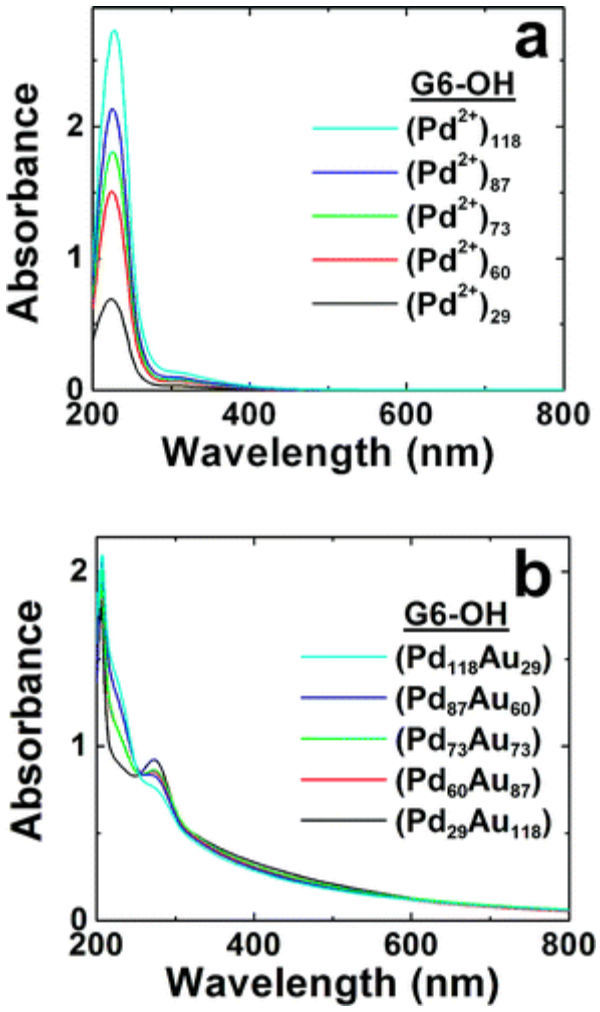

Figure 4.1. UV—vis spectra of the metal-ion/dendrimer complexes (a) before and (b) after reduction. (a) Only the Pd^{2+} complex is shown, because the dendrimer itself quickly reduces $AuCl_4^-$.

UV–vis spectra of the DENs obtained after complexation with $AuCl_4^-$ and subsequent reduction with BH_4^- are shown in Figure 4.1b. In all cases, the absorbance increases as the wavelength decreases, which is consistent with the presence of nanoscale particles.[62] Additionally, the LMCT band present in Figure 4.1a at 221 nm is absent, indicating essentially complete reduction of the Pd complex. We have not been able to unambiguously identify the small peak at 285 nm, but as discussed later, it may arise from the dendrimer itself.[63] The erratic behavior at $\lambda < 205$ nm results from imperfect background subtraction of the dendrimer-only solution.

TEM analysis of the particles and their size distribution histograms are provided in Figure 4.2. Analysis of 100 randomly selected nanoparticles indicate size distributions of 1.4 ± 0.3 nm for G6-OH($Pd_{118}Au_{29}$), 1.5 ± 0.2 nm for G6-OH($Pd_{73}Au_{73}$), and 1.5 ± 0.3 nm for all of the other PdAu DENs. These values are consistent with the calculated diameter of a 147-atom PdAu DEN having a cuboctahedral shape (1.5 nm).[1]

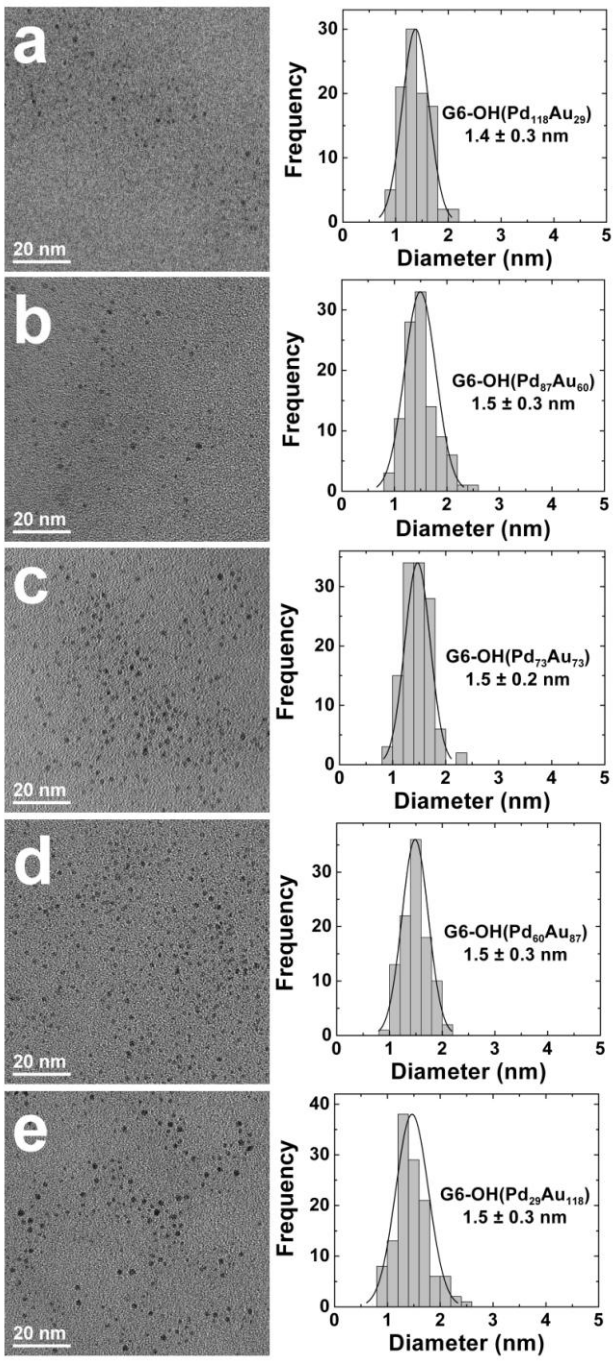
a
20 nm
Frequency
Diameter (nm)
G6-OH(Pd118Au29)
1.4 ± 0.3 nm
b
20 nm
Frequency
Diameter (nm)
G6-OH(Pd87Au60)
1.5 ± 0.3 nm
c
20 nm
Frequency
Diameter (nm)
G6-OH(Pd73Au73)
1.5 ± 0.2 nm
d
20 nm
Frequency
Diameter (nm)
G6-OH(Pd60Au87)
1.5 ± 0.3 nm
e
20 nm
Frequency
Diameter (nm)
G6-OH(Pd29Au118)
1.5 ± 0.3 nm

Figure 4.2. TEM micrographs and particle-size distribution histograms for the indicated compositions of the PdAu DENs.

Extraction of PdAu DENs

The method used to extract DENs from within dendrimers has been described in detail previously[6-9] and is briefly discussed in the Experimental Section. Mechanistically, we believe that hydrophobic ligands (dodecanethiol in this case) present in a water/hexanes emulsion penetrate the dendrimer periphery and adsorb to the surface of the encapsulated metal nanoparticle. When the number of ligands bound to the DEN surface exceeds a critical threshold, the particle extracts from the dendrimer as a hydrophobic MPC. In the case of monometallics, the size and optical properties of the MPCs are, within the resolution of the measurements, identical to the parent DENs.[7-9] We have also found that the extraction is dependent on the type of metal present on the surface of the DEN, its oxidation state, and the type of ligand present in the organic phase.[6,7]

The five bimetallic PdAu DENs prepared for this study were extracted using dodecanethiol, and the resulting MPCs were analyzed by UV–vis spectroscopy. Figure 4.3a provides spectra for the original, aqueous G6-OH($Pd_{118}Au_{29}$) DENs as well as for the aqueous and organic phases after extraction. Spectra for the other four PdAu DENs follow the

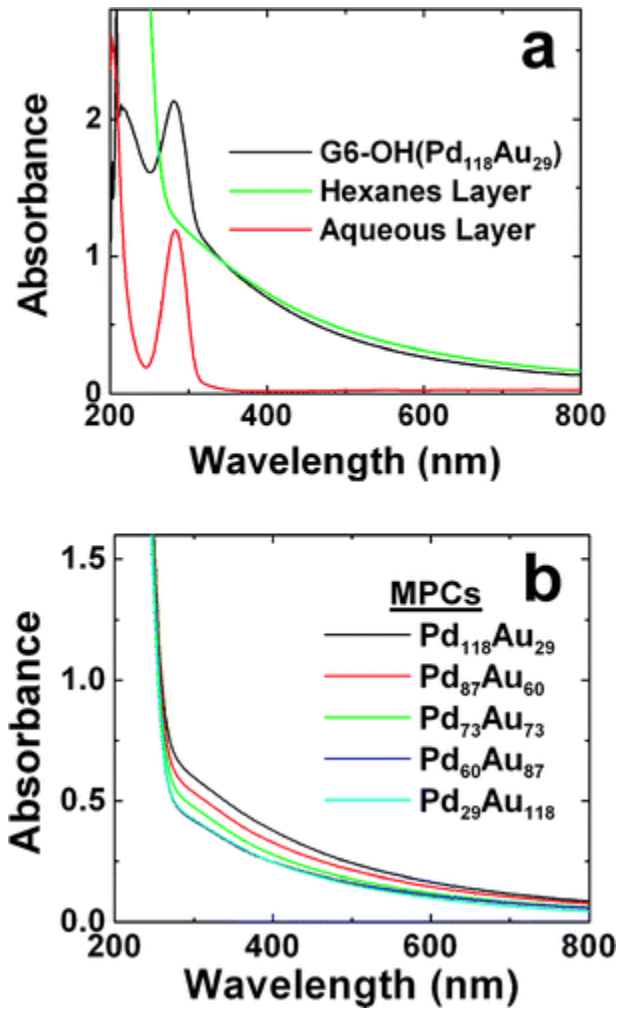

Figure 4.3. UV–vis spectroscopic analysis of the extraction process. (a) Spectra of the water-soluble G6-OH($Pd_{118}Au_{29}$) DENs prior to extraction, the aqueous layer after extraction with dodecanethiol, and the thiol-passivated $Pd_{118}Au_{29}$ MPCs after extraction. (b) UV–vis spectra of all the extracted PdAu MPCs.

same trends and are provided in Figure 4.4. Prior to extraction, the spectrum of the water-soluble G6-OH($Pd_{118}Au_{29}$) DENs exhibit an increase in absorbance at lower wavelengths, which is characteristic of small metal nanoparticles,[62] and two peaks. The peak at 285 nm probably arises from the dendrimer, because it is retained in the aqueous phase after extraction (vide infra), but its origin is uncertain at this time. The feature at 205 nm arises from imperfect background subtraction and is actually just the continuation of the rising baseline.[9,35,64]

After extraction, the spectrum of the aqueous layer did not exhibit the rising baseline characteristic of the metal nanoparticles, indicating transfer of the metal nanoparticles to the organic phase. However, as mentioned earlier, the peak at 285 nm is retained, suggesting that it arises from the water-soluble dendrimer[63,65] rather than being associated with the metal nanoparticles. The spectrum of the organic phase tracks the rising baseline of the pre-extraction spectrum, indicating that the metal nanoparticles have been quantitatively transferred as MPCs. The very rapidly rising part of this spectrum ($\lambda \leq 250$ nm) arises from absorbance by the solvent (hexanes). Figure

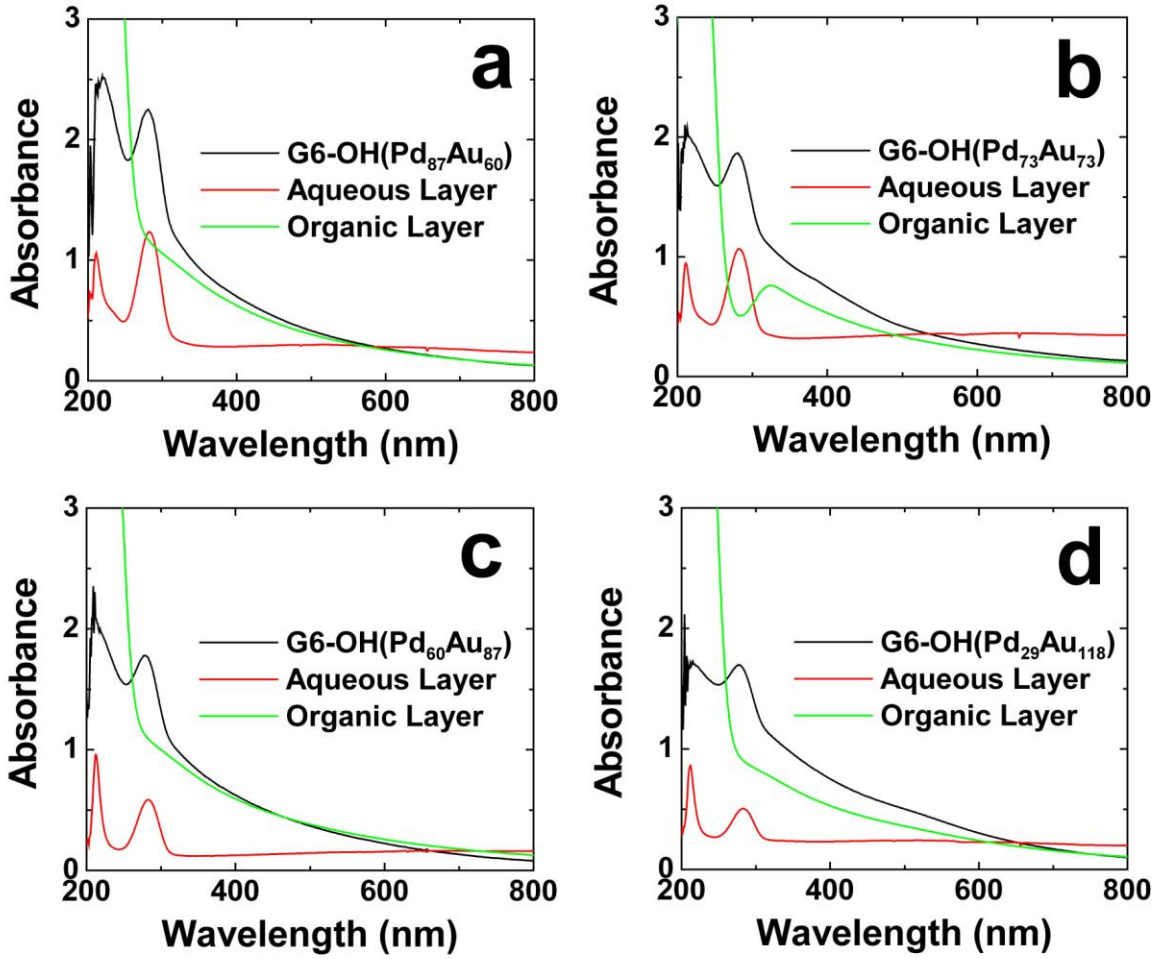

Figure 4.4. UV-vis spectroscopic analysis of the extraction process using dodecanethiol for (a) G6-OH($Pd_{87}Au_{60}$), (b) G6-OH($Pd_{73}Au_{73}$), (c) G6-OH($Pd_{60}Au_{87}$), and (d) G6-OH($Pd_{29}Au_{118}$) DENs. The black spectra represent the DENs prior to extraction in aqueous solution, the red spectra represent the aqueous layer after extraction, and the green spectra are associated with the organic layer after extraction.

4.3b shows the UV–vis spectra of all five bimetallic MPCs after extraction into the organic phase. These absorbance spectra are comparable to the corresponding spectra obtained prior to extraction (Figure 4.1b). This suggests that the DENs are quantitatively extracted into the organic phase as MPCs regardless of their elemental composition. Slight variations in absorbance before and after extraction may arise from incomplete settling of the microemulsion as well as from changes in the nanoparticle structure (vide infra). As in Figure 4.3a, the rapidly rising baseline in Figure 4.3b for $\lambda \leq 250$ nm arises from absorbance by the solvent.

TEM micrographs and the corresponding size-distribution histograms for the five MPCs are provided in Figure 4.5. Comparison of these data with those in Figure 4.2 indicate that extraction does not result in a significant change in average nanoparticle size, although the size distribution does vary slightly.

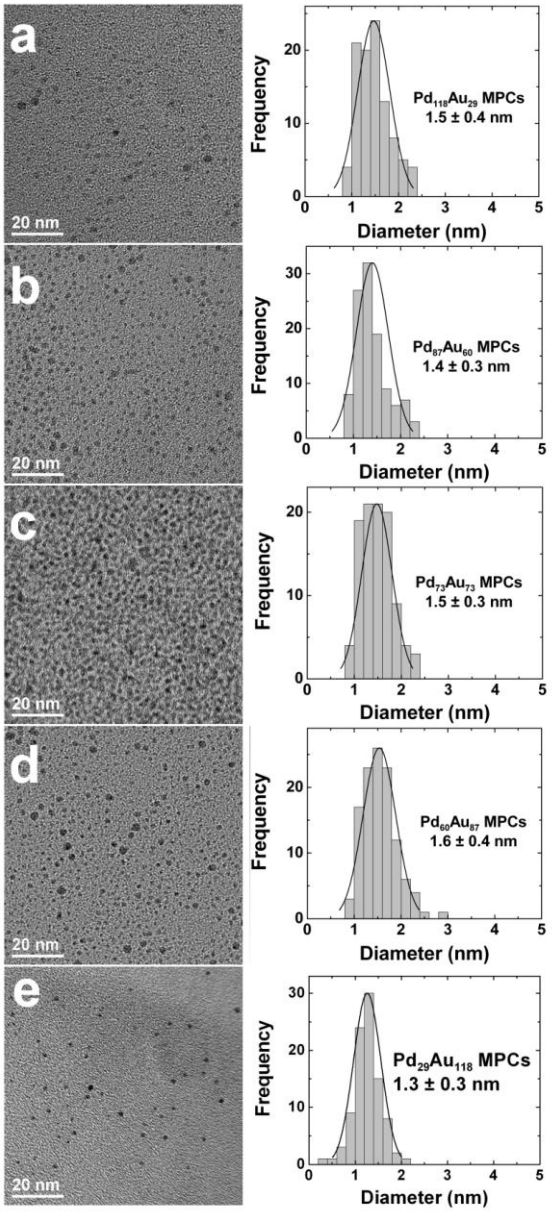

Figure 4.5. TEM micrographs and particle-size distribution histograms for the PdAu MPCs after extraction with dodecanethiol.

Principles of Quantitative Analysis of Size, Structure, and Compositional Distributions of Bimetallic Nanoparticles by EXAFS

EXAFS analysis of bimetallic alloys provides accurate information about the short-range order around alloyed elements, A and B, through the measurement of partial coordination numbers n_{AA}, n_{AB}, n_{BA}, and n_{BB}. The analysis should be done concurrently for the data collected at A and B absorbing atoms, with the following constraints imposed on the heterometallic bonds during the fits.[66]

$$n_{AB} = \frac{x_B}{x_A} n_{BA} \qquad (1)$$

$$R_{AB} = R_{BA} \qquad (2)$$

$$\sigma^2_{AB} = \sigma^2_{BA} \qquad (3)$$

Here, x_A and x_B are elemental compositions. If atoms of type A segregate to the surface of the nanoparticle and the atoms of type B to the core, then $n_{AM} < n_{BM}$, where $n_{AM} = n_{AA} + n_{AB}$ and $n_{BM} = n_{BB} + n_{BA}$, because atoms at the surface have fewer neighbors than those in the core. Random bimetallic alloys have a unique dependence of these coordination numbers (CN) on the alloy concentration. Assume, for

simplicity, a bimetallic nanoparticle of a certain size, with a random distribution of A and B atoms, where the following relationships apply.[67]

$$n_{AM} = n_{BM} = n_{MM} \quad (4)$$

$$n_{AA} = n_{BA} = x_A n_{MM} \quad (5)$$

$$n_{BB} = n_{AB} = x_B n_{MM} = (1 - x_A) n_{MM} \quad (6)$$

This analysis indicates that partial CNs should depend linearly on alloy concentration in random nanoalloys, provided that the particle size is the same at all concentrations (Figure 4.6).

To characterize their short-range order, EXAFS analyses of the bimetallic PdAu nanoparticles was completed for both the DENs and MPCs. For each edge (Pd or Au), up to four consecutive X-ray absorption energy scans were aligned in energy and averaged to minimize statistical noise. The Au and Pd EXAFS data of the same sample were subsequently fit simultaneously in *r*-space using the IFEFFIT software package.[59] CNs, bond lengths, and their disorders, as measured for the Pd–Au bonds from Pd and Au edges, were constrained by eqs 1–3.

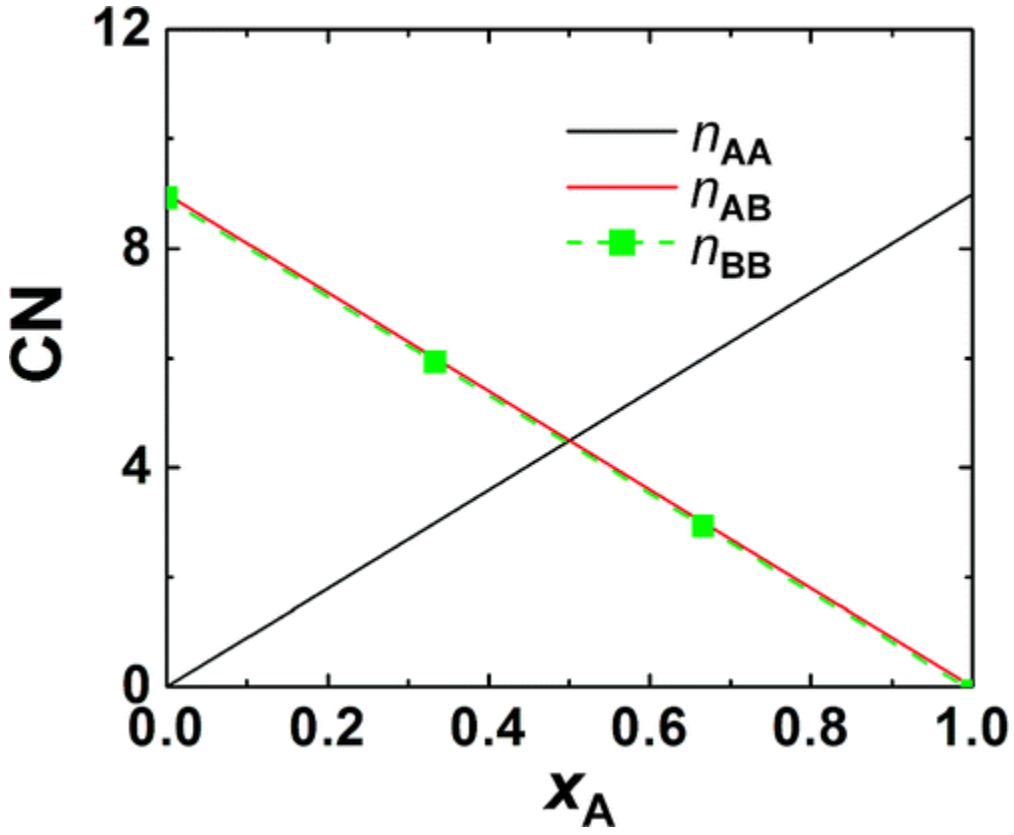

Figure 4.6. Theoretical partial CNs in random nanoalloys (assuming n_{MM} = 9) as a function of composition.

EXAFS Characterization of DENs

Figure 4.7 shows the experimentally obtained Au and Pd EXAFS data for the G6-OH($Pd_{29}Au_{118}$) and G6-OH($Pd_{118}Au_{29}$) DENs, the theoretical fits, trends in CN, and the nearest-neighbor distances. The fitting analysis for other metal ratios is provided in Figure 4.8. Panels e and f in Figure 4.7 compare the experimentally obtained first nearest-neighbor metal–metal CNs for the DENs. The CNs scale linearly with the Pd concentration (Figure 4.7e), similar to the ideal random alloy behavior (eq 6 and Figure 4.6). The difference between the ideal random alloy and the DENs is that CN(Au–M) exceeds CN(Pd–M) over the entire ratio range, as shown in Figure 4.7f. This result indicates that more Pd atoms reside on the surface of the particles than would be anticipated for a random alloy. This means that the PdAu DENS are quasirandom alloys with a Au-rich core and a Pd-rich shell. Finally, as shown in Figure 4.7g, the Au–Au, Pd–Au, and Pd–Pd bond distances in the DENs behave as expected for random alloys, because they gradually decrease from the longest values (at low Pd concentrations)

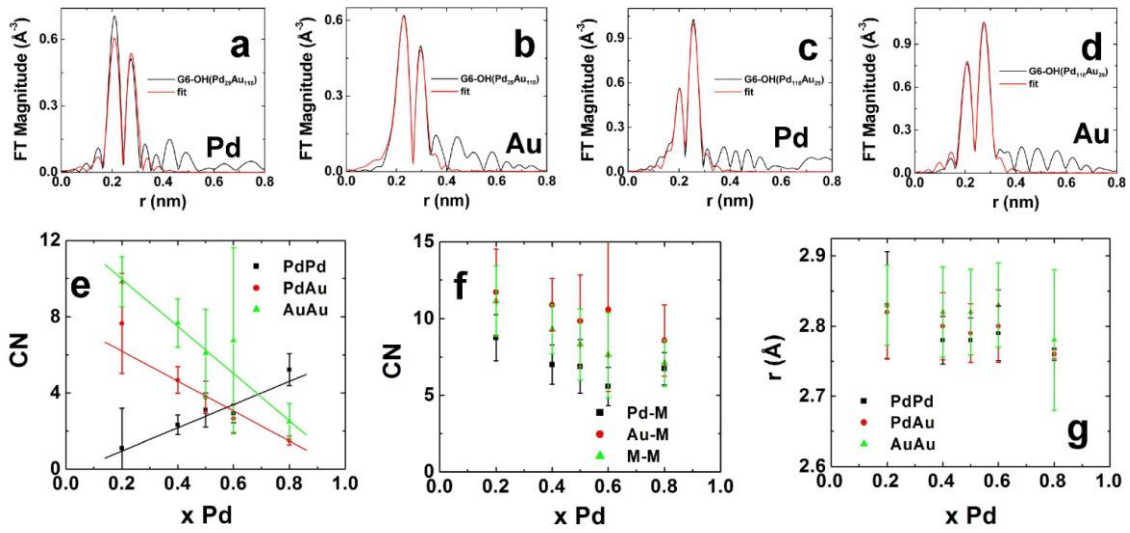

Figure 4.7. EXAFS data and the corresponding fitting analyses for the Pd K-edge and Au L_3-edge EXAFS for (a, b) G6-OH($Pd_{29}Au_{118}$) and (c, d) G6-OH($Pd_{118}Au_{29}$) DENs. In parts a–d, the data are plotted in black and the simulated fits are plotted in red. (e) Experimentally obtained partial CNs for Pd–Pd, Pd–Au, and Au–Au DENs. (f) Pd–M, Au–M, and M–M CNs as a function of Pd composition. (g) Metal–metal bond lengths for the PdAu DENs.

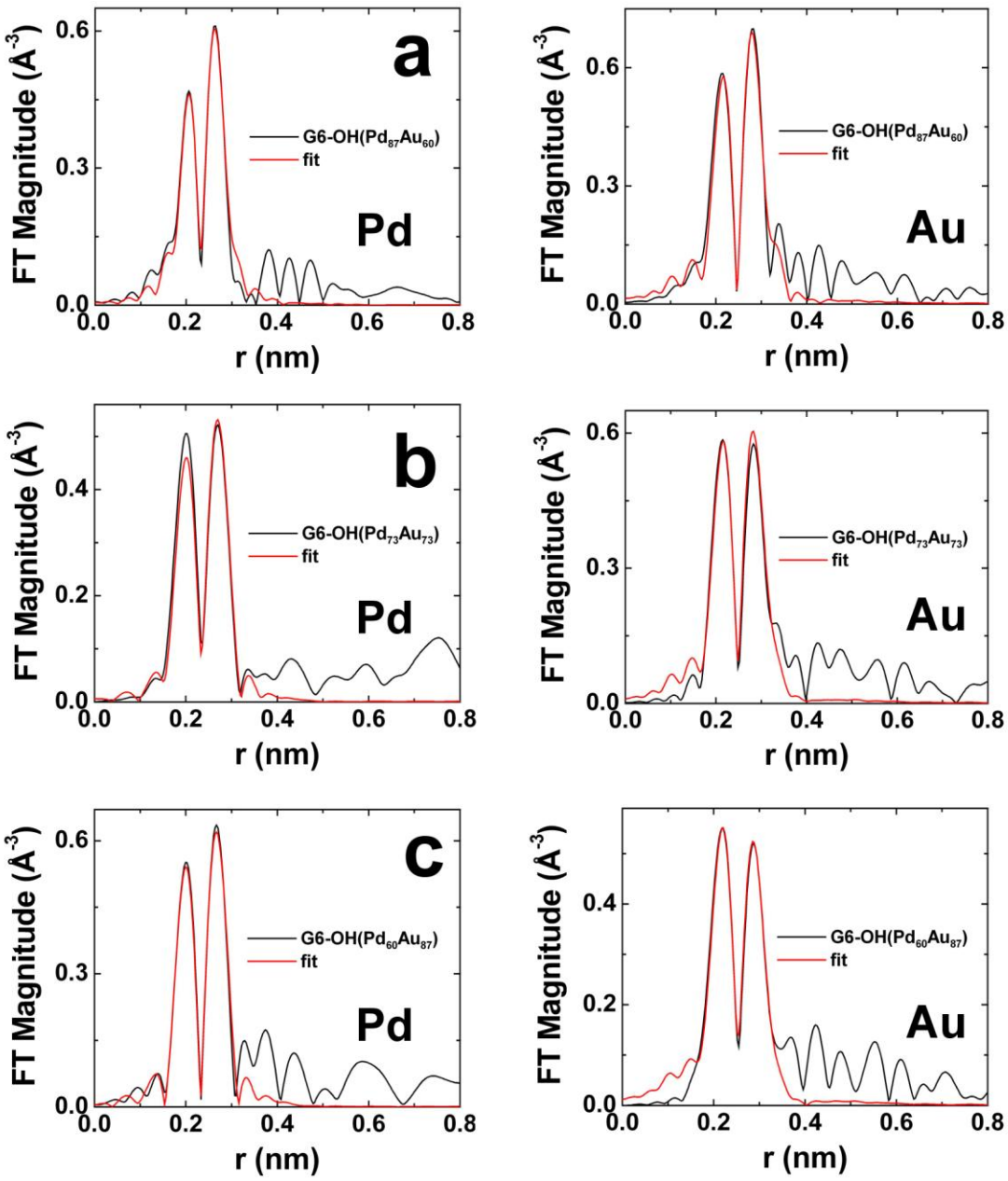

Figure 4.8. EXAFS data and fitting analysis for the Pd (left) and Au (right) absorption edge of (a) G6-OH(Pd87Au60), (b) G6-OH(Pd73Au73), and (c) G6-OH(Pd60Au87) DENs. The experimentally obtained data is plotted in black, while the fit of the data is plotted in red.

to the shortest (at high Pd concentrations), extrapolating to 2.85 Å at x_{Pd} = 0 and 2.75 Å at x_{Pd} = 1, which agree well with the first nearest neighbor distances in bulk Au (2.87 Å) and Pd (2.75 Å).[68,69] In summary, the EXAFS analysis indicates that the dendrimer-templating method used here results in PdAu DENs having a quasirandom alloy structure. Note that no coordination of the dendrimer through N (or O) ligands was observed, indicating that a significant fraction of the surface metal atoms are freely exposed.

EXAFS Characterization of MPCs

EXAFS analyses of the dodecanethiol-capped PdAu MPCs corresponding to the DENs represented in Figure 4.7 are provided in Figure 4.9. The fitting analysis for other concentrations is presented in Figure 4.10. The results indicate a structural rearrangement of the metallic architecture in response to the extraction process. Similar to the DEN parents, the number of Pd–Pd coordinations increases with increasing numbers of Pd atoms per MPC (Figure 4.9e); however, at the lowest concentration of Pd atoms, no Pd–Pd coordinations are observed. The Au–Au CN was found to be ~7.5 for all the MPCs except for the most

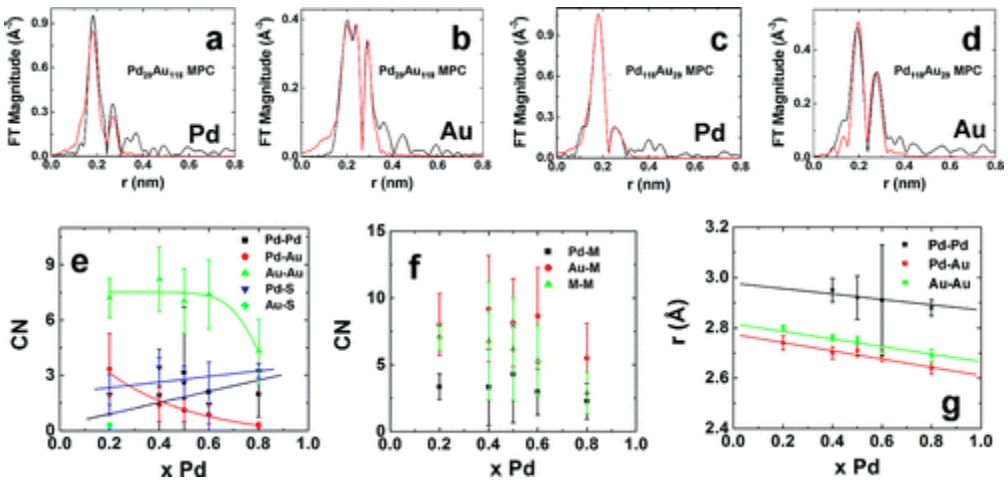

Figure 4.9. EXAFS data and the corresponding fitting analyses for the Pd K-edge and Au L_3-edge EXAFS for (a, b) $Pd_{29}Au_{118}$ and (c, d) $Pd_{118}Au_{29}$ MPCs. In parts a–d, the data are plotted in black and the simulated fits are plotted in red. (e) Experimentally obtained partial CNs for Pd–Pd, Pd–Au, and Au–Au MPCs. (f) Pd–M, Au–M, and M–M CNs as a function of Pd composition. (g) Metal–metal bond lengths for the PdAu MPCs.

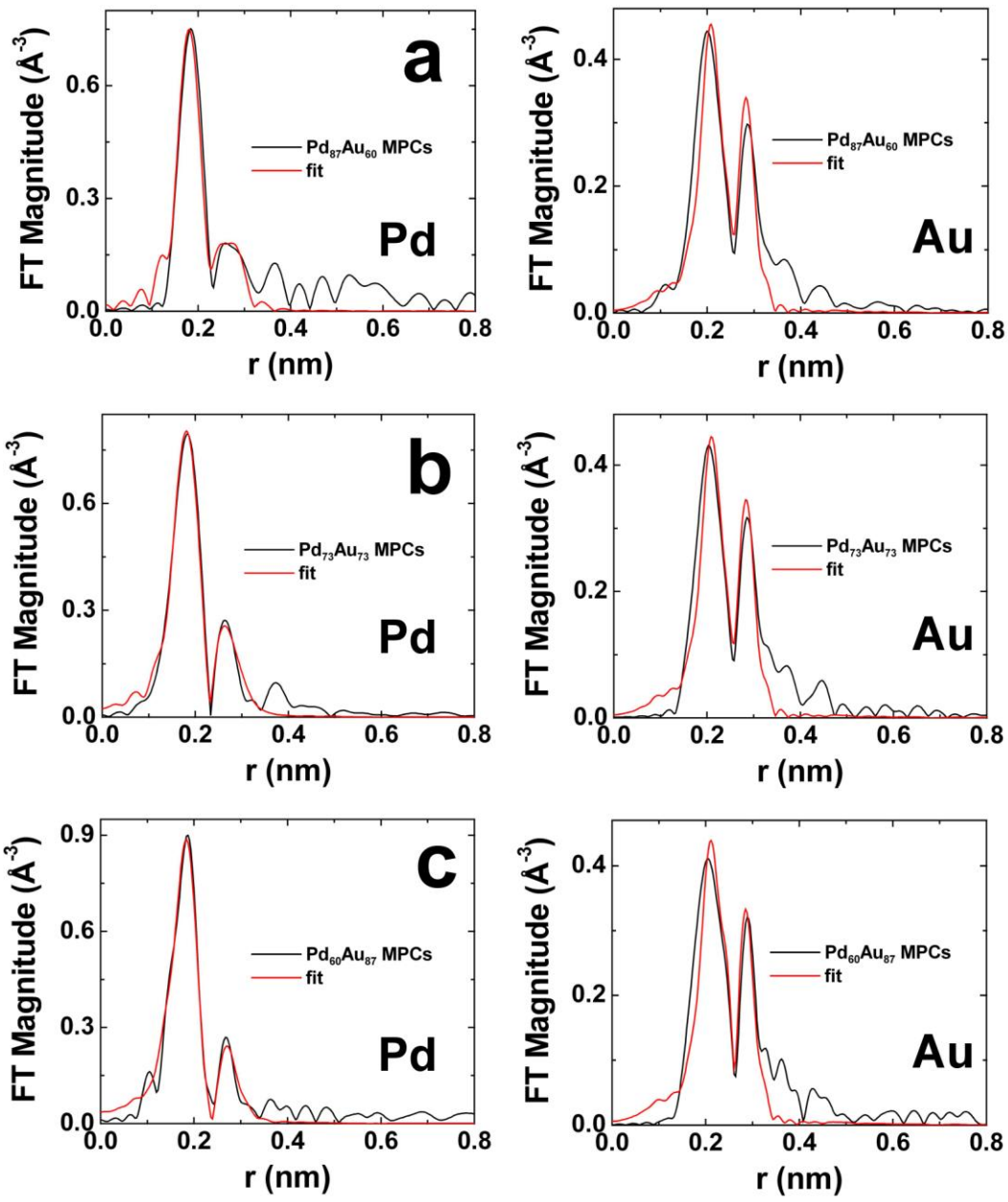

Figure 4.10. EXAFS data and fitting analysis for the Pd (left) and Au (right) absorption edge of (a) $Pd_{87}Au_{60}$, (b) $Pd_{73}Au_{73}$, and (c) $Pd_{60}Au_{87}$ MPCs. The experimentally obtained data is plotted in black, while the fit of the data is plotted in red.

Pd-rich nanoparticle ($Pd_{118}Au_{29}$, x_{Pd} = 0.8), which exhibited a Au–Au CN of 4.30 ± 1.8. For the Pd–Au coordinations, a nonlinear decrease was observed for the particles as the concentration of Pd increased. These EXAFS results are markedly different from those obtained for the DENs, which indicates a change in the structure of the nanoparticles after extraction. The CNs for the dodecanethiol ligands present on the surface of the MPCs provides additional clues as to the structure of these materials. As shown in Figure 4.9e, S interactions were observed only for Pd except for MPCs having the highest ratio of Au ($Pd_{29}Au_{118}$, x_{Pd} = 0.2). The Pd–S CN was found to be ~3 for all values of x_{Pd}, which is larger than expected for nanoparticles of this size.[70] If we assume that the surface concentration of alkylthiols on Pd nanoparticles is the same as has been found on Au MPCs, then a Pd–S CN of ~0.5 is anticipated.[58,70,71] Additionally, the total metal–metal CN (M–M, Figure 4.9f) ranges from approximately 3 (x_{Pd} = 0.8) to 7 (x_{Pd} = 0.2), which is smaller than the value of 8.98 predicted for cuboctahedral particles of this size.[72] These two observations are consistent with a model that invokes two different Pd–S interaction motifs. Specifically, one model involves dodecanethiol bound to surface Pd atoms of

the MPCs, and the other involves dodecanethiol coordinated to single Pd ions (or very small clusters of Pd atoms or ions). Indeed, such Pd–S complexes have previously been observed for Pd MPCs[68,73] resulting in larger than expected Pd–S CNs and smaller than expected Pd–Pd CNs.[68]

Correlation of the Proposed Model and the Experimental Results

The MPC EXAFS results are consistent with oxidatively driven de-alloying of the PdAu alloy DENs as shown in Scheme 4.1. In this model, some or all of the Pd atoms within the DENs oxidize in the presence of air. This results in formation of more noble Au-only (or mostly) nanoparticles and reconstitution of the Pd^{2+}/dendrimer complex (part D in Scheme 4.1). During extraction, however, a large excess of reducing agent is added, which results in deposition of Pd atoms onto the surface of the Au core (part E in Scheme 4.1). This is followed by extraction as an MPC (part F in Scheme 4.1).

The proposed model is supported by the following findings. First, Pd–M CNs are much smaller (typically by a factor of 2) than Au–M CNs (Figure 4.9f), indicating that

segregation of Pd on the surface of the MPCs is more pronounced than for the PdAu DENs (Figure 4.7f). This Pd-rich structure is also consistent with our finding that Au–S interactions are observed only at the lowest value of x_{Pd}, whereas Pd–S interactions are observed at all values of x_{Pd}. Note, however, that the latter observation is complicated by the likely presence of Pd–thiol complexes. Eventually, as the number of Au atoms per particle increases (x_{Pd} = 0.2), a sufficient number of them are present on the surface that Au–S interactions are observed.

Figure 4.9g is of particular interest, because it independently confirms surface segregation of Pd atoms. In other examples of binary alloys consisting of two species A and B with different nearest neighbor distances *a* and *b*, respectively, it has been found by EXAFS that the bond lengths at all concentrations are located between *a* and *b*.[74-77] For the PdAu DENs, we found this rule to hold (Figure 4.7g), but it does not hold for the PdAu MPCs. Specifically, the data in Figure 4.9g show that the Pd–Pd bond is distinctly longer than either the Au–Au or Pd–Au bonds at all Pd:Au ratios as well as in bulk Au (2.87 Å). This anomalous behavior is likely the result of particle

surface relaxation, wherein Pd atoms shift away from the normal fcc sites, resulting in longer Pd–Pd bonds. Such displacements must be accompanied by enhanced disorder, which is represented by σ^2. Indeed, σ^2 values for the Pd–Pd bonds are much larger for the MPCs compared to the DENs (Table 4.1). Figure 4.11 provides additional support for the model shown in Scheme 4.1. Specifically, Figure 4.11a demonstrates the effects of exposure of G6-OH($Pd_{118}Au_{29}$) DENs to air after reduction. Prior to reduction, the LMCT band at 221 nm for the Pd^{2+}/amine interaction is evident. After $AuCl_4^-$ addition and BH_4^- reduction, the LMCT band disappears and a spectrum reminiscent to that shown in Figure 4.1b is obtained demonstrating nearly complete Pd-ion reduction. After exposure of the reduced DEN sample to air for ~2 h, a peak at 221 nm is observed that is consistent with Pd atom oxidation and reconstitution to form the Pd^{2+}/dendrimer composite with the reduced Au nanoparticles remaining after oxidation. After introduction of additional BH_4^- for the extraction process, the peak at 221 nm decreases in intensity, indicating reduction of Pd^{2+}, which can deposit along the surface of the nascent Au DENs. The LMCT band does not completely disappear after the secondary reduction, suggesting that not all of the oxidized Pd^{2+} ions

Table 4.1. Comparison of the σ^2 values for the PdPd, PdAu, and AuAu bonds for DENs and MPCs. Over the compositional range studied, the values are larger for the MPCs compared to the DENs, indicating relaxation of the Pd-Pd bonds in MPCs.

Species		PdPd ($Å^2$)	PdAu ($Å^2$)	AuAu ($Å^2$)
$Pd_{29}Au_{118}$	DEN	0.000 ± 0.016	0.005 ± 0.002	0.000 ± 0.005
	MPC	n/a	0.000 ± 0.004	0.004 ± 0.005
$Pd_{60}Au_{87}$	DEN	0.002 ± 0.002	0.006 ± 0.003	0.014 ± 0.011
	MPC	0.011 ± 0.009	0.008 ± 0.004	0.012 ± 0.003
$Pd_{73}Au_{73}$	DEN	0.007 ± 0.003	0.006 ± 0.002	0.009 ± 0.006
	MPC	0.018 ± 0.017	0.008 ± 0.004	0.012 ± 0.003
$Pd_{87}Au_{60}$	DEN	0.006 ± 0.001	0.008 ± 0.002	0.012 ± 0.002
	MPC	0.013 ± 0.058	0.008 ± 0.004	0.014 ± 0.002
$Pd_{118}Au_{29}$	DEN	0.007 ± 0.001	0.011 ± 0.004	0.011 ± 0.002
	MPC	0.013 ± 0.007	0.009 ± 0.005	0.012 ± 0.001

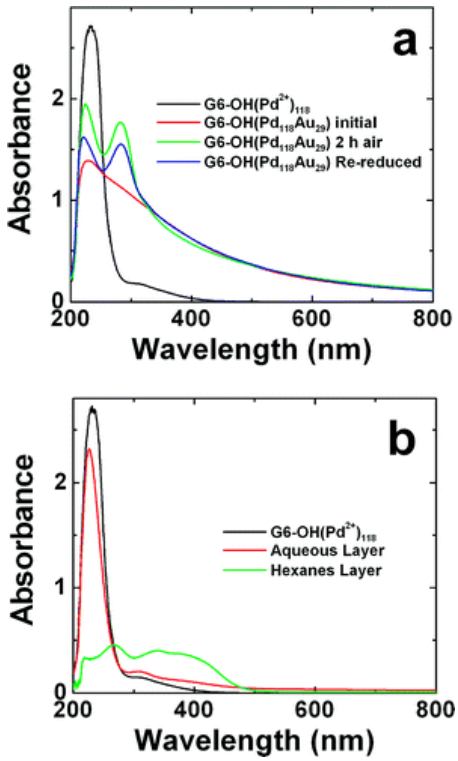

Figure 4.11. UV–vis spectra demonstrating air oxidation of Pd DENs and dodecanethiol-induced extraction of Pd ions from the dendrimer interior. (a) Spectra of the G6-$OH(Pd^{2+})_{118}$ complex prior to reduction, after reduction with BH_4^-, after exposure to air for 2 h, and after a second reduction. (b) Spectra of G6-$OH(Pd^{2+})_{118}$ before and after extraction with dodecanethiol but in the absence of a reducing agent.

have been reduced immediately prior to extraction. Note that the peak at 285 nm, which we correlated to the dendrimer earlier, is present after exposure of the DEN solution to air for 2.00 h. This might suggest that this peak arises from oxidation of the dendrimer.

Because the extraction process is completed with PdAu DEN species that are not fully reduced, it is possible that the unreduced Pd^{2+} can be extracted as well. This effect would give rise to the experimentally observed decrease in the M–M CN in the extracted MPCs (Figure 4.9f). To confirm this hypothesis, we carried out a control experiment in which the steps required for extraction were carried out on the G6-OH$(Pd^{2+})_{118}$ complex prior to reduction (Figure 4.11b). Before addition of dodecanethiol the typical LMCT band at 221 nm was observed. After addition of a solution of hexanes containing dodecanethiol, a slight decrease in the absorbance at 221 nm is observed in the aqueous phase and a slight increase is observed in the organic phase. These results suggest that Pd^{2+}/thiol complexes extract into the organic phase, and this finding is consistent with both the large Pd–S CN and the small M–M CN obtained for the PdAu MPCs.

4.5 Summary and Conclusions

We prepared bimetallic PdAu DENs by co-complexing metal ions with dendrimers and then reducing. The resulting materials are nearly monodisperse in size. EXAFS data indicate that the PdAu DENs are quasi-random alloys regardless of their relative elemental composition. Dodecanethiol extraction of the materials into hexanes results in the formation of Au-core/Pd-shell MPCs. In addition, we postulate a model in which Pd/thiol complexes are also extracted from the dendrimers to account for the both the large Pd–S CN and the small M–M CN.

The structural rearrangement that occurs upon extraction (Scheme 4.1) is likely due to Pd oxidation and re-reduction during the extraction. This change in structure is unusual and likely the result of the oxidized Pd atoms being sequestered within the dendrimer near the Au monometallic core. We also considered a model in which the structural rearrangement was driven by the thiol ligand (rather than metal oxidation). However, because the thiol binding strength to Au is stronger than to Pd, we anticipated that a ligand-driven structural change would

result in a Pd-core/Au-shell configuration.[78] Accordingly, we do not consider this mechanism to be likely.

References

1. Scott, R. W. J.; Wilson, O. M.; Crooks, R. M. *J. Phys. Chem. B* **2005** 109 692-704

2. Chandler, B. D.; Gilbertson, J. D. *Top. Organomet. Chem.* **2006** 20 97-120

3. Crooks, R. M.; Zhao, M.; Sun, L.; Chechik, V.; Yeung, L. K. *Acc. Chem. Res.* **2001** 34 181-190

4. Scott, R. W. J.; Sivadinarayana, C.; Wilson, O. M.; Yan, Z.; Goodman, D. W.; Crooks, R. M. *J. Am. Chem. Soc.* **2005** 127 1380-1381

5. Scott, R. W. J.; Wilson, O. M.; Oh, S.-K.; Kenik, E. A.; Crooks, R. M. *J. Am. Chem. Soc.* **2004** 126 15582-15591

6. Wilson, O. M.; Scott, R. W. J.; Garcia-Martinez, J. C.; Crooks, R. M. *J. Am. Chem. Soc.* **2005** 127 1015-1024

7. Wilson, O. M.; Scott, R. W. J.; Garcia-Martinez, J. C.; Crooks, R. M. *Chem. Mater.* **2004** 16 4202-4202

8. Garcia-Martinez, J. C.; Scott, R. W. J.; Crooks, R. M. *J. Am. Chem. Soc.* **2003** 125 11190-11191

9. Garcia-Martinez, J. C.; Crooks, R. M. *J. Am. Chem. Soc.* **2004** 126 16170-16178

10. Scott, R. W. J.; Datye, A. K.; Crooks, R. M. *J. Am. Chem. Soc.* **2003** 125 3708-3709

11. Toshima, N.; Yonezawa, T. *New J. Chem.* 1998 1179-1201

12. Toshima, N.; Harada, M.; Yamazaki, Y.; Asakura, K. *J. Phys Chem.* **1992** 96 9927-9933

13. Mizukoshi, Y.; Fujimoto, T.; Nagata, Y.; Oshima, R.; Maeda, Y. *J. Phys. Chem. B* **2000** 104 6028-6032

14. Slocik, J. M.; Naik, R. R. *Adv. Mater.* **2006** 18 1988-1992

15. Pârvulescu, V. I.; Pârvulescu, V.; Endruschat, U.; Filoti, G.; Wagner, F. E., Kubel, C.; Richards, R. *Chem. Eur. J.* **2006** 12 2343-2357

16. Chen, M.; Kumar, D.; Yi, C.-W.; Goodman, D. W. *Science* **2005** 310 291-293

17. Ferrer, D.; Torres-Castro, A.; Gao, X.; Sepúlveda-Guzmán, S.; Ortiz-Méndez, U.; José-Yacamán, M. *Nano Lett.* **2007** 7 1701-1705

18. Lee, A. F.; Baddeley, C. J.; Hardacre, C.; Ormerod, R. M.; Lambert, R. M.; Schmid, G.; West, H. *J. Phys. Chem.* **1995** 99 6096-6102

19. Luo, K.; Wei, T.; Yi, C.-W.; Axnanda, S.; Goodman, D. W. *J. Phys. Chem. B* **2005** 109 23517-23522

20. Mejfia-Rosales, S. J.; Fernandez-Navarro, C.; Perez-Tijerina, E.; Blom, D. A.; Allard, L. F.; Yacaman, M.-J. *J. Phys. Chem. C* **2007** 111 1256-1260

21. Shiraishi, Y.; Ikenaga, D.; Toshima, N. Aust. *J. Chem.* **2003** 56 1025-1029

22. Solsona, B. E.; Edwards, J. K.; Landon, P.; Carley, A. F.; Herzing, A.; Kiely, C. J.; Hutchings, G. J. *Chem. Mater.* **2006** 18 2689-2695

23. Villa, A.; Champione, C.; Prati, L. *Catal. Lett.* **2007** 115 113-136

24. Wang, D; Villa, A.; Porta, F.; Su, D.; Prati, L. *Chem. Commun.* **2006** 2006 1956-1958

25. Wei, T.; Wang, J.; Goodman, D. W. *J. Phys. Chem. C* **2007** 111 8781-8788

26. Wu, M.-L.; Chen, D.-H.; Huang, T.-C. *Langmuir* **2001** 17 3877-3883

27. Mizukoshi, Y.; Okitsu, K.; Maeda, Y.; Yamamoto, T. A.; Oshima, R.; Nagata, Y. *J. Phys. Chem. B* **1997** 101 7033-7037

28. Ge, Z.; Cahill, D. G.; Braun, P. V. *J. Phys Chem. B* **2004** 108 18870-18875

29. Harpeness, R.; Gedanken, A. *Langmuir* 2004 20 3431-3434

30. Nath, S.; Praharaj, S.; Panigrahi, S.; Ghosh, S. K.; Kundu, S.; Basu, S.; Pal, T. *Langmuir* **2005** 21 10405-10408

31. Hu, J.-W.; Li, J.-F.; Ren, B.; Wu, D.-Y.; Sun, S.-G.; Tian, Z.-Q. *J. Phys. Chem. C* **2007** 111 1105-1112

32. Henglein, A. *J. Phys. Chem. B* **2000** 104 6683-6685

33. Boennemann, H.; Endruschat, U.; Tesche, B.; Ruffinska, A.; Lehmann, C. W.; Wagner, F. E.; Filoti, G.; Parvulescu, V.; Parvulescu, V. I. *Eur. J. Inorg. Chem.* **2000** 2000 819-822

34. Crespilho, F. N.; Zucolotto, V.; Brett, C. M. A.; Oliveira, O. N.; Nart, F. C. *J. Phys. Chem. B* **2006** 110 17478-17483

35. Kim, Y.-G.; Oh, S.-K.; Crooks, R. M. *Chem. Mater.* **2004** 16 167-172

36. Knecht, M. R.; Crooks, R. M. *New J. Chem.* **2007** 31 1349-1353

37. Knecht, M. R.; Garcia-Martinez, J. C.; Crooks, R. M. *Chem. Mater.* **2006** 18 5039-5044

38. Lang, H.; May, R. A.; Iversen, B. L.; Chandler, B. D. *J. Am. Chem. Soc.* **2003** 125 14832-14836

39. Mark, S. S.; Bergkvist, M.; Yang, X.; Angert, E. R.; Batt, C. A. *Biomacromolecules* **2006** 7 1884-1897

40. Niu, Y.; Yeung, L. K.; Crooks, R. M. *J. Am. Chem. Soc.* **2001** 123 6840-6846

41. Scott, R. W. J.; Ye, H.; Henriquez, R. R.; Crooks, R. M. *Chem. Mater.* **2003** 15 3873-3878

42. Wilson, O. M.; Knecht, M. R.; Garcia-Martinez, J. C.; Crooks, R. M. *J. Am. Chem. Soc.* **2006** 128 4510-4511

43. Ye, H.; Scott, R. W. J.; Crooks, R. M. *Langmuir* **2004** 20 2915-2920

44. Zhao, M.; Sun, L.; Crooks, R. M. *J. Am. Chem. Soc.* **1998** 120 4877-4878

45. Narayanan, R.; El-Sayed, M. A. *J. Phys. Chem. B* **2004** 108 8572-8580

46. Vijayaraghavan, G.; Stevenson, K. J. *Langmuir* **2007** 23 5279-5282

47. Hoover, N. N.; Auten, B. J.; Chandler, B. D. *J. Phys. Chem. B* **2006** 110 8606-8612

48. Lang, H.; Maldonado, S.; Stevenson, K. J.; Chandler, B. D. *J. Am. Chem. Soc.* **2004** 126 12949-12956

49. Ye, H.; Crooks, R. M. *J. Am. Chem. Soc.* **2007** 129 3627-3633

50. Lemon, B. I.; Crooks, R. M. *J. Am. Chem. Soc.* **2007** 129 3627-3633

51. Zhao, M.; Crooks, R. M. *Angew. Chem., Int. Ed.* **1999** 38 364-366

52. Garcia-Martinez, J. C.; Lezutekong, R.; Crooks, R. M. *J. Am. Chem. Soc.* **2005** 127 5097-5103

53. Ye, H.; Crooks, R. M. *J. Am. Chem. Soc.* **2005** 127 4930-4934

54. Scott, R. W. J.; Wilson, O. M.; Crooks, R. M. *Chem. Mater.* **2004** 16 5682-5688

55. Pellechia, P. J.; Gao, J.; Gu, Y.; Ploehn, H. J.; Murphy, C. J. *Inorg. Chem.* **2004** 43 1421-1428

56. Ozturk, O.; Black, T. J.; Perrine, K.; Pizzolato, K.; Williams, C. T.; Parson, F. W.; Ratliff, J. S.; Gao, J.; Murphy, C. J.; Xie, H.; Ploehn, H. J.; Chen, D. A. *Langmuir* **2005** 21 3998-4006

57. Alexeev, O. S.; Siani, A.; Lafaye, G.; Williams, C. T.; Ploehn, H. J.; Amiridis, M. D. *J. Phys. Chem. B* **2006** 110 24903-24914

58. Templeton, A. C.; Wuelfing, W. P.; Murray, R. W. *Acc. Chem. Res*. **2000** 33 27-36

59. Newville, M. *J. Synchrotron Radiat.* 2001 8 322-324

60. Slocik, J. M.; Naik, R.; Stone, M. O.; Wright, D. W. *J. Mater. Chem.* **2005** 15 749-753

61. Garcia, M. E.; Baker, L. A.; Crooks, R. M. *Anal. Chem.* **1999** 71 256-258

62. Creighton, J. A.; Eadon, D. G. *J. Chem. Soc., Faraday Trans.* **1991** 87 3881-3891

63. Lee, W. I.; Bae, Y.; Bard, A. J. *J. Am. Chem. Soc.* **2004** 126 8358-8359

64. Kim, Y.-G.; Garcia-Martinez, J. C.; Crooks, R. M. *Langmuir* **2005** 21 5485-5491

65. Wang, D.; Imae, T.; Miki, M. *J. Colloid Interface Sci.* **2007** 306 222-227

66. Nashner, M. S.; Frenkel, A. I.; Adler, D. L.; Shapley, J. R.; Nuzzo, R. G. *J. Am. Chem. Soc.* **1997** 119 7760-7771

67. Frenkel, A. I. *Z. Kristallogr.* **2007**, 222 605-611

68. Sun, Y.; Frenkel, A. I.; Isseroff, R.; Shonbrun, C.; Forman, M.; Shin, K.; Koga, T.; White, H.; Zhang, L.; Zhu, Y.; Rafallovich, M. H.; Sokolov, J. C. *Langmuir* **2006** 22 807-816

69. Frenkel, A. I.; Nemzer, S.; Pister, I.; Soussan, L.; Harris, T.; Sun, Y.; Rafallovich, M. H. *J. Chem. Phys.* **2005** 123 184701

70. Petkov, V.; Bedford, N.; Knecht, M. R.; Weir, M. G.; Crooks, R. M.; Tang, W.; Henkelman, G.; Frenkel, A. I. *J. Phys. Chem. C* **2008** 112 8907-8911

71. Sellers, H.; Ulman, A.; Schnidman, Y.; Eilers, J. E. *J. Am. Chem. Soc.* **1993** 115 9389-9401

72. Glasner, D.; Frenkel, A. *XAFS13 Conf. Proc.* **2007** 882 746-748

73. Zamborini, F. P.; Gross, S. M.; Murray, R. W. *Langmuir* **2001** 17 481-488

74. Frenkel, A. I.; Stern, E. A.; Voronel, A.; Qian, M.; Newville, M. *Phys. Rev. Lett.* **1993** 71 3485-3488

75. Frenkel, A. I.; Stern, E. A.; Voronel, A.; Heald, S. *Solid State Commun.* **1996** 99 67-71

76. Boyce, J. B.; Mikkelsen, J. C. *Phys. Rev. B* **1985** 31 6903-6905

77. Frenkel, A. I.; Machavariani, V. S.; Rubshtein, A.; Rosenberg, Y.; Voronel, A.; Stern, E. A. *Phys. Rev. B* **2000** 62 9364-9371

78. CRC Handbook of Chemistry and Physics, 87th ed.; Lide, D. R., Ed.; Taylor and Francis: New York, **2006**

Chapter 5: Structural Analysis of PdAu Dendrimer-Encapsulated Bimetallic Nanoparticles

5.1 Synopsis

PdAu dendrimer-encapsulated nanoparticles (DENs) were prepared via sequential reduction of the component metals. When Au is reduced onto 55-atom, preformed Pd DEN cores, analysis by UV-vis spectroscopy, electron microscopy, and extended X-ray absorption fine structure (EXAFS) spectroscopy leads to a model consistent with inversion of the two metals. That is, Au migrates into the core and Pd resides on the surface. However, when Pd is reduced onto a 55-atom Au core, the expected Au core/Pd shell structure results. In this latter case, the EXAFS analysis suggests partial oxidation of the relatively thick Pd shell. When the DENs are extracted from their protective dendrimer stabilizers by alkylthiols, the resulting monolayer-protected clusters retain their original Au core-Pd shell structures. The structural analysis is consistent with a study of nanoparticle-catalyzed conversion of resazurin to

resorufin. The key conclusion from this work is that correlation of structure to catalytic function for very small, bimetallic nanoparticles requires detailed information about atomic configuration.

5.2 Introduction

Here we report the synthesis and characterization of bimetallic PdAu dendrimer-encapsulated nanoparticles (DENs) prepared via sequential reduction of the component metals in hydroxyl-terminated poly(amidoamine) (PAMAM) dendrimers (Scheme 5.1).[1] We have previously reported that this approach can be used to prepare nanoparticles comprised of a core of the first metal covered with a shell of the second metal.[2,3] The key result to emerge from the present study is that regardless of whether Pd or Au is reduced first, these DENs adopt a Au core-Pd shell (Au@Pd) structure. Primary evidence for this contention comes from detailed measurements made by extended X-ray absorption fine structure (EXAFS) spectroscopy. Additionally, the Au-

Scheme 5.1

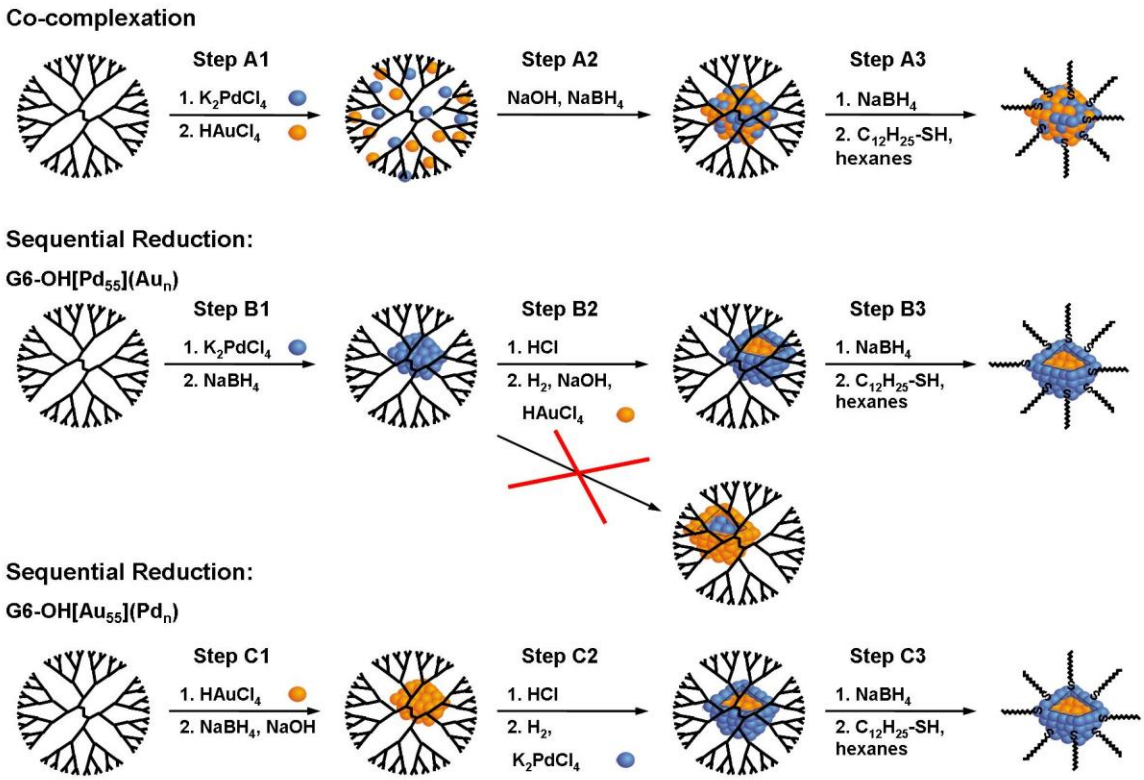
Co-complexation
Step A1
1. K_2PdCl_4
2. $HAuCl_4$
Step A2
$NaOH, NaBH_4$
Step A3
1. $NaBH_4$
2. $C_{12}H_{25}$-SH, hexanes
Sequential Reduction:
G6-OH[Pd_{55}](Au_n)
Step B1
1. K_2PdCl_4
2. $NaBH_4$
Step B2
1. HCl
2. H_2, NaOH,
$HAuCl_4$
Step B3
1. $NaBH_4$
2. $C_{12}H_{25}$-SH, hexanes
Sequential Reduction:
G6-OH[Au_{55}](Pd_n)
Step C1
1. $HAuCl_4$
2. $NaBH_4$, NaOH
Step C2
1. HCl
2. H_2,
K_2PdCl_4
Step C3
1. $NaBH_4$
2. $C_{12}H_{25}$-SH, hexanes

catalyzed conversion of resazurin to resorufin is used to probe the surface composition of the DENs, and the results are consistent with the EXAFS data.[4] Finally, we also show that Au@Pd DENs can be extracted from within their host dendrimers with their core-shell structures intact by using appropriate α-alkylthiol ligands.

DENs are usually synthesized in a two-step process. First, metal ions are extracted from solution into the dendrimer interior via complexation with internal tertiary amines. Second, the metal ions are reduced with BH_4^-, and the resultant atoms subsequently coalesce to form zerovalent nanoparticles within the dendrimer templates. Monometallic Au, Pt, Pd, Cu, Ni, Ru, Rh, Ir, and Fe, as well as bimetallic AuAg, PdAu, PdPt, PtCu, PtAu, and CuPd DENs, have been synthesized using this basic procedure.[1-3,5-22] Once formed, DENs are retained within and stabilized by the dendrimer framework.[1]

We have previously reported the synthesis of PdAu bimetallic nanoparticles using two different methods: co-complexation of both precursor metal ions followed by simultaneous reduction,[2,7,23] and sequential complexation and reduction of each of the two metals (Scheme 5.1).[2] The

first report of PdAu DENs described the products of both the co-complexation and sequential methods using both partially quaternized, amine-terminated dendrimers and hydroxyl-terminated dendrimers.[2] UV-vis spectroscopy and selective catalysis experiments indirectly confirmed structural differences between DENs prepared by co-complexation and sequential reduction. We also suggested, on the basis of fairly weak evidence, that there might be differences in the structures of core-shell PdAu DENs depending on which metal was used as the seed (core). In the present chapter, using more sophisticated analysis tools, we recognize that regardless of whether Au or Pd is used as the initial seed, the product of the sequential reduction is a Au@Pd DEN.

In addition to the detailed study described in the previous paragraph, we also reported that PdAu alloy DENs prepared within primary amine-terminated PAMAM dendrimers via the co-complexation route could be immobilized on titania substrates.[23] However, this report focused on the catalytic oxidation of CO, and little structural analysis was presented. Finally, we very recently reported a detailed EXAFS analysis of PdAu bimetallic DENS synthesized

via co-complexation within sixth-generation, hydroxyl-terminated (G6-OH) PAMAM dendrimers.[7] Consistent with our preliminary report,[2] these results showed that PdAu DENs prepared by co-complexation form alloys. However, we described these DENs as quasirandom alloys, because they were somewhat enriched with Pd on their surface and with Au within their interior. We also showed that these PdAu alloys could be converted into Au@Pd monolayer-protected clusters (MPCs)[24,25] via intradendrimer de-alloying and subsequent reduction.

Chandler and coworkers have prepared PtCu,[6] PtAu,[8] and NiAu[26] nanoparticles via dendrimer templating. The PtCu DENs were synthesized by co-complexation while preparation of the PtAu DENs involved galvanic exchange. The NiAu nanoparticles were stabilized by multiple dendrimers rather than being encapsulated within single dendrimers.[26,27] The surface composition of supported PtCu DENs was inferred from catalytic measurements of toluene hydrogenation and CO oxidation. Specifically, Pt dominated the catalytic properties in the presence of CO, while Cu had a strong negative influence on the catalytic rate during

hydrogenation. The data were interpreted in terms of structural rearrangements driven by CO.

There have been numerous reports from other groups concerning the synthesis of PdAu bimetallic nanoparticles prepared by means other than dendrimer templating.[28,29] However, here we focus only on unsupported PdAu particles having diameters of < ~5 nm, as they are most closely related to the DENs discussed in this chapter. Different synthetic methods are capable of producing nanoparticles with alloy,[30,31] core-shell[29,32-34] and other more complex structures.[35,36] The structure of PdAu alloys range from truly random[30] to partially segregated, quasi-random alloys.[7,31] In this small size range, most core-shell particles formed are Au@Pd,[29] but larger particles may form the opposite structure.[34] Jose-Yacaman and coworkers have used aberration-corrected TEM to demonstrate a three-layer structure that varies as a function of the diameter of the particle and the ratio of the two metals.[35,36] They have also used inert-gas condensation in a sputter reactor to synthesize alloyed PdAu bimetallic nanoparticles.[30] Classical molecular dynamics simulations have shown that the Pd@Au structure is the most stable form

thermodynamically,[37] but these calculations do not include ligand effects or other conditions present during a real synthesis.

X-ray absorption spectroscopy (XAS) is a powerful tool for determining the structure of bimetallic nanoparticles.[38-40] For example, a case that is particularly relevant to that discussed here was carried out by Toshima and coworkers. They investigated polymer-protected PdAu clusters prepared by both simultaneous[41] and sequential[42] reduction. A Au@Pd structure was determined for the simultaneous reduction case. The sequential reduction process yielded two different results, depending on the order of reduction of the metals. When Pd was reduced first, bimetallic cluster-in-cluster structures were observed.[42] When Au was reduced first, a mixture of Pd and Au monometallic nanoparticles was formed. XAS studies have been carried out on other, larger PdAu nanoparticles in solution[43] and on supported PdAu clusters.[44-46]

Here we used UV-vis spectroscopy, TEM, EXAFS, and a Au-specific catalytic reaction to elucidate the structure of bimetallic PdAu DENs prepared within G6-OH dendrimers via the sequential reduction method illustrated in Scheme

5.1. Specifically, Au and Pd seed DENs were prepared, and then the second metal was catalytically reduced onto the seeds. UV-vis spectroscopy confirms that the precursor metal ions are complexed and then reduced. TEM size-distribution analysis shows that the sizes of these particles are consistent with expectations based on their composition and the average number of atoms per particle. EXAFS reveals that a Au@Pd structure forms in DENs prepared by sequential reduction regardless of the order that the component metals are introduced. When extracted from the dendrimer interior with dodecanethiol, the particles retain their Au@Pd structure but with an unanticipated degree of Pd-S bonding. A comprehensive study of the catalytic conversion of resazurin to resorufin indicates that monometallic Au DENs are highly active. However, bimetallic DENs having Pd-only shells, or even shells composed of both Pd and Au, are not active. This suggests that particular arrangements of Au atoms on the nanoparticle surface are required for catalytic activity.

5.3 Experimental Section

Chemicals. G6-OH PAMAM dendrimers were purchased from Dendritech, Inc. (Midland, MI) as methanol solutions. Prior to use, the dendrimer stock solution was dried under vacuum and then redissolved in sufficient deionized water to make a 100 μM solution. All other chemicals were used as received unless otherwise noted in the text. Resazurin, K_2PdCl_4, $NaBH_4$, $HAuCl_4 \cdot 3H_2O$, and dodecanethiol were purchased from Sigma-Aldrich (Milwaukee, WI), and NaOH, HCl, and hexanes were purchased from Fisher Scientific (Pittsburgh, PA). Absolute ethanol was purchased from Aaper Chemical Co. (Shelbyville, KY). Aqueous solutions were prepared using 18 MΩ·cm Milli-Q water (Millipore, Bedford, MA).

Characterization. UV-vis absorbance spectra were obtained using a Hewlett-Packard HP8453 spectrometer and quartz cuvettes having an optical path length of 0.200 cm. Depending on the sample, a spectrum of either 2.00 μM G6-OH in water or neat hexanes (no dendrimer) was used for background subtraction. TEM micrographs were obtained using a JEOL-2010F TEM operating at 200 kV. Samples were prepared by dropwise addition of an appropriate solution onto a 20 nm-thick, carbon-coated, 400 mesh Cu grid (EM

Sciences, Gibbstown, NJ) followed by solvent evaporation in air.

EXAFS experiments were conducted at beamline X18B of the National Synchrotron Light Source at the Brookhaven National Laboratory. The DEN solutions were freeze-dried using a Labconco FreeZone 12L lyophilizer to simplify transporting them to the beamline. Subsequently, the powder was partially reconstituted in methanol or hexanes for dispersion onto adhesive tape, followed by drying in air. The tapes were folded multiple times to ensure homogeneity. The samples were measured in fluorescence mode, using an Ar-filled, five-grid Lytle detector, with the sample positioned at a 45° angle relative to the incident beam. X-ray absorption coefficients were measured from 150 eV below to 750 and 1250 eV above the Pd K and Au L_3-edges, respectively. The X-ray energy was calibrated prior to examination of each metallic edge by analysis of the corresponding bulk metal foil. EXAFS data were analyzed using the IFEFFIT software package.[47]

Synthesis of the monometallic seed DENs. The synthesis of both Pd and Au monometallic DENs has previously been described.[1,48,49] However, the EXAFS studies

required larger quantities of DENs, so the synthesis was scaled up in the present case. Briefly, 5.0 mL of a 100.0 μM G6-OH stock solution was diluted with enough water (~240 mL) to yield a final concentration of 2.00 μM. For G6-OH(Pd_{55}) DENs, 55 equiv of a freshly prepared 10.0 mM K_2PdCl_4 solution (2.75 mL) were added to the G6-OH solution. The solution was allowed to stir for a minimum of 15 min to ensure complete complexation between the tertiary amines of the dendrimer and Pd^{2+}. We denote all forms of ionic Pd as Pd^{2+} for convenience and all forms of ionic Au as Au^{3+}, even though various ligand exchange products of $PdCl_4^{2-}$ likely exist.[50,51] Next, a 10-fold molar excess of an aqueous 1.00 M $NaBH_4$ solution was added to the dendrimer/metal-ion precursor. Reduction was allowed to proceed for 15 min. The final volume of each solution was 250 mL.

For the G6-OH(Au_{55}) DENs, a similar procedure was followed. After dilution of the dendrimer stock, 55 equiv of a 10.0 mM $HAuCl_4$ solution (2.75 mL) were added to the G6-OH solution. This was followed almost immediately (< 1 min) by addition of a 10-fold molar excess of 1.00 M $NaBH_4$ in 0.30 M aqueous NaOH (0.27 mL). Quick addition of $NaBH_4$ and the presence of base are necessary to prevent reduction

of the Au salt to zerovalent metal by the hydroxyl functionalities of the dendrimer.[52]

Synthesis of the shell. Sequentially reduced DENs having a nominal 55-atom Pd core and either 92 or 254 Au atoms in the putative shell were prepared as follows. Ten min after formation of the monometallic Pd DEN core, 1.50 mL of 0.30 M HCl was added to the solution to quench unreacted reducing equivalents of BH_4^-. A few minutes later, H_2 gas was bubbled through the solution. After ~10 min, 2.25 mL of 0.30 M NaOH was added to neutralize the acid and ensure a basic pH (to slow reduction of the Au salt by hydroxyl groups of the dendrimer). Next, 92 or 254 equiv of 10.0 mM $HAuCl_4$ solution were added (4.60 and 12.7 mL, respectively). Bubbling of H_2 gas was continued for an additional 15 min.

Sequentially reduced DENs having a nominal 55-atom Au core and either 92 or 254 Pd atoms in the putative shell were prepared as follows. A 10% molar excess (with respect to the NaOH present in solution) of 0.30 M HCl (0.30 mL) was added to the monometallic Au core DENs. H_2 gas was then bubbled through the solution for a minimum of 10 min. While bubbling, either 92 or 254 equiv (4.60 and 12.7 mL,

respectively) of a fresh 10.0 mM K_2PdCl_4 solution was added. Bubbling of H_2 gas was continued for an additional 15 min.

Extraction of DENs. Extraction of the bimetallic PdAu DENs was carried out within 4 h of the initial reduction using a previously described method.[52-55] The solutions were exposed to air during this period and during the extraction process, resulting in partial oxidation of the zerovalent Pd within the DENs.[56] Briefly, 125 mL of an aqueous 2.00 μM DEN solution was placed into a separatory funnel. A 100-fold excess (with respect to the total metal concentration) of solid $NaBH_4$ was added. Next, 125 mL of a 29.4 mM dodecanethiol solution, prepared in hexanes, was layered atop the aqueous solution. The separatory funnel was shaken vertically and vigorously for 5 min. After settling, the organic phase was removed and collected. This process was repeated a total of six times: once for each of six 125 mL aliquots. At the end, all six extraction volumes (750 mL) were combined, and then concentrated on a rotary evaporator to a volume of ~5.0 mL. The resulting MPCs were then precipitated with absolute ethanol to separate them from excess dodecanethiol,[52,55] and the precipitate was collected by centrifugation. The

supernatant was decanted and the MPCs were redissolved in a small volume of hexanes. The concentrated solution was then evaporated to dryness under vacuum at 23 ± 2 °C.

Resazurin catalysis. 200.0 µL of each DEN sample (2.00 µM in dendrimer) was added to 10.0 mL of a 10.0 µM aqueous resazurin solution. Solutions were stirred for 5 min before UV-vis spectra were obtained. In some cases, an additional spectrum was obtained 24 h later to ensure completion of the reaction.

5.4 Results and Discussion

Nomenclature. We use Au_xPd_y to represent particles formed by co-complexation. For sequentially reduced DENs, the notation G6-OH[Au_x](Pd_y) is used when Au is reduced first and Pd second, but this does not imply a particular alloy or core-shell structure. Likewise, G6-OH[Pd_x](Au_y) represents the case when Pd is reduced first and Au second. The numbers *x* and *y* represent the stoichiometric relationship of the metal-ion-to-dendrimer ratios used in the synthesis (that is, the average number of Au and Pd atoms in the DENs). We have previously shown that the

average numbers of each element in bimetallic DENs closely corresponds to the actual stoichiometry of individual particles.[22] The notations Pd@Au and Au@Pd specifically imply core-shell structures with the first element corresponding to the core and the second to the shell metal.

Synthesis of PdAu DENs. Three methods for synthesizing bimetallic DENs are illustrated in Scheme 5.1. The co-complexation method (Steps A1 and A2) generally leads to alloy formation.[7] The two sequential reduction methods can lead to core-shell or alloy DENs. For sequential reduction, the seed DENs are synthesized (Steps B1 and C1) using the same methods we have previously used for monometallic DENs.[1,49,52] The second metal salt is added in the presence of a weaker reducing agent, H_2 gas in this case, so that the ions are catalytically reduced only on the existing DEN seed (Steps B2 and C2). The presence of H_2 ensures that a galvanic exchange mechanism (displacement of Pd by $AuCl_4^-$, for example) is not operative.[57]

Figure 5.1 provides UV-vis spectroscopic data for the sequential synthesis of PdAu DENs. The spectra in Figure 5.1a are consistent with 55-atom Pd DENs and subsequent

addition of sufficient Au to yield one and two shells (92 and 254 equiv of Au, respectively). In each case, a monotonically increasing absorbance toward lower wavelengths is observed. This is consistent with expectations from Mie theory for particles in this size range.[58-61] The spectra exhibit three features in the 200-300 nm range that merit comment. The absorbance of the dendrimer itself at ~200 nm is very strong, resulting in inconsistencies in background subtraction. There is a ligand-to-metal charge transfer (LMCT) peak at 220 nm corresponding to slight (< 10%) oxidation of the Pd_{55} DENs and subsequent recomplexation of the ions to the dendrimer.[49,56] The peak at ~280 nm may be related to a small amount of a catalytic decomposition product of the dendrimer,[49] but more likely arises from specific and reversible intradendrimer configurational changes driven by pH.[62] Whatever the origin of this band, it does not appear to significantly affect the synthesis or catalytic properties of DENs. The increase in absorbance for the two types of PdAu particles, compared to the Pd-only DENs, is

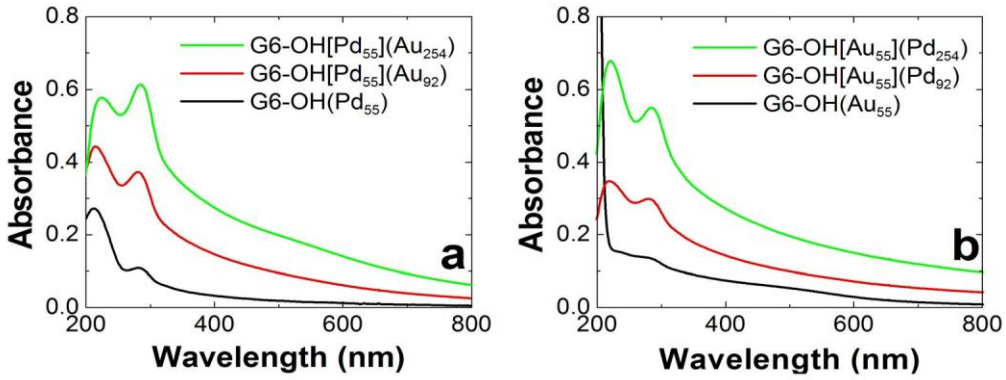

Figure 5.1. UV-vis spectra of (a) Pd monometallic DENs and PdAu DENs formed by sequential reduction of Au onto a Pd core; (b) Au monometallic DENs and PdAu DENs formed by sequential reduction of Pd onto a Au core. The concentration of the DENs solutions was 2.00 μM and the analysis was carried out in a 0.2 cm cuvette.

consistent with, but does not confirm, an increase in the size of the particles upon addition of Au.[58-61] A very slight plasmon band is centered at 522 nm for the G6-OH[Pd_{55}](Au_{254}) DENs.[58-60,63,64] The magnitude and position of this band is an indication that a very small fraction of these DENs have diameters in the 2-3 nm size range.[65-68]

The black spectrum in Figure 5.1b is consistent with 55-atom Au DENs,[3,48,52] and the other two spectra suggest further addition of Pd. The features of these spectra are similar to those in Figure 5.1a, except that the very small plasmon band, present at 505 nm for the Au_{55} seed DENs, is absent. Additionally, the Pd^{2+}-dendrimer LMCT band for the two bimetallics is slightly more pronounced. Finally, the similarity in the magnitudes of the absorbances of the spectra in Figures 5.1a and 5.1b suggests that regardless of the starting core metal, the particles have similar sizes and optical characteristics.

Extraction of PdAu DENs. Extraction of DENs from within dendrimer templates followed a previously established procedure that is briefly discussed in the Experimental Section.[52,55] The extraction model we have previously proposed involves two steps. First, a suitable

ligand, typically an alkylthiol, is added to a solution of DENs. The ligand penetrates the dendrimer periphery and adsorbs to the surface of the encapsulated nanoparticle. Second, the presence of the ligand weakens the interaction between the nanoparticle and the dendrimer. If the ligand/DEN interaction is sufficiently strong, then binding results in extraction of the DEN into an organic phase. The empty dendrimer remains in the aqueous phase.

The spectra in Figure 5.2 provide evidence for extraction of the bimetallic DENs into hexanes using dodecanethiol as the phase-transfer agent. Figure 5.2a shows spectra of the precursor G6-OH[Pd_{55}](Au_{92}) DENs, as well as both the aqueous and organic layers after extraction. The absorbance in the aqueous phase after extraction is negligible, indicating the absence of a detectable level of DENs. The spectrum of the organic layer is similar to that of the original DEN solution, indicating transfer of the metal nanoparticles to the organic phase. The small but significant changes in the magnitudes of the

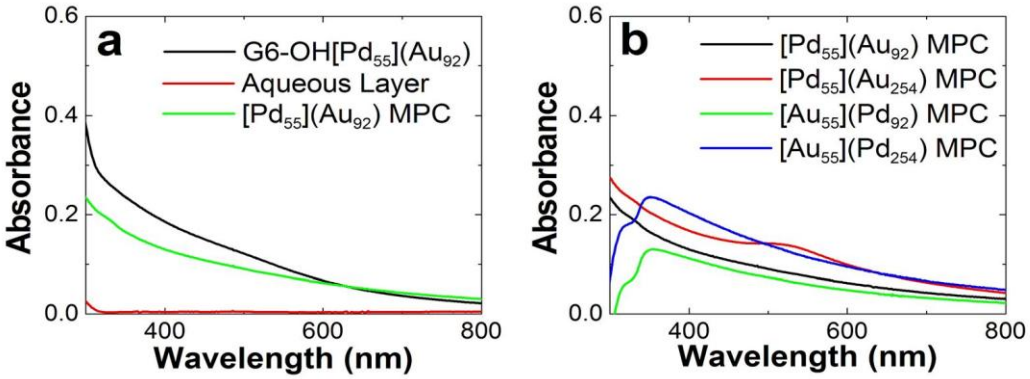

Figure 5.2. UV-vis spectra of PdAu DENs and MPCs prepared by extraction into hexanes using dodecanethiol as the phase transfer agent. (a) Spectra of an aqueous 2.00 μM G6-OH[Pd_{55}](Au_{92}) DEN solution prior to extraction, and the aqueous and hexane fractions after extraction. (b) Spectra for each MPC combination described in the text. These spectra are cut off below 300 nm because of the high absorbance of hexanes in this region. The path length of the cuvette was 0.20 cm.

absorbances may be related to differences in the ligands surrounding the nanoparticles (G6-OH vs. dodecanethiol) or the dielectric constants of water and hexanes.[58,61]

Figure 5.2b shows spectra for all four compositions of the extracted, bimetallic MPCs. The monotonically increasing absorbances at lower wavelengths are in accordance with expectations for metal particles in this size range.[1,65-68] A broad plasmon is observed for the $[Pd_{55}](Au_{254})$ MPCs, similar to that found previously for Au and AuAg alloy MPCs having the same size.[25] The shoulder at ~340 nm, and other differences in the spectra of the $[Pd_{55}](Au_x)$ and $[Au_{55}](Pd_x)$ MPCs near 300 nm, are a consequence of imperfect background subtraction (the solvent absorbs in this region). The important point is that MPCs having the same nominal size yield about the same absorbance at wavelengths > ~350 nm.

Size analysis by TEM. The size of the nanoparticles was determined by TEM. The diameters of the 55-atom Au and Pd seed DENs were both found to be 1.2 ± 0.3 nm (Figure 5.3).[1,48,49,52,53,55] This value is the same as for a 55-atom truncated cuboctahedron of these two metals.[48] When the second metal is added to the seeds, the particles become

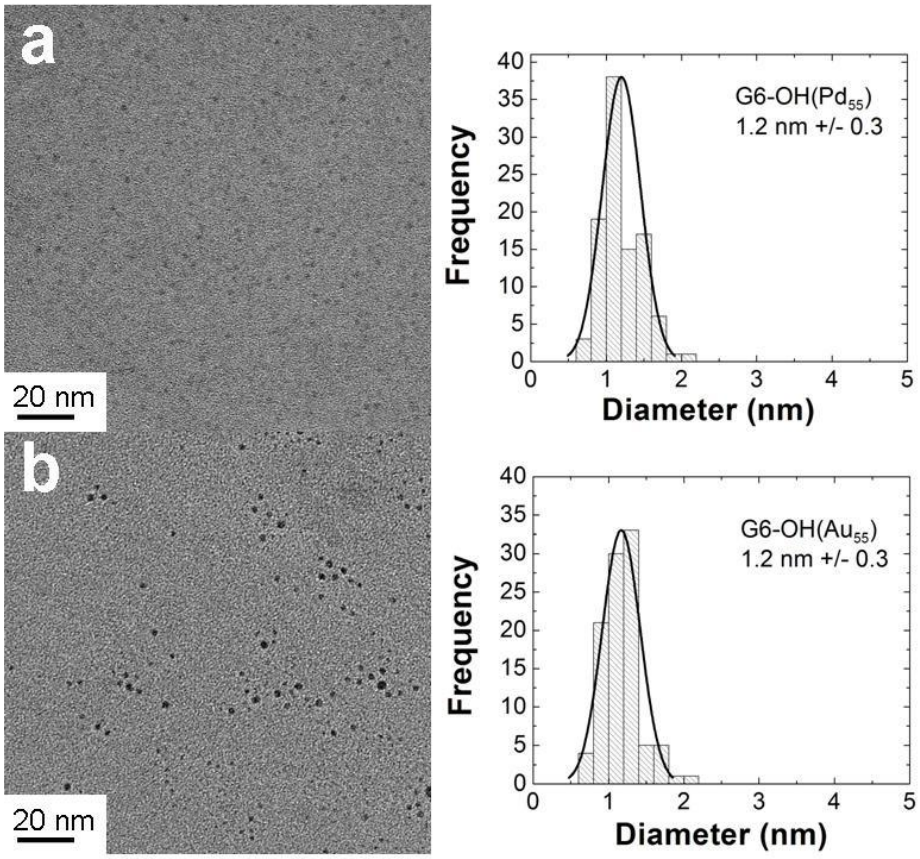

Figure 5.3. TEM micrographs and accompanying particle-size distribution histograms for (a) G6-OH(Pd_{55}) and (b) G6-OH(Au_{55}).

larger (Figure 5.4). The bimetallic nanoparticles formed by sequential reduction are slightly larger than the corresponding monometallic nanoparticles composed of the same number of metal atoms. For example, 147-atom Au and Pd DENs have previously been found to be 1.6 nm in diameter (calculated: 1.6 nm), while here the bimetallics average 2.0 ± 0.5 nm.[1,48,49] This increase may result from the presence of more atomic disorder in the bimetallics, but in any event the results are consistent with previous results obtained for DENs prepared by the sequential reduction method.[2]

Micrographs and histograms for the extracted MPCs are provided in Figure 5.5. The extracted, bimetallic MPCs are somewhat larger (0.2-0.3 nm) than the corresponding DENs. No such increase in size was evident in previous extraction experiments,[7,52,55] but in the present case it may be attributable to the incorporation of sulfur atoms from the alkylthiol into the Pd crystal structure. This type of configuration has been observed previously for other types of thiol-stabilized Pd nanoparticles and is discussed in more detail later.[69]

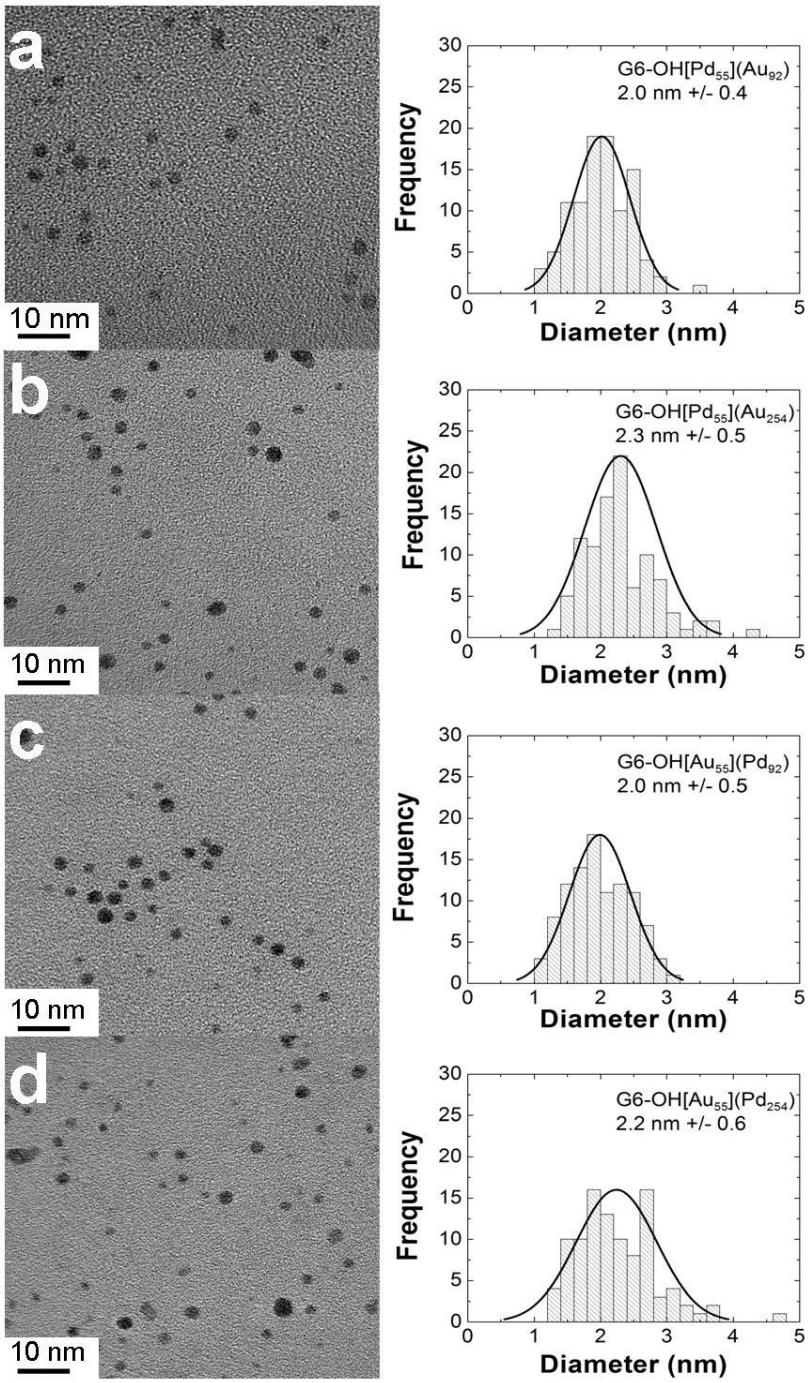

Figure 5.4. TEM micrographs and accompanying particle-size distribution histograms for the indicated DENs.

Structural analysis by EXAFS. EXAFS was used to determine the average local structure of the DENs and MPCs. In this analysis, the coordination numbers (CNs) for each sample are compared to those calculated for different structural models. For example, to determine the structure of bimetallic DENs, we consider six distinct CNs: n_{PP}, n_{PA}, n_{AA}, n_{PM}, n_{AM}, and n_{MM}, where n_{AP} is determined from n_{PA} and the stoichiometry of the particles. Here, *A* refers to Au, *P* to Pd, and *M* to any metal present (in this case, Au or Pd). The relationships between these CNs for an ideal, randomly alloyed nanoparticle have been discussed in detail elsewhere.[7] Briefly, n_{PP}, n_{PA}, and n_{AA} vary linearly with the stoichiometry, and the metal CNs are all equal ($n_{PM} = n_{AM} = n_{MM}$). The relevant values for the current stoichiometries were calculated and are provided in Figure 5.6a.

The CNs for an ideal cuboctahedral core-shell particle are more difficult to interpret, compared to monometallic particles, because there are fewer clear trends. The core metal (C) will have a n_{CC} similar to that of a smaller monometallic nanoparticle of the appropriate size. In this case, the CN for the core atoms resembles a 55-atom

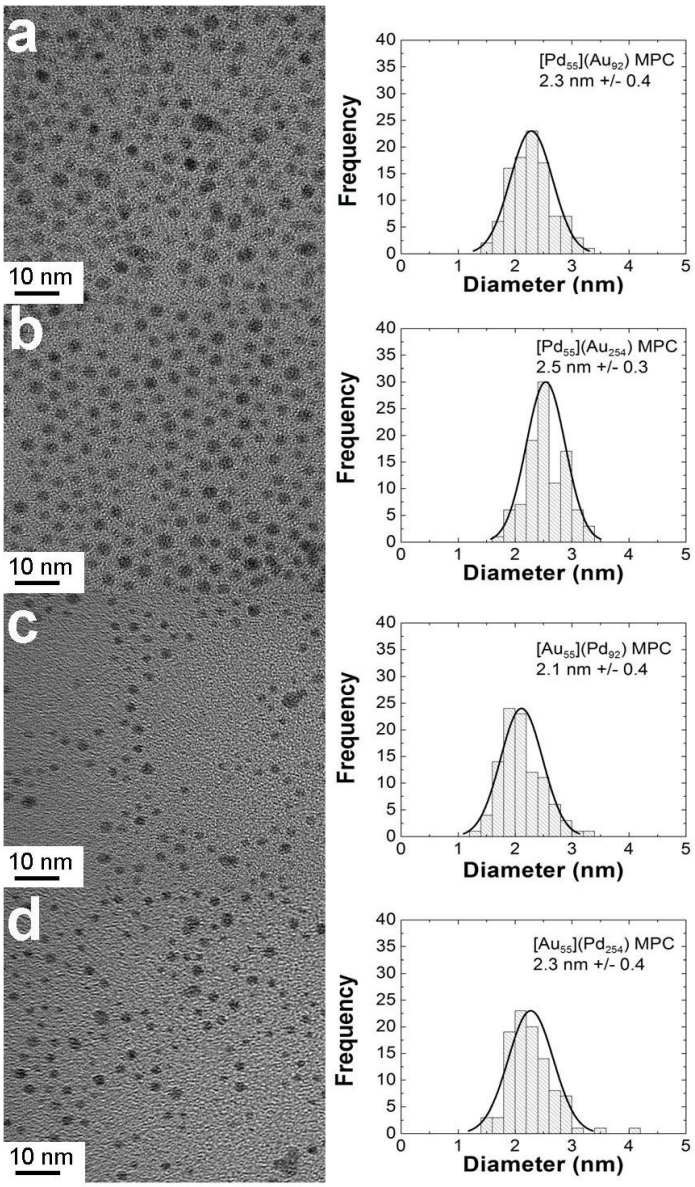

Figure 5.5. TEM micrographs and accompanying particle-size distribution histograms for the indicated MPCs.

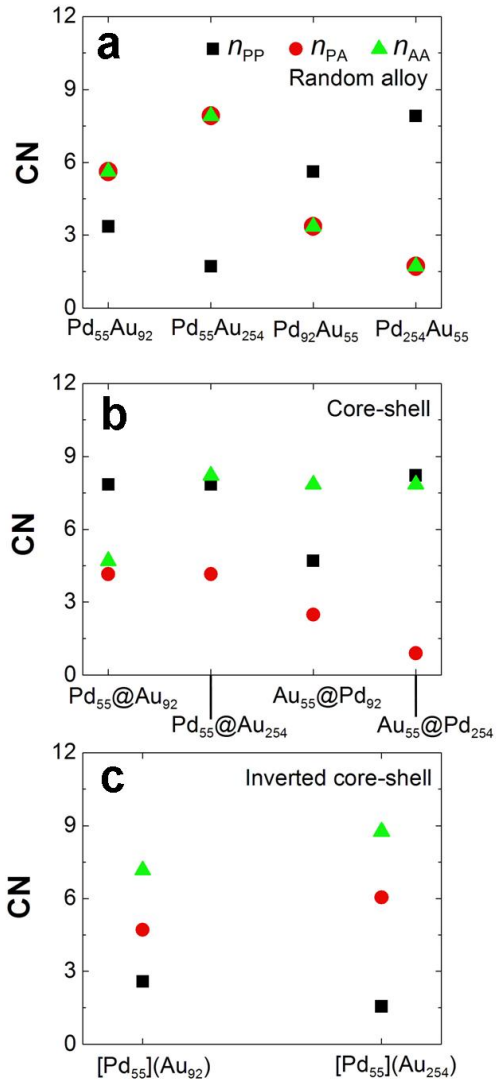

Figure 5.6. Calculated CNs for the following ideal nanoparticle configurations: (a) random alloy (theoretical), (b) core-shell, (c) inverted core-shell. Note that the CNs in (c) correspond to particles having Au cores and randomly configured PdAu shells. See text for additional information.

nanoparticle (n_{CC} = 7.85). However, the core is surrounded by shell atoms and therefore n_{CM} = 12, which is the bulk value. The metal CN for the shell metal (D) will be lower than 12, because the surface atoms are partially uncoordinated (n_{DM} < 12). The value for this CN will vary with the number of shells and size of the nanoparticle. For example, the nanoparticle size will determine n_{MM}, just as it does for a monometallic nanoparticle.[39,70,71] Furthermore, differences between observed and calculated core and shell CNs (n_{CM} and n_{DM}) may also arise due to interfacial disorder.

The values for the remaining CNs were calculated by generalizing the method previously described by Frenkel and coworkers to bimetallic particles.[38,39] First, Cartesian coordinates of a series of cuboctahedral clusters were generated. Next, depending on the overall cluster stoichiometry, the inner (core) cuboctahedral shells of the cluster were populated by atoms of one type (C), and the outer shells by atoms of the second type (D). In those cases where the outer shells consisted of a mixture of atoms, the C and D atoms were randomly distributed within the mixed composition shells as described below. Finally, the radial pair distribution function and accompanying CNs

of all pairs (n_{CC}, n_{CD}, n_{DC} and n_{DD}) were calculated using a method developed by Frenkel and coworkers.[72] Figure 5.6b plots the results of this calculation, and the corresponding structures are illustrated in Scheme 5.2.

In addition to the theoretically calculated random alloy model and the software-based core-shell models, CNs were also calculated for one other model: an inverted Pd@Au core-shell particle. That is, a Pd@Au core-shell nanoparticle inverted to a Au@Pd structure that retains the same atomic stoichiometry. For example, the inverted structure corresponds to moving the Pd atoms in Scheme 2a to the surface of the particle, and filling the new core with the Au atoms that were formerly in the shell. However, the number of metal atoms of each type remains the same: 55 Pd and 92 Au. Because the core of this 147-atom nanoparticle has space for 55 atoms, these are completely filled by Au. The remaining 37 (92-55) Au atoms must remain in the shell. The rest of the shell is occupied by the Pd atoms. This mixed-composition shell is assumed to be randomly occupied by Pd and Au atoms (Scheme 5.2c). The CNs for this inverted structure will vary depending on the shell configuration. For example, Scheme 5.2d shows two

Scheme 5.2

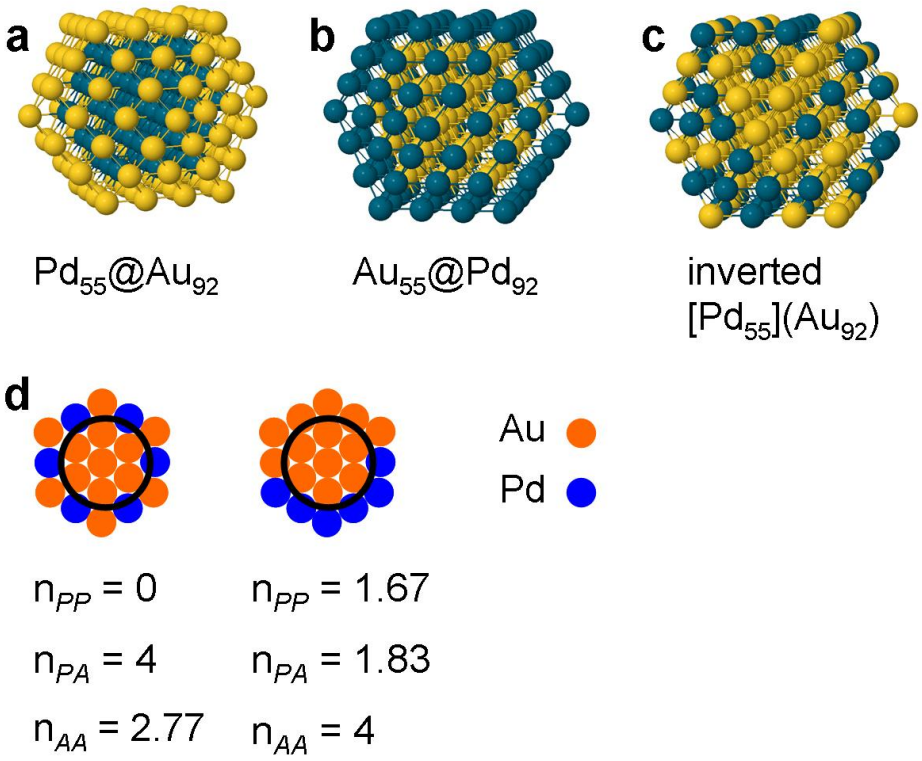
a
b
c
$Pd_{55}@Au_{92}$
$Au_{55}@Pd_{92}$
inverted
$[Pd_{55}](Au_{92})$
d
Au
Pd
$n_{PP} = 0$
$n_{PA} = 4$
$n_{AA} = 2.77$
$n_{PP} = 1.67$
$n_{PA} = 1.83$
$n_{AA} = 4$

quite different structures that could result from inversion: segregated and alternating. In both cases the numbers of Pd and Au atoms in the shell are identical. When these types of configurations are considered, the only consistent trend is that $n_{AM} > n_{MM} > n_{PM}$. To simplify the analysis, therefore, the CNs reported in Figure 5.6c are calculated assuming a random shell. Each of these idealized models should be viewed as an illustration of different structural trends, not as actual 3D structures, due to the distribution of particle sizes and structural disorder that are present in the nanoparticles prepared by most methods.

EXAFS scans of the DENs were collected for both the Pd and Au absorption edges. As many as 12 scans were aligned in energy, using a reference foil, and then the spectra were averaged to reduce statistical noise. The data for Pd and Au edges of the same sample were fit simultaneously in R-space using the Artemis program.[47] As in the previous chapter, the number of fitted variables was reduced by constraining the bond lengths and Debye-Waller factors for Pd-Au bonds to be equivalent for each edge, and by requiring the ratio of CNs of these bonds to be equal to

the ratio of their bulk compositions.[7] That is, for Pd_xAu_y, $n_{PA}/n_{AP} = y/x$.

EXAFS characterization of DENs. Parts a and b of Figure 5.7 provide an example of the k-space data for the G6-OH[Pd_{55}](Au_{92}) DENs for the Pd and Au edges, respectively. Parts c and d of Figure 5.7 provide the R-space data and fit results for the same material. The individual and metal CNs for all DEN configurations are plotted in parts e and f of Figure 5.7, respectively.

First, consider the CNs for the G6-OH[Pd_{55}](Au_{92}) DENs (Figures 5.7e). The n_{AA} is high (8.9 ± 1.0) when compared with n_{PP} (1.0 ± 2.2) and n_{PA} (3.3 ± 0.8). These results do not fit the alloy model where $n_{PA} = n_{AA} = 5.6$ (Figure 5.6a). Likewise, they do not match the trends of the core-shell model where $n_{PP} > n_{PA}$ and n_{AA} (Figure 5.6b). The model most closely matching the data is the inverted core-shell (Figure 5.6c). However, even this model is not a perfect fit to the data. We rationalize this as follows. First, there are variations in the possible shell configurations (Scheme 5.2d), and this will lead to a range of CNs. Second, we have previously shown that the structure of DENs

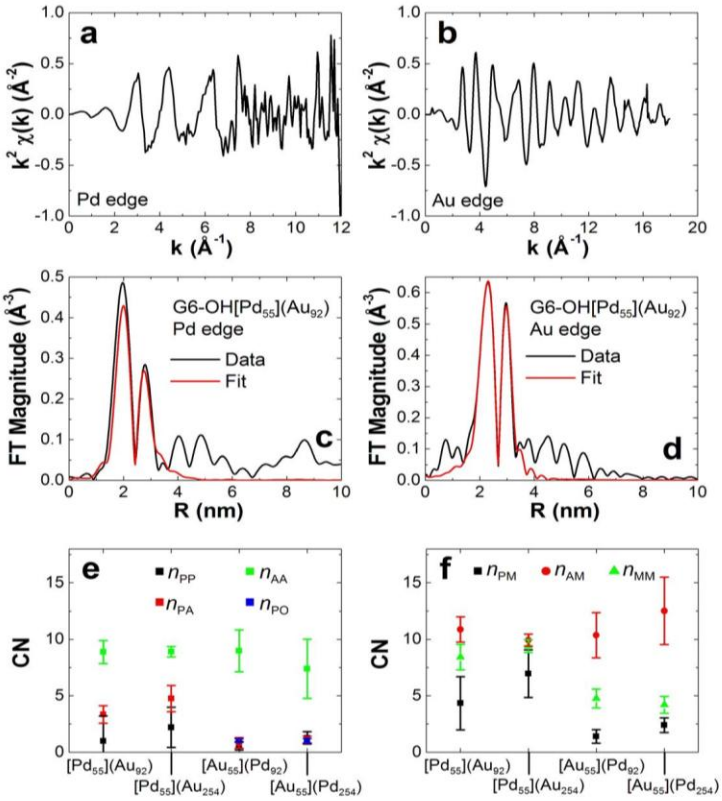

Figure 5.7. EXAFS data and corresponding fitting analyses for the DENs. k-space data are given for the (a) Pd K edge and (b) Au L_3 edge of G6-OH[Pd_{55}](Au_{92}) DENs. The corresponding Fourier transform magnitudes of the k^2-weighted data and fits are provided in frames (c) and (d), respectively. In frames (c) and (d), the data are plotted in black and the calculated fits are in red. The k-ranges from 2 $Å^{-1}$ to 8.3 $Å^{-1}$ and from 2.7 $Å^{-1}$ to 11 $Å^{-1}$ were used for the Pd and Au fits, respectively. The partial and metal CNs are summarized in frames (e) and (f), respectively.

may be somewhat amorphous, and therefore different from the cuboctahedral model assumed for the calculated CNs.[71,73]

Next, we examine the metal CN data for the G6-OH[Pd_{55}](Au_{92}) DENs (Figure 5.7f). These data also fit the expected trends ($n_{AM} > n_{MM} > n_{PM}$) for the inverted core-shell model, but not for the other two models we consider. Finally, the numerical value for the average metal CN, n_{MM}, is 8.4 ± 1.1, is close to the CN (9.0) for an ideal 147-atom truncated cuboctahedron.

The values of the CNs for the larger G6-OH[Pd_{55}](Au_{254}) DENs (Figure 5.7e) are also only consistent with the inverted core-shell model (n_{AA} = 8.9 ± 0.5, n_{PP} = 2.2 ± 1.8 and n_{PA} = 4.7 ± 1.2). The metal CNs (Figure 5.7f) fit the same trend as discussed for the G6-OH[Pd_{55}](Au_{92}) DENs. The average metal CN, n_{MM}, for this configuration is 9.4 ± 0.6, which is both larger than that of the smaller DENs and indistinguishable from the value for a perfect 309 atom truncated cuboctahedron (9.6).

Next we consider the Au core materials. The G6-OH[Au_{55}](Pd_{92}) DENs are different from the G6-OH[Pd_{55}](Au_x) DENs in that there is a significant contribution to the

EXAFS signal from Pd-O or Pd-N bonds. These types of interactions are indistinguishable, and therefore they are both modeled as Pd-O for simplicity and the CN is given as n_{PO}. This bonding is likely a combination of interactions between the Pd surface and amines or amides from the dendrimer, oxygen atoms (that is, PdO), OH^-, and H_2O.[56]

For G6-OH[Au_{55}](Pd_{92}), n_{AA} is relatively high (9.0 ± 1.9) while n_{PA} and n_{PP} are much lower (0.8 ± 0.5 and 0.6 ± 0.4). Because EXAFS is an ensemble averaging technique, there are two models that fit these data. Either there is a Au core nanoparticle with a loose, disordered Pd shell or there is a bimodal distribution of Au nanoparticles (capped with a small amount of Pd) and a large number of small (1-~5 atom), oxidized Pd clusters that are not closely associated with the Au nanoparticles. These two models can be distinguished by examining the metal CNs and comparing them with the UV-vis and TEM data. The n_{AM} (10.4 ± 2.0) is significantly higher than would be expected for a Au_{55} nanoparticle (7.9).[39,70] Therefore, the measured CN is consistent with the disordered Pd shell model, but not the bimodal distribution. The minimum fraction of oxidized Pd atoms necessary to account for a n_{PO} of 1.0 ± 0.2 is

approximately one quarter of the total Pd. In this case, a strong LMCT band at ~220 nm would be expected.[1,49,56] Because no such band is observed, the UV-vis data are also consistent with the Au core-disordered Pd shell model. Finally, the size of the G6-OH[Au_{55}](Pd_{92}) particles measured by TEM is larger than previously observed for monometallic DENs containing the same total number (147) of atoms.[1,49,73] In the bimodal distribution model, the size should be less than or equal to that of the corresponding monometallic DENs. Note also that the average metal coordination number, n_{MM}, is significantly lower (4.8 ± 0.8) than that of the G6-OH[Pd_{55}](Au_{92}) DENs, probably due to disorder in the Pd shell, and is lower than that of the calculated, ideal nanoparticles (9.0). We conclude that the G6-OH[Au_{55}](Pd_{92}) DENs have a Au@Pd structure, with the Pd shell showing disorder from bonding with O.

The analysis of the G6-OH[Au_{55}](Pd_{254}) DENs is similar to that of the just-discussed G6-OH[Au_{55}](Pd_{92}) DENs. The n_{AA} (7.4 ± 2.6) is again higher than n_{PA} (1.1 ± 0.3), n_{PP}(1.3 ± 0.6), and n_{PO} (1.0 ± 0.2). The CN, n_{AM} (12.5 ± 3.0), is again consistent with a Au core. The same arguments as above are used with the UV-vis and TEM data, resulting in a

Au@Pd structure having a partial oxidized Pd shell. The partial oxidation of the Pd shell and accompanying disorder lower the average metal CN, n_{MM}.

EXAFS Analysis of MPCs. The approach for analyzing extracted MPCs is very similar to that used for the DENs, but in this case the presence of metal bonds to sulfur must also be considered. An example of the k- and R-space data, the fitting analysis and a summary of the CNs are found in Figure 5.8. For all of the MPCs, n_{AA} and n_{AM} remain high compared to n_{PP} and n_{PM} indicating that the Au atoms are in the core of the material. In addition, the Au-S CN, n_{AS}, is low, indicating that few Au atoms are available for binding to S atoms. For the $[Pd_{55}](Au_{254})$ MPCs, Au-S bonds do not contribute significantly to the fit but Pd-S bonds do. The n_{PS} ranges from 0.4 ± 0.5 for $[Pd_{55}](Au_{92})$ to 3.1 ± 2.7 for $[Pd_{55}](Au_{254})$. Because the maximum possible Pd-S CN is 4, these results indicate that more than a surface layer of thiols is present.[69,73] Accordingly, we propose a model in which the outer layers of the nanoparticle are penetrated by the thiol head groups. This leads to disordering of the Pd shell and hence a lower-than-expected n_{PP} and a correspondingly higher-than-expected n_{PS}. The alternative

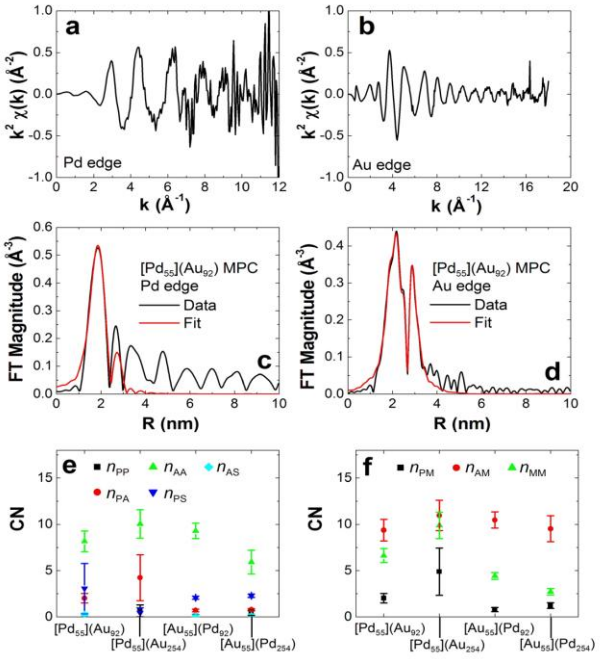

Figure 5.8. EXAFS data and corresponding fitting analyses for the MPCs. k-space data are given for the (a) Pd K edge and (b) Au L_3 edge of $[Pd_{55}](Au_{92})$ MPCs. The corresponding Fourier transform magnitudes of the k^2-weighted data and fits are provided in frames (c) and (d), respectively. In frames (c) and (d), the data are plotted in black and the calculated fits are in red. The k-ranges from 3 $Å^{-1}$ to 10 $Å^{-1}$ and from 3.2 $Å^{-1}$ to 15 $Å^{-1}$ were used for the Pd and Au fits, respectively. The partial and metal CNs are summarized in frames (e) and (f), respectively.

model, which invokes the presence of a bimodal distribution of small Pd-S particles and MPCs, is not consistent with the sizes measured by TEM. Additionally, the absence of a significant Au-S contribution to the EXAFS fits suggests that Au must be confined within a protective shell of Pd and hence shielded from S atoms.

Selective catalytic reactions. The reduction of resazurin to resorufin is a well-known and frequently used biological assay.[74,75] Both compounds have a strong, distinct absorbance in the visible range (λ_{max} = 602 and 572 nm, respectively, at basic pH),[76] and there is a large difference in their fluorescence quantum yield.[77] As recently shown by Chen and coworkers,[4] this reduction is catalyzed by Au nanoparticles in the presence of amines. However, we have carried out control experiments demonstrating that this reaction is not catalyzed by Pd DENs or by the tertiary amines of the dendrimer. Accordingly, the catalytic conversion of resazurin to resorufin can be used as a probe for the composition of the surface of PdAu nanoparticles. That is, the reaction should only proceed in the presence of a Au shell. Note

also that a very dilute concentration (40 nM) of Au nanoparticles is sufficient to catalyze this reaction.

Figure 5.9 shows the absorbance spectra in the region of interest for resazurin and resorufin. A complete UV-vis spectrum is provided in Figure 5.10. Part a of Figure 5.9 shows the effect on the conversion of resazurin in the presence of G6-OH only, and monometallic, 147-atom Au and Pd DENs. Initially, all three solutions exhibited the deep blue color typical of resazurin. There is no spectral change in the presence of the dendrimer or the Pd DENs, but upon exposure to Au DENs the color of the solution changes to the bright pink color of resorufin. This change is observed in part a of Figure 5.9 as a shift in λ_{max} from 602 nm to 571 nm and in the shape of the spectrum. Additional control experiments were carried out for conditions similar to those used to prepare the monometallic and bimetallic DENs, but with no metals added. These data are not shown, because there was no detectable conversion of resazurin to resorufin.

Part b of Figure 5.9 presents spectra for the sequentially reduced DENs, G6-OH[Pd_{55}](Au_{92}) and G6-OH[Au_{55}](Pd_{92}), and those prepared by co-complexation with

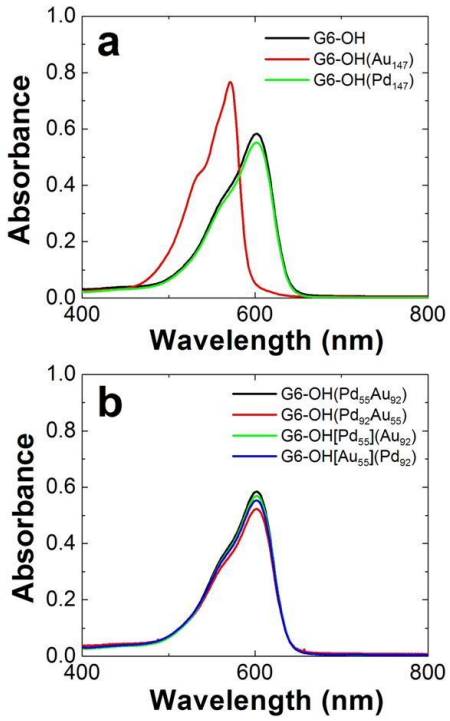

Figure 5.9. UV-vis spectra illustrating the results for the DEN-catalyzed conversion of resazurin to resorufin. (a) Spectra for G6-OH and monometallic Au and Pd DENs consisting of an average of 147 atoms. Only the Au DENs are catalytically active. (b) Spectra showing that DENs prepared by sequential reduction and co-complexation do not catalyze the resazurin-to-resorufin reaction. Spectra were measured in water, the path length of the cuvette was 0.20 cm, and the concentrations of DENs and resazurin were 40 nM and 10 μM, respectively.

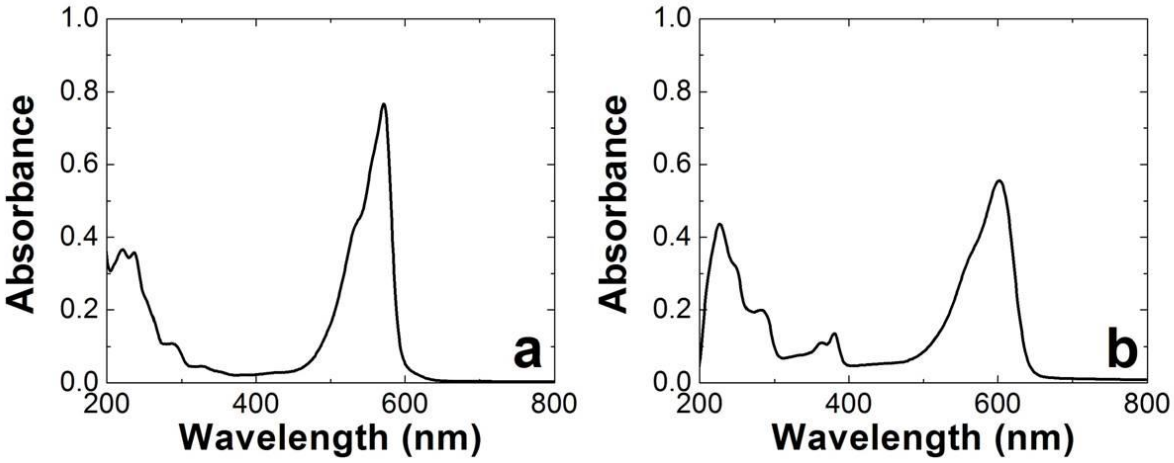

Figure 5.10. UV-vis spectra of the resazurin experiment for (a) G6-OH(Au_{55}) and (b) G6-OH[Pd_{55}](Au_{254}). (a) a positive result representing conversion of resazurin to resorufin. (b) is a negative result. The conversion is particularly noticeable at 600 nm. The DENs are low enough in concentration (40 nM) that they do not absorb significantly in this spectral region.

the same stoichiometry: G6-OH($Pd_{55}Au_{92}$) and G6-OH($Pd_{92}Au_{55}$). None of these bimetallic nanoparticles catalyze the conversion of resazurin to resorufin. The catalysis results for DENs prepared by sequential reduction are in agreement with the EXAFS analysis, which showed that the Au atoms are predominantly located within the interior of the particles rather than on the surface. It is somewhat surprising that the same result is obtained for the DENs prepared by co-complexation, because our previous EXAFS results showed that some Au atoms are on the surface of these nanoparticles.[7] This suggests that this catalytic reaction requires particular configurations of Au atoms on the particle surface. For example, isolated Au atoms may be less catalytically active compared to, for example, Au atoms on the surface of G6-OH(Au_{55}) monometallic DENs. Consistent with this view, Goodman and coworkers have recently observed that contiguous Pd atoms on a Au surface promote CO oxidation.[78] A similar argument can be made for the lack of catalytic activity of G6-OH[Pd_{55}](Au_{254}) DENs, which must have some Au on the surface because of the large Au:Pd ratio.

5.5 Summary and Conclusions

We have prepared PdAu DENs via the two sequential reduction methods shown in Scheme 5.1. When Au is reduced onto 55-atom, preformed Pd DEN cores, the data analysis leads to a model consistent with inversion of the two metals. That is, Au migrates into the core and Pd resides on the surface. However, when Pd is reduced onto a 55-atom Au core, the expected Au@Pd structure results. However, in this latter case, the EXAFS analysis suggests partial oxidation of the relatively thick Pd shell. The absence of such oxidation in the inverted structures is likely a consequence of the relatively low surface concentration of Pd in these materials, and an apparent stabilization of surface Pd by Au. When the DENs are extracted from their protective dendrimer stabilizers by alkylthiols, the resulting MPCs retain the original Au@Pd structures. However, the presence of the thiol groups leads to some subtle structural changes in the Pd shells that are revealed by EXAFS.

Results relating to the catalytic conversion of resazurin to resorufin by DENs are especially interesting. We find that monometallic G6-OH(Au_{147}) and G6-OH(Au_{55}) DENs

efficiently catalyze this reaction. In contrast, none of the PdAu DENs prepared by sequential reduction are active. This result is certainly consistent with the presence of a Au core surrounded by a protective Pd shell, as suggested by EXAFS. Interestingly, however, the G6-OH[Pd_{55}](Au_{254}) DENs, which must have a substantial number of Au atoms on their surfaces (due to high Au:Pd ratio) after inversion, are still not catalytically active. This suggests that the conversion of resazurin to resorufin requires particular spatial relationships between Au atoms that are not present on sequentially reduced PdAu DENs. Indeed, even PdAu DENs prepared by co-complexation, which have quasirandom alloy structures, are not catalytically active for this reaction.

The key conclusion from this work is that correlation of structure to catalytic function for very small, bimetallic nanoparticles requires detailed information about atomic configuration. Underscoring this point is our finding that the synthesis of bimetallic PdAu nanoparticles may yield unanticipated structures, such as the inverted Au@Pd DENs reported here. Clearly the structure of nanoparticles in the < 2 nm size range may be controlled by factors that are, at present, not understood.

Unfortunately, unambiguous structure determination for particles in this size range remains a major analytical challenge.

References

1. Scott, R. W. J.; Wilson, O. M.; Crooks, R. M. *J. Phys. Chem. B* **2005**, *109*, 692-704.

2. Scott, R. W. J.; Wilson, O. M.; Oh, S. K.; Kenik, E. A.; Crooks, R. M. *J. Am. Chem. Soc.* **2004**, *126*, 15583-15591.

3. Wilson, O. M.; Scott, R. W. J.; Garcia-Martinez, J. C.; Crooks, R. M. *J. Am. Chem. Soc.* **2005**, *127*, 1015-1024.

4. Xu, W.; Kong, J. S.; Yeh, Y.-T. E.; Chen, P. *Nature Mater.* **2008**, *7*, 992-996.

5. Endo, T.; Yoshimura, T.; Esumi, K. *J. Colloid Interface Sci.* **2005**, *286*, 602-609.

6. Hoover, N. N.; Auten, B. J.; Chandler, B. D. *J. Phys. Chem. B* **2006**, *110*, 8606-8612.

7. Knecht, M. R.; Weir, M. G.; Frenkel, A. I.; Crooks, R. M. *Chem. Mater.* **2008**, *20*, 1019-1028.

8. Lang, H.; Maldonado, S.; Stevenson, K. J.; Chandler, B. D. *J. Am. Chem. Soc.* **2004**, *126*, 12949-12956.

9. Knecht, M. R.; Garcia-Martinez, J. C.; Crooks, R. M. *Chem. Mater.* **2006**, *18*, 5039-5044.

10. Knecht, M. R.; Garcia-Martinez, J. C.; Crooks, R. M. *Langmuir* **2005**, *21*, 11981-11986.

11. Beakley, L. W.; Yost, S. E.; Cheng, R.; Chandler, B. D. *Appl. Catal. A* **2005**, *292*, 124-129.

12. Bustos, E. B.; Jimenez, M. G. G.; Diaz-Sanchez, B. R.; Juaristi, E.; Chapman, T. W.; Godinez, L. A. *Talanta* **2007**, *72*, 1586-1592.

13. Chung, Y.-M.; Rhee, H.-K. *Catal. Lett.* **2003**, *85*, 159.

14. Gilbertson, J. D.; Vijayaraghavan, G.; Stevenson, K. J.; Chandler, B. D. *Langmuir* **2007**, *23*, 11239-11245.

15. Hendricks, T. R.; Dams, E. E.; Wensing, S. T.; Lee, I. *Langmuir* **2007**, *23*, 7404-7410.

16. Knecht, M. R.; Crooks, R. M. *New J. Chem.* **2007**, *31*, 1349-1353.

17. Lafaye, G.; Siani, A.; Marecot, P.; Amiridis, M. D.; Williams, C. T. *J. Phys. Chem. B* **2006**, *110*, 7725-7731.

18. Mark, S. S.; Bergkvist, M.; Yang, X.; Angert, E. R.; Batt, C. A. *Biomacromolecules* **2006**, *7*, 1884-1897.

19. Pittelkow, M.; Brock-Nannestad, T.; Moth-Poulsen, K.; Christensen, J. B. *Chem. Commun.* **2008**, 2358-2360.

20. Satoh, N.; Nakashima, T.; Kamikura, K.; Yamamoto, K. *Nature Nanotech.* **2008**, *3*, 106-111.

21. Huang, W.; Kuhn, J. N.; Tsung, C.-K.; Zhang, Y.; Habas, S. E.; Yang, P.; Somorjai, G. A. *Nano Lett.* **2008**, *8*, 2027-2034.

22. Ye, H.; Crooks, R. M. *J. Am. Chem. Soc.* **2007**, *129*, 3627-3633.

23. Scott, R. W. J.; Sivadinarayana, C.; Wilson, O. M.; Yan, Z.; Goodman, D. W.; Crooks, R. M. *J. Am. Chem. Soc.* **2005**, *127*, 1380-1381.

24. Murray, R. W. *Chem. Rev.* **2008**, *108*, 2688-2720.

25. Templeton, A. C.; Wuelfing, W. P.; Murray, R. W. *Acc. Chem. Res.* **2000**, *33*, 27-36.

26. Auten, B. J.; Hahn, B. P.; Vijayaraghavan, G.; Stevenson, K. J.; Chandler, B. D. *J. Phys. Chem. C* **2008**, *112*, 5365-5372.

27. Garcia, M. E.; Baker, L. A.; Crooks, R. M. *Anal. Chem.* **1999**, *71*, 256-258.

28. Ferrando, R.; Jellinek, J.; Johnston, R. L. *Chem. Rev.* **2008**, *108*, 845-910.

29. Mandal, S.; Mandale, A. B.; Sastry, M. *J. Mater. Chem.* **2004**, *14*.

30. Perez-Tijerina, E.; Pinilla, M. G.; Mejia-Rosales, S.; Ortiz-Mendez, U.; Torres, A.; Jose-Yacaman, M. *Faraday Discuss.* **2008**, *138*, 353-362.

31. Wu, M. L.; Chen, D. H.; Huang, T. C. *Langmuir* **2001**, *17*, 3877-3883.

32. Harpeness, R.; Gedanken, A. *Langmuir* **2004**, *20*, 3431-3434.

33. Jose, D.; Jagirdar, B. R. *J. Phys. Chem. C* **2008**, *112*, 10089-10094.

34. Kan, C., Cai, W.;Li, C.; Zhang, L.; Hofmeister, H. *J. Phys. D: Appl. Phys.* **2003**, *36*, 1609-1614.

35. Ferrer, D.; Blom, D. A.; Allard, L. F.; Mejia, S.; Perez-Tijerina, E.; Jose-Yacaman, M. *J. Mater. Chem.* **2008**, *18*, 2442-2446.

36. Mejia-Rosales, S. J.; Fernandez-Navarro, C.; Perez-Tijerina, E.; Blom, D. A.; Allard, L. F.; Jose-Yacaman, M. *J. Phys. Chem. C* **2007**, *111*, 1256-1260.

37. Liu, H. B.; Pal, U.; Perez, R.; Ascencio, J. A. *J. Phys. Chem. B* **2006**, *110*, 5191-5195.

38. Frenkel, A. I. *Z. Kristallogr.* **2007**, *222*, 605-611.

39. Glasner, D.; Frenkel, A. I. *XAFS 13, Proc. Int. Conf. X-ray Absorpt. Fine Struct.* **2007**, *882*, 746-748.

40. Hwang, B. J.; Sarma, L. S.; Chen, J.-M.; Chen, C. H.; Shih, S.-C.; Wang, G. R.; Liu, D. G.; Lee, J. F.; Tang, M. T. *J. Am. Chem. Soc.* **2005**, *127*, 11140-11145.

41. Toshima, N.; Harada, M.; Yamazaki, Y.; Asakura, K. *J. Phys. Chem.* **1992**, *96*, 9927-9933.

42. Harada, M.; Asakura, K.; Toshima, N. *J. Phys. Chem.* **1993**, *97*, 5103-5114.

43. Chen, C.-H.; Sarma, L. S.; Chen, J.-M.; Shih, S.-C.; Wang, G.-R.; Liu, D.-G.; Tang, M.-T.; Lee, J.-F.; Hwang, B.-J. *ACS Nano* **2007**, *1*, 114-125.

44. Davis, R. J.; Boudart, M. *J. Phys. Chem.* **1994**, *98*, 5471-5477.

45. Reifsnyder, S. N.; Lamb, H. H. *J. Phys. Chem. B* **1999**, *103*, 321-329.

46. Zhang, P.; Zhou, X.; Tang, Y.; Sham, T. K. *Langmuir* **2005**, *21*, 8502-8508.

47. Newville, M. *J. Synchrotron Radiat.* **2001**, *8*, 322-324.

48. Kim, Y. G.; Oh, S. K.; Crooks, R. M. *Chem. Mater.* **2004**, *16*, 167-172.

49. Scott, R. W. J.; Ye, H.; Henriquez, R. R.; Crooks, R. M. *Chem. Mater.* **2003**, *15*, 3873-3878.

50. Kim, Y. H.; Nakano, Y. *Water Res.* **2005**, *39*, 1324.

51. Tait, C. D.; Janecky, D. R.; Rogers, P. S. Z. *Geochim. Cosmochim. Acta* **1991**, *55*, 1253-1264.

52. Garcia-Martinez, J. C.; Crooks, R. M. *J. Am. Chem. Soc.* **2004**, *126*, 16170-16178.

53. Kim, Y. G.; Garcia-Martinez, J. C.; Crooks, R. M. *Langmuir* **2005**, *21*, 5485-5491.

54. Wilson, O. M.; Scott, R. W. J.; Garcia-Martinez, J. C.; Crooks, R. M. *Chem. Mater.* **2004**, *16*, 4202-4204.

55. Garcia-Martinez, J. C.; Scott, R. W. J.; Crooks, R. M. *J. Am. Chem. Soc.* **2003**, *125*, 11190-11191.

56. Carino, E. V.; Knecht, M. R.; Crooks, R. M. *Langmuir* **2009**, *25*, 10279-10284

57. Zhao, M.; Crooks, R. M. *Chem. Mater.* **1999**, *11*, 3379-3385.

58. Alvarez, M. M.; Khoury, J. T.; Schaaff, T. G.; Shafigullin, M. N.; Vezmar, I.; Whetten, R. L. *J. Phys. Chem. B* **1997**, *101*, 3706-3712.

59. Daniel, M. C.; Astruc, D. *Chem. Rev.* **2004**, *104*, 293-346.

60. Roldughin, V. I. *Russ. Chem. Rev. (Engl. Transl.)* **2000**, *69*, 821-843.

61. Link, S.; El-Sayed, M. A. *Int. Rev. Phys. Chem.* **2000**, *19*, 409.

62. Pande, S.; Crooks, R. M. **2010**, In Preparation.

63. Mulvaney, P. *Langmuir* **1996**, *12*, 788-800.

64. Zheng, J.; Petty, J. T.; Dickson, R. M. *J. Am. Chem. Soc.* **2003**, *125*, 7780-7781.

65. Bauer, C.; Abid, J.-P.; Girault, H. H. *Chem. Phys.* **2005**, *319*, 409-421.

66. Lim, I. S.; Pan, Y.; Mott, D.; Ouyang, J.; Njoki, P. N.; Luo, J.; Zhou, S.; Zhong, C.-J. *Langmuir* **2007**, *23*, 10715-10724.

67. Link, S.; Burda, C.; Wang, Z. L.; El-Sayed, M. A. *J. Chem. Phys.* **1999**, *111*, 1255-1264.

68. Quinten, M. *Appl. Phys. B* **2001**, *73*, 317-326.

69. Sun, Y.; Frenkel, A. I.; Isseroff, R.; Shonbrun, C.; Forman, M.; Shin, K.; Koga, T.; White, H.; Zhang, L.; Zhu, Y.; Rafailovich, M. H.; Sokolov, J. C. *Langmuir* **2006**, *22*, 807-816.

70. Jentys, A. *Phys. Chem. Chem. Phys.* **1999**, *1*, 4059-4063.

71. Knecht, M. R.; Weir, M. G.; Myers, V. S.; Pyrz, W. D.; Ye, H.; Petkov, V.; Buttrey, D. J.; Frenkel, A. I.; Crooks, R. M. *Chem. Mater.* **2008**, *20*, 5218-5228.

72. Frenkel, A. I.; Frankel, S. C.; Liu, T. *Phys. Scr.* **2005**, *T115*, 721-723.

73. Petkov, V.; Bedford, N.; Knecht, M. R.; Weir, M. G.; Crooks, R. M.; Tang, W.; Henkelman, G.; Frenkel, A. *J. Phys. Chem. C* **2008**, *112*, 8907-8911.

74. Karakashev, D.; Galabova, D.; Simeonov, I. *World J. Microbiol. Biotechnol.* **2003**, *19*, 233-238.

75. Chapin, K. C.; Lauderdale, T.-L., Manual of Clinical Microbiology (Editor: P. R. Murray), ASM Press, Washington, D. C., 2007.

76. Bueno, C.; Villegas, M. L.; Bertolotti, S. G.; Previtali, C. M.; Neumann, M. G.; Encinas, M. V. *Photochem. Photobiol.* **2002**, *76*, 385-390.

77. Guilbault, G. G.; Kramer, D. N. *Anal. Chem.* **1965**, *37*, 1219-1221.

78. Gao, F.; Wang, Y.; Goodman, D. W. *J. Am. Chem. Soc.* **2009**, *131*, 5734-5735.

Chapter 6: In-situ X-ray Absorption Analysis of ~1.8 nm Dendrimer-Encapsulated Platinum Nanoparticles During Electrochemical CO Oxidation

6.1 Synopsis

We report an in-situ X-ray absorption-fine structure (XAFS) spectroscopic analysis of ~1.8 nm Pt dendrimer-encapsulated nanoparticles (DENs) during electrocatalytic oxidation of CO. The results indicate that Pt nanoparticles encapsulated within poly(amidoamine) (PAMAM) dendrimers and immobilized on a carbon electrode retain their electrocatalytic activity and are structurally stable for extended periods during CO oxidation. This is a significant finding, because nanoparticles in this size range are good experimental models for comparison to first-principles calculations if they remain stable during catalytic reactions.

6.2 Introduction

Here we report an in-situ X-ray absorption-fine structure (XAFS) spectroscopic analysis of ~1.8 nm Pt dendrimer-

encapsulated nanoparticles (DENs) during electrocatalytic oxidation of CO. These results represent a significant advance in understanding the structure and stability of very small nanoparticles under catalytic conditions. Specifically, the data indicate that Pt nanoparticles encapsulated within poly(amidoamine) (PAMAM) dendrimers retain their electrocatalytic activity and are structurally stable for extended periods during CO oxidation. This is important, because Pt DENs, and DENs in general, are a good experimental model for studying catalytic reactions at nanoparticles containing 40-240 atoms. This is the interesting size range in which nanomaterials undergo rapid transitions in chemical and physical properties.[1-2] Moreover, the lower end of this range is compatible with first-principles calculations, and therefore there is an opportunity to directly compare theory to experimental results if the catalysts retain their structural integrity during the time required to make catalytic rate measurements.[3]

Pt DENs containing an average of 40 – 240 atoms have previously been prepared within fourth- and sixth-generation PAMAM dendrimers.[4-8] The synthesis involves two

steps. First the Pt complex, $PtCl_4^{2-}$, undergoes water substitution, and then it reacts with interior tertiary amines of the dendrimer. Second, addition of $NaBH_4$ results in reduction of the coordinated Pt ions to atoms, which quickly coalesce into nanoparticles. We have recently shown that this synthesis yields a bimodal distribution of products: roughly half the dendrimers contain fully reduced Pt nanoparticles, and the other half contain unreduced Pt^{2+} (here we denote all forms of unreduced platinum as Pt^{2+}, even though Pt^{2+} may be coordinated to the dendrimer, OH^-, Cl^-, or other species present in solution).[5] Pt DENs, and alloys thereof, can be immobilized onto electrode surfaces and are active for the oxygen reduction reaction (ORR),[7-9] CO oxidation,[7] H^+ reduction,[7] and H_2 oxidation.[7] We have previously reported that the rate of the ORR is a sensitive function of catalyst size,[7] and that the rate of the ORR at PtPd bimetallic DENs depends on the relative composition of the two metals.[9]

In addition to our own studies of Pt DENs, there have been numerous experimental and theoretical reports from other groups.[4,10-17] For example, Miyahara and coworkers recently demonstrated that the reaction between interior

tertiary amines of PAMAM dendrimers and Pt^{2+} is temperature dependent.[17] Amiridis and coworkers explored the platinum-dendrimer system using a slightly different synthetic technique that did not result in reduction of the precursor complex.[4] Yamamoto et al. examined the electrocatalytic properties of Pt DENs for the ORR using a different type of dendrimer and reported exceptional catalytic activity for the smallest (~1 nm) nanoparticles.[18]

While the structural characteristics of DENs are beginning to emerge, very little is known about their properties during catalytic reactions. As mentioned earlier, our primary interest in DENs is in directly correlating first-principles theory to experimental catalytic rate measurements. For this purpose, it is essential that the structure of the catalyst remain unchanged (or at least that the changes be understood) *in operando*. As a first step toward understanding how DEN structure evolves during catalysis, we examined the oxidation of CO to CO_2. This reaction has specific characteristics that make it appropriate for this study. First, the rate of this reaction is easily controlled via the electrode potential. Second, the intermediate species,

adsorbed CO, can be retained on the electrode surface long enough to obtain XAFS spectra. Finally, this electrochemical reaction has been studied extensively both on single-crystal Pt and on nanoparticles, and therefore benchmarks exist for interpreting results.[19-22] For example, CO adsorption on Pt/Cu near-surface alloys results in a Cu-rich surface due to the enhanced strength of the Pt-CO bond in the presence of a Pt/Cu surface alloy.[23] Additionally, it has been shown that Pt nanoparticles agglomerate during CO adsorption and oxidation.[21,24] Markovic and coworkers have used repeated potential cycling in a CO-rich solution to restructure the surface of Pt nanoparticles in their studies of particle-size effects.[19,22] This group also found that adsorption of OH at surface defect sites affects the potential for CO oxidation.

Extended XAFS (EXAFS) provides information about the local environment of atoms in nanoparticles like DENs. This information includes the chemical identity, average bond lengths, and ensemble-average coordination number (CN) of atoms close to the x-ray absorbing atom.[25] X-ray absorption near-edge structure (XANES) contains information about the charge state of the absorbing atom, and therefore

it is sensitive to the oxidation state of the absorber and its changes during in-situ transformations. EXAFS and XANES data can both be collected in-situ during electrochemical reactions, but for Pt nanoparticles less than ~5 nm in diameter, such studies have largely been confined to applications related to fuel cells.[26-41] These prior studies are distinguished from the results presented here by the size and composition of the catalyst and its support. For example, Russell and coworkers studied the adsorption of CO to commercial, carbon-supported Pt catalysts ranging in size from 1-10 nm and reported sensitivity to surface adsorbates. Specifically, they were able to detect both CO and Pt oxides, and they could distinguish between Pt-CO and Pt-support interactions.[33] Adzic and coworkers studied the ORR at core-shell particles consisting of Pt monolayers on nano-sized substrates including NbO_2.[37] In these studies, the Pt interatomic distance could be controlled by changing the core material, and this in turn led to tuning of the catalytic activity.

Here, Pt DENs containing an average of 240 atoms were encapsulated within sixth-generation, hydroxyl-terminated PAMAM dendrimers (G6-OH), and then immobilized onto carbon

paper electrodes. The CNs were measured in electrolyte solution before and after application of an electrode potential, and before, during, and after CO adsorption. Two significant results emerge from this study. First, the Pt CN of the electrode-immobilized DENs increases significantly after the first application of a reducing potential and then it remains constant. This result is consistent with our previous study,[5] and it suggests that the fraction of unreduced Pt DEN precursors originally present after BH_4^- reduction is converted to fully reduced DENs by the potential applied to the electrode. Second, CO adsorbs to Pt DENs and is then electrochemically oxidized to CO_2 without measurable change to the encapsulated nanoparticles. This is an important finding, because it means these DENs are dimensionally stable on the timescale of the XAFS measurements. Accordingly, the effect of DEN size and composition on catalytic reactions can be studied without fear of time-dependent agglomeration or other changes.

6.3 Experimental Section

Chemicals. G6-OH dendrimers were purchased from Dendritech, Inc. (Midland, MI) as 10.0% solutions in methanol. Before use, this solution was dried under vacuum at 22 °C and then reconstituted in sufficient deionized water to make a 100 μM solution. All other chemicals were used as received. K_2PtCl_4 and $NaBH_4$ were purchased from Sigma-Aldrich (Milwaukee, WI). High-purity H_2SO_4 and $HClO_4$ were purchased from J.T. Baker (Phillipsburg, NJ). The carbon paper was AvCarb Grade-P75, purchased from Ballard Material Products (Lowell, MA). Au foil and wire (99.9%) were obtained from Alfa Aesar (Ward Hill, MA). Aqueous solutions were prepared using 18 MΩ·cm Milli-Q water (Millipore, Bedford, MA).

DEN synthesis. DENs consisting of sixth-generation, hydroxyl-terminated PAMAM dendrimers encapsulating Pt nanoparticles containing of an average of 240 atoms (G6-OH(Pt_{240})) were prepared using a previously reported synthesis. Briefly, 240 equiv of Pt^{2+} from a freshly prepared, aqueous 100 mM K_2PtCl_4 solution were added to an aqueous 10.0 μM solution of G6-OH. This solution was stirred for 3.0 days to allow complexation of Pt^{2+} to

tertiary amines within the dendrimer.[5] This G6-OH$(Pt^{2+})_{240}$ complex was reduced for 24.0 h in a tightly sealed vial using a ~10-fold molar excess of freshly prepared, aqueous 0.50 M $NaBH_4$. Finally, the DENs solution was dialyzed for 24.0 h into 4.0 L of Milli-Q water using a 12 kDa cutoff dialysis sack (Sigma-Aldrich).

Characterization. UV-vis absorption spectra were acquired using a Hewlett-Packard HP8453 spectrometer and quartz cuvettes having a pathlength of 0.10 cm. A 10.0 μM aqueous G6-OH solution was used for background subtraction.

Transmission electron microscopy (TEM) was carried out using a JEOL-2010F TEM operating at 200 kV. Samples were prepared by dropping the appropriate solution onto a 20 nm-thick, carbon-coated, 400-mesh Cu grid (EM Sciences, Gibbstown, NJ) supported on filter paper, and then drying in air. X-ray photoelectron spectroscopy (XPS) data were obtained using a Kratos Axis Ultra DLD spectrometer having a monochromatic Al Kα X-ray source. High-resolution spectra were collected at a pass energy of 20 eV, a resolution of 0.1 eV, and a dwell time of 1.00 s. Survey scans were collected at a pass energy of 160 eV, a resolution of 1 eV, and a dwell time of 1.00 s. XPS

samples were cut from the carbon paper used for the EXAFS measurements. To account for sample charging, the recorded binding energies were adjusted so that the energy of the carbon peak matched the previously measured value for the dendrimer (286.0 eV).[5] Peak fitting was performed using XPSPEAK software. Both the separation and the ratio of areas for the Pt $4f_{7/2}$ and $4f_{5/2}$ peaks were constrained to be equal for both the reduced and oxidized Pt species. A Shirley background was used while the peaks were 80% Lorentzian-20% Gaussian.

XAFS spectra were obtained at beamline X18B of the National Synchrotron Light Source at the Brookhaven National Laboratory using a custom-designed cell. More information about the cell is provided later in this section, and in the main text. The DENs were immobilized onto the working electrode by soaking electrochemically activated carbon paper (*vide infra*) overnight in a dialyzed, aqueous solution of Pt DENs. Once modified with DENs, the electrodes were rinsed and kept wet until use. All XAFS data were obtained in fluorescence mode using a Lytle detector, Soller slits, and a Ge filter. A reference Pt foil was measured between successive samples and used

for energy calibration and alignment. As many as 10 EXAFS scans of the Pt adsorption edge were collected and averaged to improve the signal-to-noise ratio.

The data were processed using the Athena program and fit using the FEFF6 theory and the Artemis program.[25,42-43] The fitting model was constructed using four variables (CN, Δr, ΔE_0, and σ^2) for each interaction (Pt-Pt, Pt-O, or Pt-C). The value of S_O^2 (0.84) was fixed to that of a Pt foil measured on the same beamline. The foil was fit over 4 shells to a perfect fcc lattice to obtain S_O^2. A typical analysis fit either 4 or 8 variables to the data which contained 10 independent data points. The initial choice of R_{bkg}, a background subtraction factor, was made during the data processing and finalized during the analysis stage due to the difficulty of correctly determining this parameter in the case of low Z absorbers. Fine tuning of its value was made by visual examination of the fit quality and inspection of the quantitative goodness of the fit; that is, the reduced χ^2 and R-factor reported by Artemis.

Electrochemical cells. Three distinct types of electrochemical cells were used in this work. Photographs of each cell are provided in Figure 6.1. The first type of

cell used is referred to as the "standard electrochemical cell" (Figure 6.1a). This cell is a cylindrical glass container, open at the top, and it has a volume of 20 mL. All three electrodes are inserted into the cell from the top. When a carbon paper electrode is used in this cell, a large area of the electrode is exposed to the electrolyte solution. However, the active electrochemical area is limited to that which has been rendered hydrophilic by electrochemical pretreatment. The electrochemical cell used to make the carbon paper hydrophilic is referred to hereafter as the "Teflon cell," and it is illustrated schematically in Scheme 6.1 and a photograph is provided in Figure 6.1b. This cell defines a geometric area of 3.1 cm^2 on the carbon paper working electrode.

The final electrochemical cell is referred to as the "XAFS cell", and it is shown in Figure 6.1c and illustrated in Scheme 6.2. This cell was used for all in-situ XAFS experiments. Alternative designs have been used by other groups.[32,34,44] As shown in Scheme 6.2, our cell design

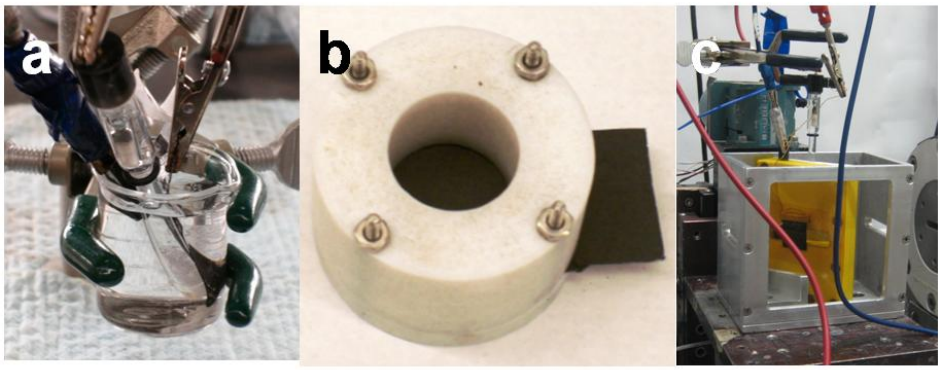

Figure 6.1. Photographs of the (a) standard electrochemical cell, (b) Teflon cell, and (c) XAFS cell.

Scheme 6.1

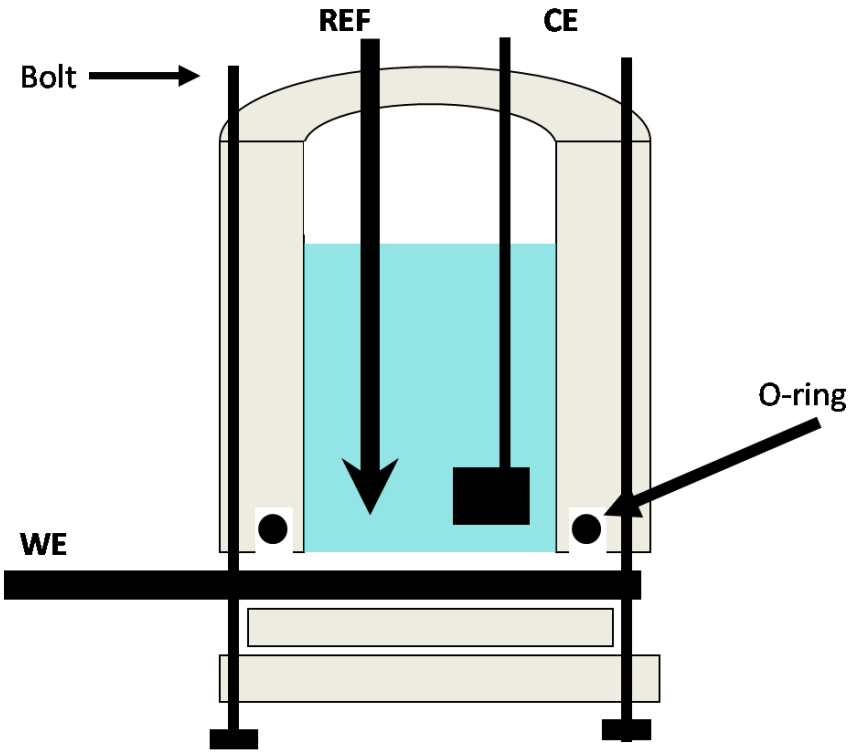

Scheme 6.2

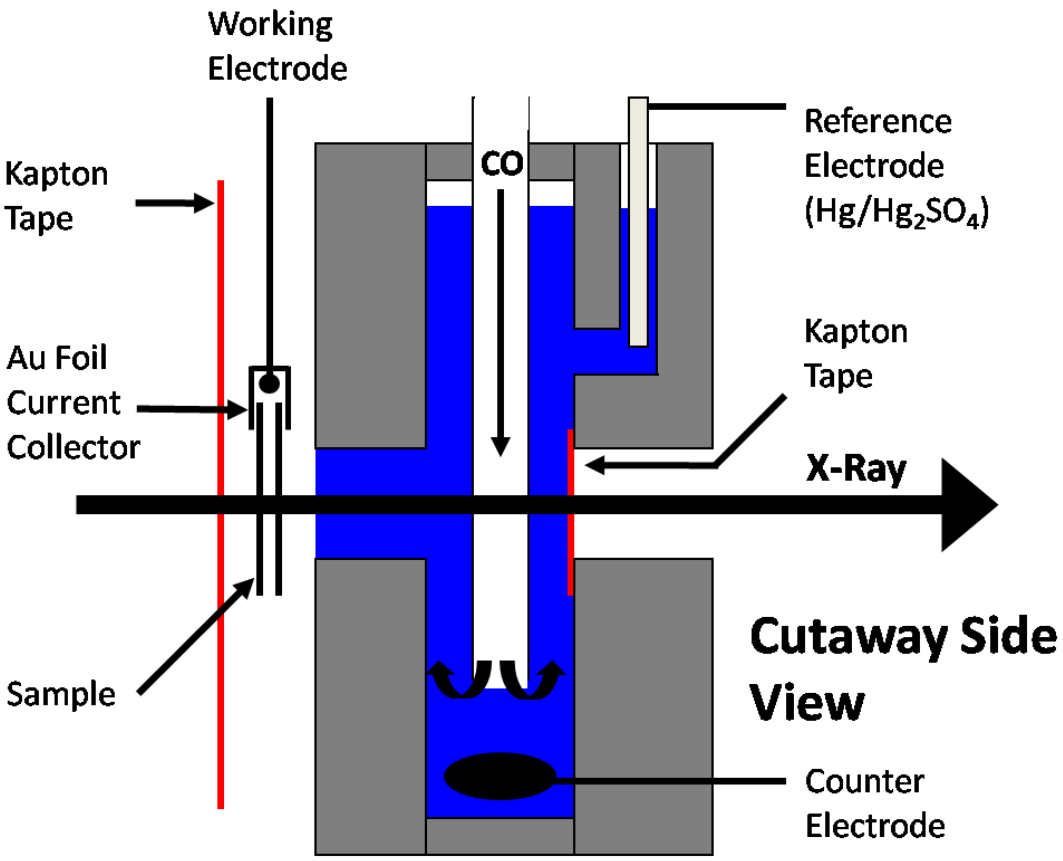
Working
Electrode
Kapton
Tape
Au Foil
Current
Collector
Sample
CO
Reference
Electrode
(Hg/Hg2SO4)
Kapton
Tape
X-Ray
Cutaway Side
View
Counter
Electrode

balances the requirements for electrochemical and XAFS measurements. In addition, this design provides for continuous gas sparging during the XAFS experiments without bubbles forming either on the electrode or near the XAFS window.

Electrochemistry. Unless specified otherwise, all electrochemistry experiments employed a Hg/Hg_2SO_4 reference electrode (CH Instruments, Austin, TX) and a glassy carbon counter electrode. All potentials are reported vs. the Hg/Hg_2SO_4 reference electrode. The standard electrochemical cell was used for experiments employing either the glassy carbon working electrode (GCE) or the Pt working electrode, as well as for CO oxidation scans using the carbon paper working electrode. Carbon paper pretreatment, cleaning scans, and H-adsorption experiments were performed in the Teflon cell.

Immobilization of Pt DENs on the GCE followed a previously reported procedure.[7-9] Briefly, The GCE was polished with 0.3 μm alumina, rinsed, dried with N_2, and then immersed in a cell containing 0.1 M $LiClO_4$, the dialyzed DENs solution, a Pt wire counter electrode, and a Hg/Hg_2SO_4 reference electrode. During immobilization, the

electrode potential was scanned from -0.2 to 0.7 V at 10 mV/s for 3 cycles. For the oxidation of CO in the standard cell, the working electrode (either a macroscopic Pt electrode, a Pt DENs-modified GCE, or a Pt DENs-modified carbon paper electrode) was first placed in a CO-saturated, 0.1 M $HClO_4$ solution. The potential of this electrode was stepped to -0.7 V and held there for 10 min. Next, N_2 was bubbled into the solution for 10 additional minutes while maintaining the electrode at -0.7 V. The electrode was then swept from -0.7 V to 0.8 V at 50 mV/s for 2 full cycles.

Electrochemical pretreatment of the carbon cloth, necessary to render it hydrophilic, followed a procedure previously reported by Godinez and coworkers.[45] Specifically, the potential of the carbon cloth was scanned 4 times between 1.0 V and -1.0 V at 100 mV/s in an aqueous 0.5 M H_2SO_4 electrolyte solution. These scans started and ended at 0.0 V, and the initial scan direction was negative. Figure 6.2 displays this CV. The first scan (red) exhibits low capacitance, indicating that the carbon paper is hydrophobic. As the electrode potential goes positive of

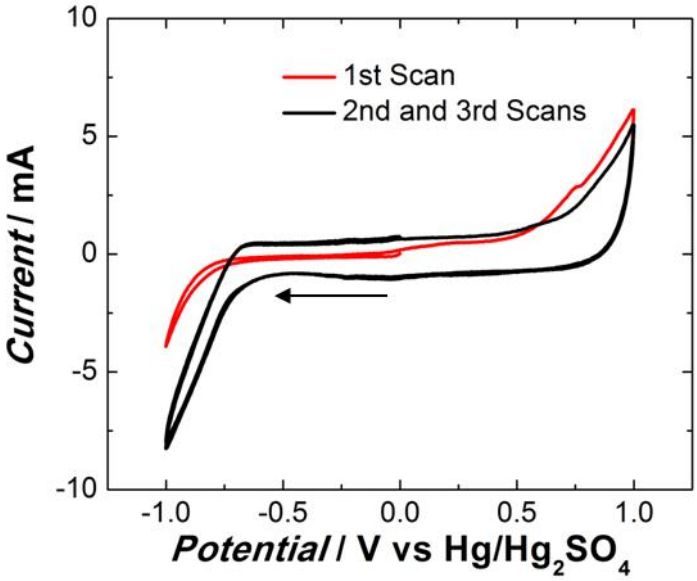

Figure 6.2. Cyclic voltammograms corresponding to the electrochemical pretreatment of the carbon paper electrode.

~0.5 V, the background capacitance increases dramatically, indicating that the carbon paper has become hydrophilic.

Following DEN immobilization, nanoparticle cleaning scans were performed by cycling the potential of the carbon cloth 10 times between 0.185 V and -0.715 V at 50 mV/s in an aqueous 0.1 M $HClO_4$ electrolyte solution. These scans started and ended at 0.0 V, and the initial scan direction was negative. Voltammetry in the hydrogen adsorption region was performed immediately following the cleaning scans. In this case, the scan rate was 50 mV/s and 3 cycles were recorded.

In-situ XAFS experiments were carried out in 0.1 M $HClO_4$ aqueous solutions, saturated with either N_2 or CO, using the XAFS cell. The electrolyte solutions were sparged with the appropriate gas for at least 10 min before placing the working electrode under potential control, and, unless otherwise specified, sparging continued throughout the time required to obtain XAFS spectra. The in-situ CO experiments started with a linear sweep from -0.2 V to -0.7 V at 10 mV/s, and then the potential was held at -0.7 V for the duration of the XAFS measurements. The cell was then purged with N_2 for 10 min to remove residual CO from the

solution. Adsorbed CO was oxidized by cycling the potential twice from -0.7 V to 0.8 V at 50 mV/s with no gas flowing. These scans began and ended at -0.7 V. The final XAFS spectrum was obtained at the open circuit potential (OCP) with no gas flowing.

6.4 Results and Discussion

DENs synthesis. Details regarding the synthesis of Pt DENs containing an average of 240 atoms (G6-OH(Pt_{240})) are provided in the Experimental Section and have been reported previously.[5-9] Briefly, however, $PtCl_4^{2-}$ was allowed to complex with an aqueous solution of G6-OH for 72 h. The resulting precursor complex (G6-OH(Pt^{2+})$_{240}$) was then reduced with BH_4^-. UV-vis spectra and TEM micrographs of the resulting DENs were consistent with previous reports and are shown in Figure 6.3. The DENs were purified by dialysis prior to electrochemical experiments.

Immobilization of DENs onto GCEs. Figure 6.4a shows cyclic voltammograms (CVs) obtained during immobilization of Pt DENs to a GCE.[8] The immobilization procedure consists of cycling the potential of the GCE from -0.2 V to 0.7 V

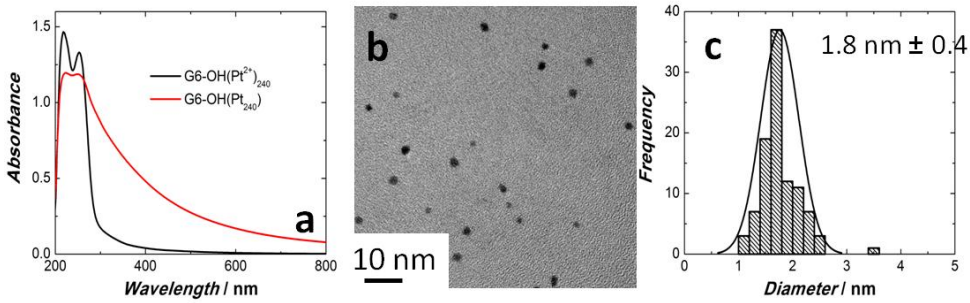

Figure 6.3. Characterization data for Pt DENs. (a) UV-vis spectra for both the precursor complex (G6-OH$(Pt^{2+})_{240}$) and the reduced G6-OH(Pt_{240}) DENs. (b) TEM micrograph of G6-OH(Pt_{240}) DENs. (c) Particle-size distribution histogram for G6-OH(Pt_{240}) DENs.

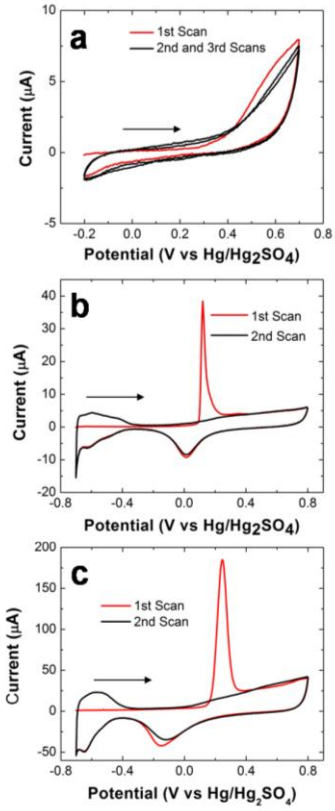

Figure 6.4. Cyclic voltammograms for (a) the immobilization of G6-OH(Pt_{240}) DENs to a GCE; (b) CO oxidation on a bulk, polycrystalline Pt electrode; and (c) CO oxidation on the DEN-modified GCE. The immobilization (a) was performed at 10 mV/s in a dialyzed 10 μM solution of G6-OH(Pt_{240}) DENs with 0.1 M $LiClO_4$ as electrolyte. The CO oxidation experiments (b & c) were performed at 50 mV/s in 0.1 M $HClO_4$. These experiments were performed in the standard electrochemical cell (see text for details about the cells used in this work).

three times. The first scan has a slightly higher anodic current, beginning at ~0.4V, compared to subsequent scans. We do not know how this observation correlates to the mechanism of DEN immobilization, but we have shown previously that it leads to a strong and irreversible link between the dendrimer and the GCE.[7-9]

CO oxidation. For comparison, CO oxidation experiments were performed on two different electrodes: bulk polycrystalline Pt and a DEN-modified GCE. Each electrode was immersed in a CO-saturated aqueous 0.1 M $HClO_4$ solution in the standard electrochemical cell (see the Experimental Section for the terminology used to identify the three different types of cells used in this work) for 10 min at -0.7 V, and then the electrolyte solution was purged with N_2. It has been previously reported that this treatment results in chemisorption of a CO monolayer.[19-21,24] Finally, the electrode potential was cycled twice from -0.7 to 0.8 V.

CVs for oxidation of CO on the polycrystalline Pt electrode are shown in Figure 6.4b. At the start of the first scan (red line, -0.7 V), the Pt surface is covered with CO and therefore no H-oxidation peaks are observed.

As the electrode is scanned to more oxidizing potentials (0.10 V), adsorbed CO is oxidized to CO_2 and then desorbs from the surface. At the highest potentials, the increased current results from oxidation of the Pt surface. On the return sweep, a small amount of Pt oxide is reduced at ~0.0 V, followed by the reductive adsorption of H^+ onto the Pt surface. The second cycle has many of the same features as the first, but it also shows a H-desorption peak at ~ -0.6 V and no CO oxidation peak. All of these observations are in accord with literature reports.[19-22,46]

The oxidation of CO on the Pt DENs-modified GCE (Figure 6.4c) displays features similar to those just described for the polycrystalline Pt electrode. However, consistent with previous reports, the CO oxidation peak is both broader and at a more positive potential for the DENs.[7] These observations are consistent with more heterogeneity in the CO binding sites for the DENs, compared to bulk Pt, and stronger adsorption of CO to the nanoparticles, respectively.[47] Similar findings have been reported for Pt nanoparticles in this size range prepared by other methods.[19] The H-adsorption region extends to slightly less positive potentials for the Pt DENs, indicating that H^+ is

harder to reduce on the DENs compared to a bulk Pt electrode. Additionally, for the polycrystalline Pt electrode, there are smaller features atop the broader current envelope in this potential region, which arise from both hydrogen and anion adsorption and desorption from specific crystal faces.[48-50] Finally, the Pt oxide reduction wave for the DENs is displaced ~ 200 mV negative compared to the bulk Pt electrode.[51]

The area under the CO oxidation peaks were integrated to estimate the total Pt surface area. As is customary for polycrystalline Pt surfaces,[20] we assumed a charge-per-unit-area of 420 μC/cm^2 for this calculation for both bulk Pt and Pt DENs. However, the corresponding value for Pt nanoparticles is unknown, and therefore the surface area estimate for the DENs must be considered within this context.[7] The true surface area for the bulk Pt electrode, measured using the data in Figure 6.4b, is 0.069 cm^2, and its geometric area is 0.032 cm^2. The ratio of measured area to geometric area, or roughness factor, is, therefore, 2.15, which is consistent with previous reports.[52-54] The surface area of the Pt DENs, measured using the data in Figure 6.4c, is 0.57 cm^2. The surface area of the Pt DENs

was estimated using several reasonable assumptions: a roughness factor of 2.4 for the GCE, one spherical nanoparticle per dendrimer, and a surface coverage of one dendrimer per 35 nm^2 of GCE surface area.[7] This calculation yields an estimated Pt surface area of 0.049 cm^2. The difference between the measured (0.57 cm^2) and estimated (0.049 cm^2) areas by an order of magnitude is similar to, but higher than, that observed in previous studies of Pt DENs.[7] We rationalize the difference in the ratios between this study and the previous report by considering the difference in electrode roughness and the electrode pretreatment.

Immobilization of DENs to a carbon paper electrode. G6-OH(Pt_{240}) DENs were immobilized onto a carbon paper electrode following a procedure reported by Godinez et al. and described in the Experimental Section.[45] Briefly, the hydrophobic carbon paper was rendered hydrophilic using an electrochemical pretreatment step in the Teflon cell. The carbon paper was then rinsed and immersed in a Pt DENs solution overnight, resulting in immobilization of the dendrimers. We speculate that oxygen-containing functional groups introduced onto the carbon surface by

electrochemical cycling provide sites for hydrogen bonding or electrostatic adsorption of dendrimers.[10,55]

Immobilization of Pt DENs onto the carbon paper was confirmed using cyclic voltammetry. Figure 6.5a compares CVs in the H-adsorption region for carbon cloth electrodes modified with empty G6-OH dendrimers and G6-OH(Pt_{240}) DENs. The CV for the empty dendrimers is featureless, except for a significant capacitive background, indicating an absence of catalytic activity. In contrast, the CV for the carbon paper electrode modified with Pt DENs exhibits significant catalytic activity for reduction of protons and subsequent oxidation of adsorbed H atoms. Additionally, there is a smaller feature at the extreme positive end of the scan range, which corresponds to formation of Pt oxide. These results confirm the presence of Pt DENs, and that the DENs are in electrical contact with the carbon paper working electrode.

The CV of the carbon paper modified with Pt DENs differs from the corresponding data for the GCE (Figure 6.4c, second scan) in that the former displays higher capacitance and a slightly sloped resistive background. These changes are ascribed to both the higher resistance of

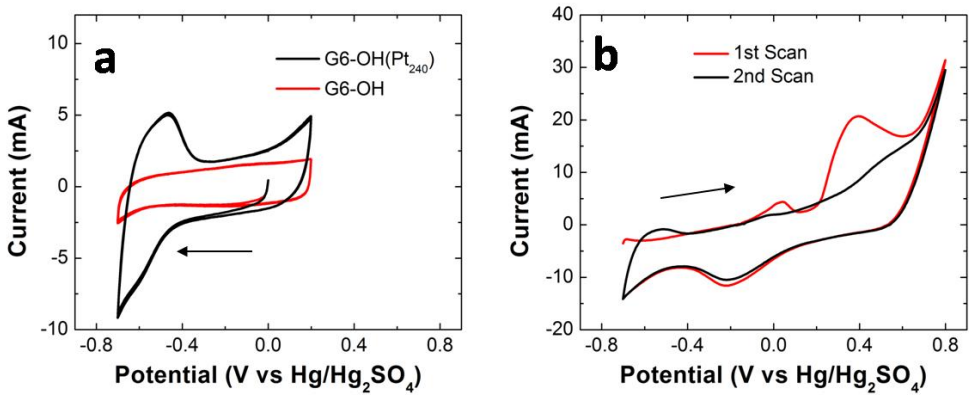

Figure 6.5. Cyclic voltammograms obtained in 0.1 M $HClO_4$ using a carbon paper working electrode. (a) A scan of the hydrogen adsorption region using an unmodified electrode (red line) and an electrode modified with G6-OH(Pt_{240}) DENs (black line) (scan rate = 50 mV/s). (b) The first (red line) and second (black line) scans of the CO oxidation region (scan rate = 50 mV/s). These experiments were performed in the standard electrochemical cell.

the carbon paper and its substantially higher surface area (~3.1 cm^2 geometric).

CO oxidation on a carbon paper electrode. Figure 6.5b shows a CV for CO oxidation on a Pt DEN-modified carbon paper electrode in the standard electrochemical cell. With the exception of the electrode materials, this experiment was performed using the same conditions described for the GCE (Figure 6.4c). The first scan in the positive direction displays the features anticipated by the results on the DEN-modified GCE: no H-oxidation (< -0.6 V), CO oxidation (~0.35 V), and Pt oxidation (> 0.6 V)). However, these major features are shifted positive and broadened by the resistance of the carbon paper electrode compared to the GCE. The resistance of the cell is also observed as a sloping background current. In addition to the expected features, there is a small peak in this CV at 0.05 V. It may be associated with an interaction between the carbon paper and the Pt DENs, and we have observed that it varies in intensity with both batch and thickness of carbon paper.

Upon reversal of the positive-going scan, reduction of Pt oxide is observed at ~-0.25 V, and there is a small peak for H adsorption at ~-0.7 V. Note that the CVs were

performed on different samples, so some variation in both the H-adsorption peaks and the capacitive background are expected due to differences in Pt DENs loading.

There is a small Pt-H oxidation peak present at ~-0.6 V in the second scan, but the CO oxidation peak is absent. These results are consistent with the data for the Pt DEN-modified GCE (Figure 6.4c). Note that the smaller anodic peak at 0.05 V is also not present in the second scan.

Electrochemistry. The in-situ electrochemical XAFS experiments require a highly specialized cell geometry (Scheme 6.2). This cell design evolved as a compromise between the need to simultaneously optimize the electrochemical and spectroscopic measurements, and therefore it is not ideal for either. More details about the cell design are included in the Experimental Section. The XAFS cell and XAFS experiments required slight changes to the procedure described earlier for CO adsorption to the Pt DENs. First, instead of initially stepping the potential from open circuit to -0.7 V, as was done for the experiments shown in Figure 6.5b, the electrode potential was swept from -0.2 to -0.7 V at 50 mV/s, and then held at -0.7 V. This was necessary because of the high surface

area of the electrode, and the corresponding need to maintain the maximum current passing through the cell below the limit defined by the potentiostat. In addition, to allow time for the XAFS spectra to be acquired, the potential was held at -0.7 V in the presence of CO for 4 h rather than 10 min.

The CV in Figure 6.6 shows the oxidation of CO in the XAFS cell. The electrochemical parameters used to obtain these data were identical to those described for Pt DENs on carbon paper in the smaller cell (Figure 6.5b). Note the prominent resistive background arising from the electrode material and cell geometry. The peaks in the CVs are also quite similar to those in Figure 2b, except they are broadened and shifted in potential (~0.4 V vs. ~0.6 V for Figures 6.5b and 6.6, respectively). Importantly, each feature of the ideal CO oxidation exhibited by the Pt DENs on a GCE (Figure 6.4c) is observed.

EXAFS analysis. Figure 6.7 shows the r-space data and fits for the Pt L_3 edge for each in-situ EXAFS experiment. The corresponding k-space data are provided in Figure 6.8. Parameters resulting from the fits, as well as the experimental conditions, are given in Table 6.1. Prior to

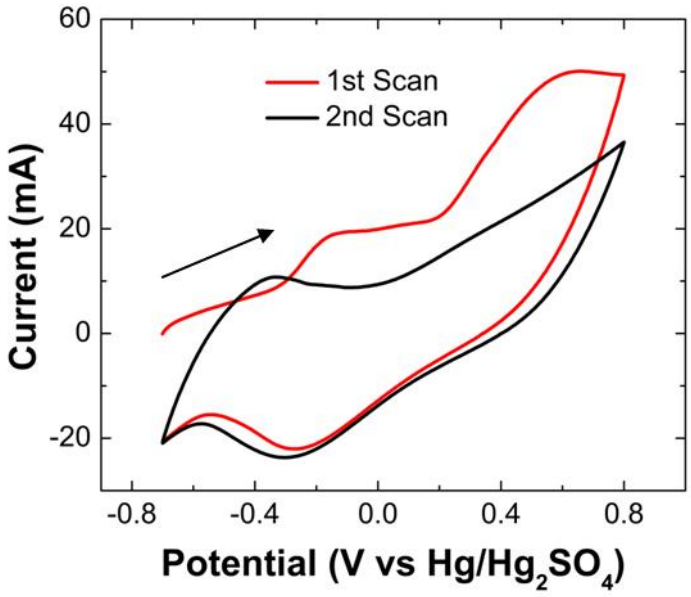

Figure 6.6. Cyclic voltammograms showing the first (red line) and second (black line) scans of the CO oxidation region for a G6-OH(Pt_{240}) DEN-modified carbon paper electrode using the in-situ EXAFS cell. The scan rate was 50 mV/s and the electrolyte was 0.1 M $HClO_4$.

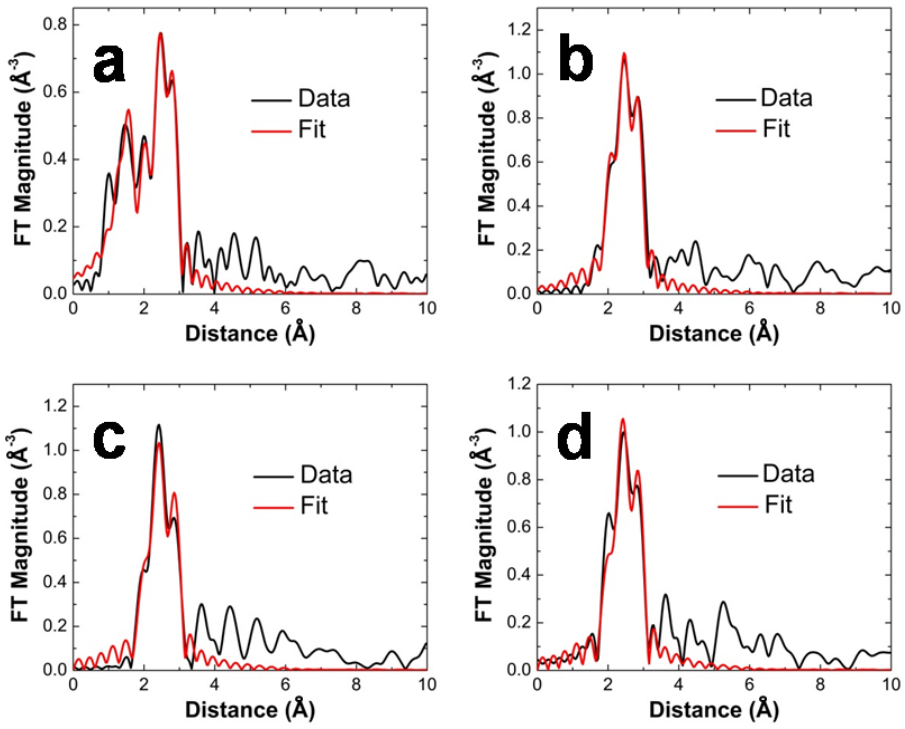

Figure 6.7. R-space data (black lines) and fitting analysis (red lines) for in-situ electrochemical XAFS experiments. The experiments were carried out at fixed potentials using a G6-OH(Pt_{240})-modified carbon cloth working electrode. The electrolyte was 0.1 M $HClO_4$. (a) air-saturated solution at open-circuit potential; (b) N_2-saturated solution, E = -0.7 V; (c) CO-saturated solution, E = -0.7 V; (d) air-saturated solution, open-circuit potential. See Table 6.1 and the text for a complete summary of the conditions used to obtain these results.

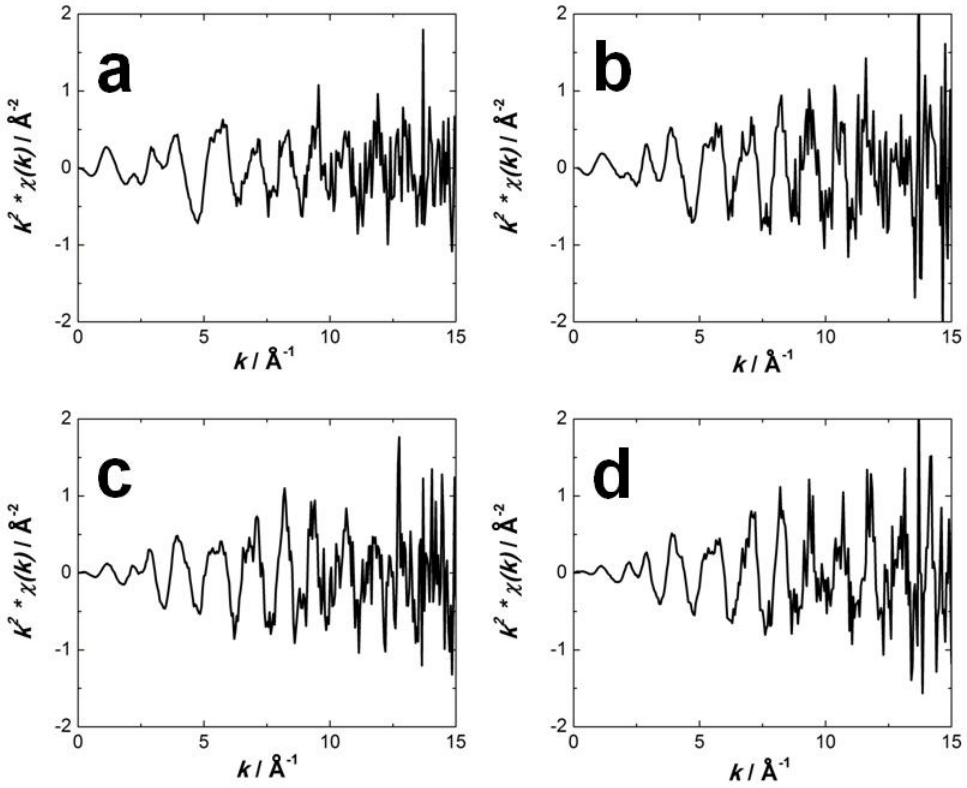

Figure 6.8. k-space data corresponding to the R-space data in Figure 6.7. These are included to demonstrate the data quality for EXAFS scans taken using the in-situ cell. The samples shown are for: (a) Experiment 1; (b) Experiment 2; (c) Experiment 3; and (d) Experiment 4. See main text and Table 6.1 for more information about these experiments.

Table 6.1. Experimental Conditions and EXAFS Fitting Results

Name	Gas sparge[a]	Potential (vs. Hg/Hg_2SO_4)	Pt-Pt CN	Pt-O CN	R_{bkg}
Experiment 1	None	OCP[b]	5.8 ± 1.3	1.6 ± 0.6	1.2
Experiment 2	N_2	-0.7	9.9 ± 1.1	[c]	1.8
Experiment 3	CO	-0.7	10.5 ± 1.5	[d]	1.8
Experiment 4	None	OCP[b]	8.9 ± 0.9	[d]	1.8

[a] This column indicates the gas that was used to sparge the solution during XAFS measurements. For Experiment 1, the solution was air-saturated, but not sparged. For Experiment 4, the solution was sparged with N_2 for 10 min prior to XAFS measurements, but during measurements the cell was open to the atmosphere.

[b] Open circuit potential

[c] A Pt-O contribution was barely detectable but not used for the fit. See text for more information.

[d] No Pt-O contribution was included in the fit.

sparging the solution with gas or placing the working electrode under potential control (Experiment 1, Table 6.1), the Pt-Pt CN is 5.8 ± 1.3. The corresponding EXAFS data and the theoretical fit are shown in Figure 6.7a. This CN allows estimation of the nanoparticle size by comparison with model compounds: bulk Pt (CN = 12), a 147 atom cuboctahedron (8.98), and a 309 atom cuboctahedron (9.63).[56-57] The measured CN is significantly lower than expected for a 240-atom particle (8.98 < CN < 9.63) but is consistent with that previously measured for G6-OH(Pt_{240}) DENs in the solid state (6.1 ± 0.4).[5] Additionally, the fit reveals a significant contribution from Pt-O (Figure 6.7b) indicating presence of unreduced Pt^{2+} surrounded by low Z neighbors (modeled by oxygen atoms), while the other experiments listed in Table 6.1 showed little or no contribution from Pt-O. The Pt-O CN for Experiment 1 is also consistent with previous measurements.[5] Note also that in the presence of multiple X-ray absorption sites (e.g., within the interior and on the surface of the nanoparticle, as in the case here) EXAFS can not discriminate between Pt-O and Pt-N bonds, or between different forms of oxygenated Pt, including Pt-OH_2, Pt-OH, and Pt-O: very well-defined model structures are required for such discrimination.[58]

Additionally, EXAFS measurements do not imply a chemical bond, but simply proximity. Because both the Pt-Pt and Pt-O CNs for Experiment 1 are consistent with previous results for bulk DEN samples, we conclude that there is no significant change induced in the DENs by the immobilization process or the presence of the electrolyte solution.

The EXAFS data for Experiment 2 (Table 6.1 and Figure 6.7b), which were obtained with the DEN-modified electrode under potential control (-0.7 V), were somewhat ambiguous as to whether a weak Pt-O contribution (CN = 0.26 ± 0.27) should be included. No Pt-O contribution is included in the fit shown in Figure 6.7b, but an alternative simulation, which does include this component, is shown in the Figure 6.9a. The decision to exclude a contribution from Pt-O is based on the XANES data shown in Figure 6.10. Figure 6.10a shows the difference in the white line intensity for a bulk Pt reference foil, a dried powder sample of the unreduced Pt^{2+}/dendrimer complex, and a dried powder sample of the reduced Pt DENs. The presence of oxidized Pt is clearly observed as an increase in the white line intensity of the red spectrum.[59] Figure 6.10b shows

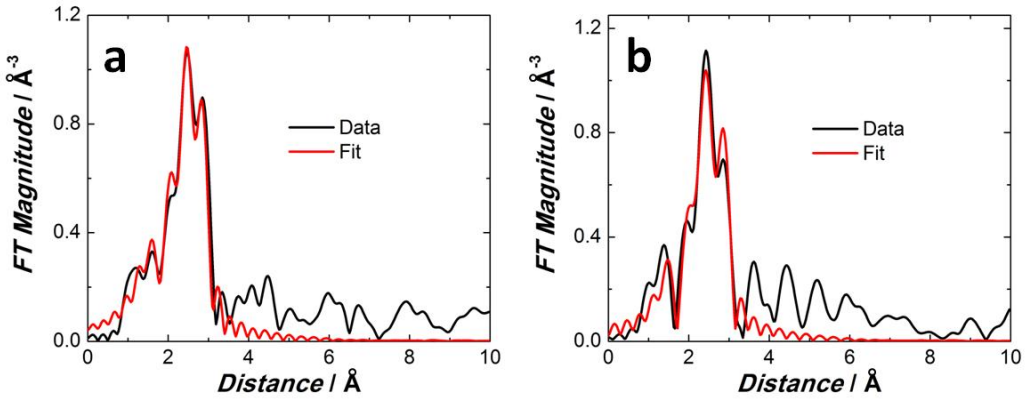

Figure 6.9. Alternative EXAFS analysis results (data and fits) for (a) the N_2 control experiment (Experiment 2 in the text and Table 1) and (b) the experiment with CO adsorbed to the Pt surface (Experiment 3). The data were analyzed with a low Rbkg (1.2) to allow for detection of the contributions from low Z neighbors which may be present in these experiments. Experiment 2 was fit with a Pt-O contribution, which resulted in coordination numbers (CNs) of 9.5 ± 1.2 for the Pt-Pt and 0.95 ± 0.61 for the Pt-O. The high relative uncertainty in the Pt-O CN led to comparison of the XANES data as discussed in the text. The fit for Experiment 3 included a Pt-C bond. The resulting CNs are 9.4 ± 1.7 for Pt-Pt and 0.36 ± 0.33 for Pt-C.

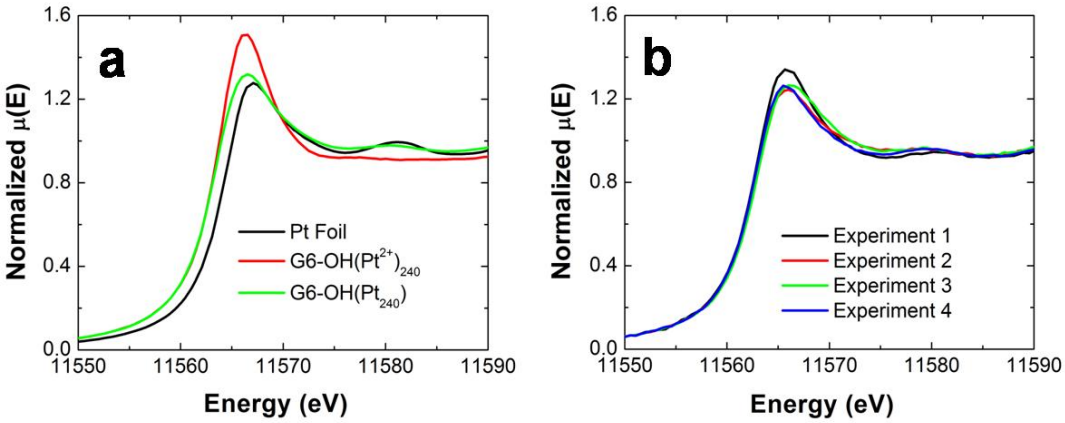

Figure 6.10. XANES spectra obtained for (a) dry, solid-state reference materials and (b) These experiments were carried out at fixed potentials using a G6-OH(Pt_{240})-modified carbon cloth working electrode. The electrolyte was 0.1 M $HClO_4$. (Black line, Experiment 1): air-saturated solution at open-circuit potential; (red line, Experiment 2): N_2-saturated solution, E = -0.7 V; (green line, Experiment 3): CO-saturated solution, E = -0.7 V; (blue line, Experiment 4) air-saturated solution, open-circuit potential. See Table 6.1 and the text for a complete summary of the conditions used to obtain these results.

the XANES data for the four experiments summarized in Table 6.1. Only the spectrum for Experiment 1 reveals this same sort of intensity increase, and therefore a contribution from Pt-O was used to fit just this one EXAFS spectrum.

The EXAFS analysis of Experiment 2 indicates a significantly higher Pt-Pt CN than was measured in Experiment 1 (9.9 ± 1.1 vs. 5.8 ± 1.3). Taking into consideration the error in the measurement, this CN is approximately that expected for a 240-atom particle. That is, cuboctahedral nanoparticles containing 147 and 309 atoms have CNs of 8.98 and 9.63, respectively. This result suggests that the application of a sufficiently negative electrode potential (-0.7 V in this case) leads to reduction of Pt^{2+} that was not originally reduced by BH_4^-. This finding is fully consistent with our previously reported model, which suggested that BH_4^- only reduces about 50% of the precursor complexes present in solution.[5]

Figure 6.7c shows EXAFS spectra for CO absorbed to the Pt DENs at an electrode potential of -0.7 V (Experiment 3, Table 6.1). The Pt-Pt CN (10.5 ± 1.5) is about the same as before CO adsorption (9.9 ± 1.1). Additionally, a weak contribution to the EXAFS signal, which is consistent with

an interaction between Pt and a low Z element (Figure 6.9b), was observed. The fitted bond length for this interaction (1.87 Å ± 0.04) matches that of Pt-CO.[33,60-61] While this interaction was not strong enough to be conclusive, we included it in the fit because its presence is anticipated based on the chemistry of the system.

The CO adlayer was removed by scanning the electrode potential twice from -0.7 V to 0.8 V, and then EXAFS data were acquired at open circuit (Experiment 4). The fit of the EXAFS spectrum (Figure 6.7d) reveals a Pt-Pt CN of 8.9 ± 0.9 (Table 1). This value is a little lower than that measured in the presence of CO but still consistent with a 240 atom nanoparticle.

Our CO adsorption and stripping results are in excellent agreement with those previously reported by Newton et al. for cycling of Pd nanoparticles in CO and NO gas.[62] Specifically, they used a combination of EXAFS and diffuse reflectance infrared spectroscopy, to show that Pd-Pd CNs were higher in the presence of CO. Yevick and Frenkel have recently proposed a quantitative modeling strategy that makes it possible to account for the surface disorder effect on EXAFS results for CNs in strained

nanoparticles.[63] They showed that enhanced surface disorder causes a reduction in the apparent metal-metal CN relative to ordered atomic arrangements of the same shape (e.g., in bare clusters vs. clusters passivated by H or CO). The Yevick-Frenkel model offers a plausible explanation for the apparent small increase (Table 6.1) in the Pt-Pt CN in the presence of surface-adsorbed CO. That is, CO may induce additional order in Pt DENs, which results in a more accurate measurement of their CN.

There are two more important findings that result from the EXAFS experiments. First, Pt DENs are fully reduced by application of an appropriate electrode potential. Second, once they are fully reduced, the DENs remain stable during adsorption and subsequent oxidation of CO. That is, it is absolutely clear that surface-immobilized DENs do not aggregate into bulk-like structures (CN = 12) during electrocatalytic oxidation of CO.

X-ray photoelectron spectroscopy (XPS). The Pt DEN-modified carbon paper was examined by XPS following the XAFS experiments to determine the oxidation state of the nanoparticles. A high-resolution XPS scan of the Pt 4f region of the spectrum, along with relevant peak fitting,

is shown in Figure 6.11. The positions of the main peaks (Pt $4f_{5/2}$ = 74.6 eV and Pt $4f_{7/2}$ = 71.3 eV) are consistent with our previously reported results for reduced Pt DENs (Pt $4f_{7/2}$ = 71.3 eV).[5] However, the small shoulders apparent at 75.9 and 72.6 eV in Figure 6.11 indicate the presence of a small amount of oxidized Pt. The full-width at half maximum for the peaks corresponding to fully reduced Pt (green line) is 0.8 eV. However, the peaks corresponding to oxidized Pt (Pt^{x+}, magenta line) are much broader: 1.75 eV and 1.40 eV for the $4f_{7/2}$ and $4f_{5/2}$ peaks, respectively. This suggests a distribution of oxidation states. The tail at higher binding energies is likely due to energy losses arising from interactions between photoelectrons and the dendrimer templates. The key point, however, is that all of the XPS data are consistent with the EXAFS results.

6.5 Summary and Conclusions

We have used in-situ electrochemical XAFS to investigate the structural properties of Pt DENs before, during, and after adsorption of CO. The results support our previous finding that reduction of the Pt^{2+}/dendrimer precursor complex with BH_4^- leads to a bimodal distribution of fully reduced and fully unreduced encapsulated Pt structures

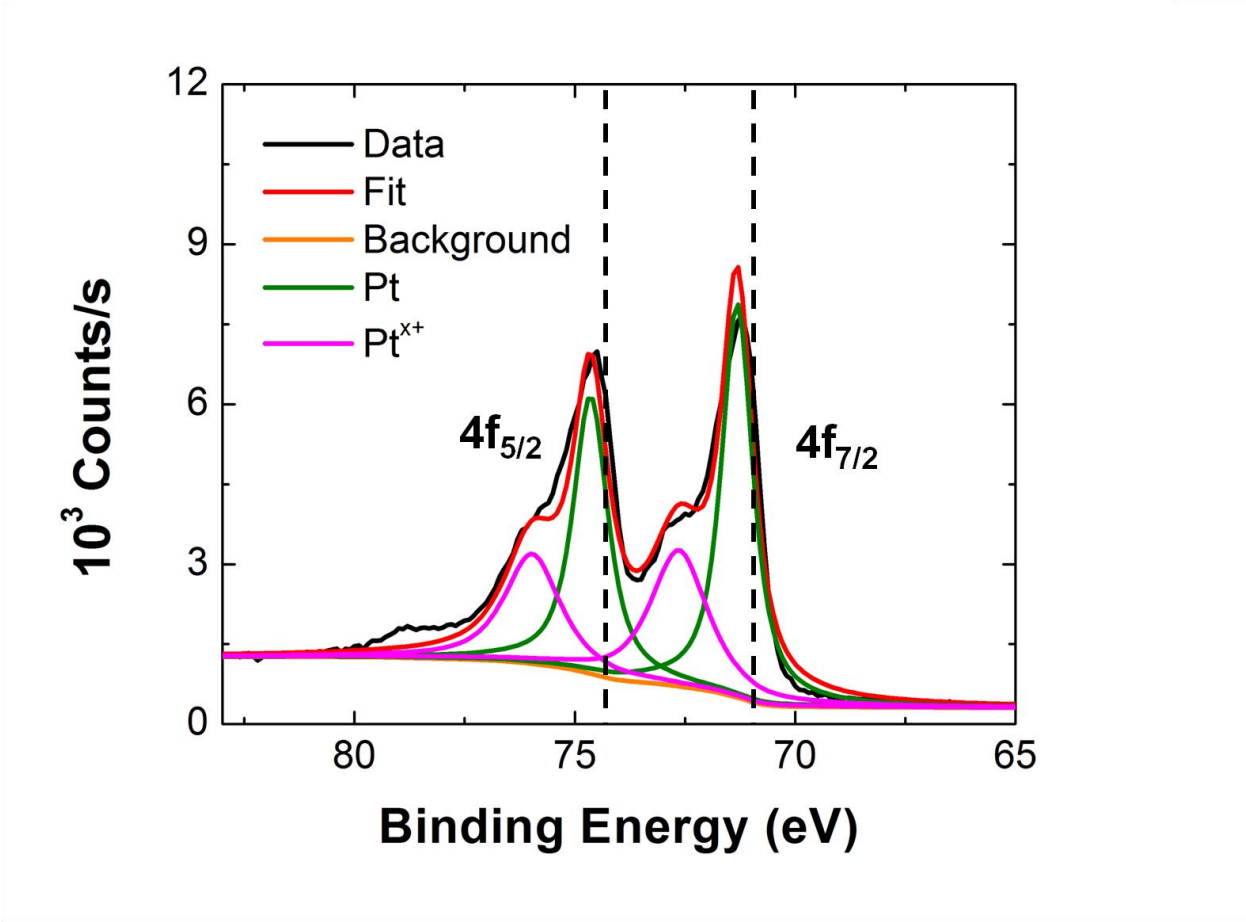

Figure 6.11. High-resolution XPS spectrum in the Pt 4f region for G6-OH(Pt_{240}) DENs. These data were obtained from a section of the electrode used for the XAFS data shown in Figure 6.7. The dashed lines represent the binding energies for zero-valent Pt ($4f_{7/2}$ = 71.2 eV, $4f_{5/2}$ = 74.5 eV). See text for a discussion of the peak fitting procedure.

(that is, a mixture of G6-OH(Pt_{240}) and G6-OH(Pt^{2+})$_{240}$).[5] This distribution is unchanged after passive immobilization of the dendrimers onto the electrode. However, when a negative potential is applied to the carbon-cloth electrode, the CN of the DENs increases from 5.8 to 9.9, indicating complete reduction of the G6-OH(Pt^{2+})$_{240}$ fraction on the electrode and hence conversion of the bimodal distribution to G6-OH(Pt_{240}). Finally, adsorption and desorption of CO onto the Pt DENs do not significantly change the particle structure, but there are some subtle changes that might result from adsorbate-driven ordering of the DENs. The important point, however, is that the presence of the dendrimer hosts stabilize the nanoparticles and prevent agglomeration.

The fact that the structure of DENs is stable on the electrochemical and XAFS time scale (hours) is important, because our objective is to correlate the structure of these materials to their electrocatalytic properties and to first principles calculations. Such correlations require that the size, composition, and structure of nanoparticles be well-defined and not change during the course of catalytic rate measurements. These types of studies are

presently underway in our lab, and the results will be reported in due course.

References

1. Jain, P. K.; Huang, X.; El-Sayed, I. H.; El-Sayed, M. A. *Acc. Chem. Res.* **2008**, *41*, 1578-1586.

2. Murray, R. W. *Chem. Rev.* **2008**, *108*, 2688-2720.

3. Tang, W. J.; Henkelman, G. *J. Chem. Phys.* **2009**, *130*.

4. Alexeev, O. S.; Siani, A.; Lafaye, G.; Williams, C. T.; Ploehn, H. J.; Amiridis, M. D. *J. Phys. Chem. B* **2006**, *110*, 24903-24914.

5. Knecht, M. R.; Weir, M. G.; Myers, V. S.; Pyrz, W. D.; Ye, H.; Petkov, V.; Buttrey, D. J.; Frenkel, A. I.; Crooks, R. M. *Chem. Mater.* **2008**, *20*, 5218-5228.

6. Scott, R. W. J.; Wilson, O. M.; Crooks, R. M. *J. Phys. Chem. B* **2004**, *109*, 692-704.

7. Ye, H.; Crooks, J. A.; Crooks, R. M. *Langmuir* **2007**, *23*, 11901-11906.

8. Ye, H.; Crooks, R. M. *J. Am. Chem. Soc.* **2005**, *127*, 4930-4934.

9. Ye, H.; Crooks, R. M. *J. Am. Chem. Soc.* **2007**, *129*, 3627-3633.

10. Vijayaraghavan, G.; Stevenson, K. J. *Langmuir* **2007**, *23*, 5279-5282.

11. Mark, S. S.; Bergkvist, M.; Yang, X.; Angert, E. R.; Batt, C. A. *Biomacromolecules* **2006**, *7*, 1884-1897.

12. Singh, A.; Chandler, B. D. *Langmuir* **2005**, *21*, 10776-10782.

13. Gu, Y.; Xie, H.; Gao, J.; Liu, D.; Williams, C. T.; Murphy, C. J.; Ploehn, H. J. *Langmuir* **2005**, *21*, 3122-3131.

14. Pellechia, P. J.; Gao, J.; Gu, Y.; Ploehn, H. J.; Murphy, C. J. *Inorg. Chem.* **2004**, *43*, 1421-1428.

15. Tarazona-Vasquez, F.; Balbuena, P. B. *J. Phys. Chem. A* **2007**, *111*, 945-953.

16. Tarazona-Vasquez, F.; Balbuena, P. B. *J. Phys. Chem. A* **2007**, *111*, 932-944.

17. Yamamoto, D.; Watanabe, S.; Miyahara, M. T. *Langmuir* **2009**.

18. Yamamoto, K.; Imaoka, T.; Chun, W.-J.; Enoki, O.; Katoh, H.; Takenaga, M.; Sonoi, A. *Nat. Chem.* **2009**, *1*, 397-402.

19. Arenz, M.; Mayrhofer, K. J. J.; Stamenkovic, V.; Blizanac, B. B.; Tomoyuki, T.; Ross, P. N.; Markovic, N. N. *J. Am. Chem. Soc.* **2005**, *127*, 6819-6829.

20. Gilman, S. *J. Phys. Chem.* **1962**, *66*, 2657-2664.

21. Maillard, F.; Eikerling, M.; Cherstiouk, O. V.; Schreier, S.; Savinova, E. R.; Stimming, U. *Faraday Discuss.* **2004**, *125*, 357-377.

22. Mayrhofer, K. J. J.; Blizanac, B. B.; Arenz, M.; Stamenkovic, V.; Ross, P. N.; Markovic, N. N. *J. Phys. Chem. B* **2005**, *109*, 14433-14440.

23. Andersson, K. J.; Calle-Vallejo, F.; Rossmeisl, J.; Chorkendorff, I. *J. Am. Chem. Soc.* **2009**, *131*, 2404-2407.

24. Maillard, F.; Schreier, S.; Hanzlik, M.; Savinova, E. R.; Weinkauf, S.; Stimming, U. *Phys. Chem. Chem. Phys.* **2005**, 7, 385-393.

25. Newville, M. *J. Synchrotron Rad.* **2001**, *8*, 322-324.

26. McBreen, J.; Mukerjee, S. *J. Electrochem. Soc.* **1995**, *142*, 3399-3404.

27. Mukerjee, S.; McBreen, J. *J. Electrochem. Soc.* **1999**, *146*, 600-606.

28. Mukerjee, S.; Urian, R. C.; Lee, S. J.; Ticianelli, E. A.; McBreen, J. *J. Electrochem. Soc.* **2004**, *151*, A1094-A1103.

29. Rose, A.; Crabb, E. M.; Qian, Y.; Ravikumar, M. K.; Wells, P. P.; Wiltshire, R. J. K.; Yao, J.; Bilsborrow, R.; Mosselmans, F.; Russell, A. E. *Electrochim. Acta* **2007**, *52*, 5556-5564.

30. Russell, A. E.; Maniguet, S.; Mathew, R. J.; Yao, J.; Roberts, M. A.; Thompsett, D. *J. Power Sources* **2001**, *96*, 226-232.

31. Russell, A. E.; Rose, A. *Chem. Rev.* **2004**, *104*, 4613-4636.

32. Wiltshire, R. J. K.; King, C. R.; Rose, A.; Wells, P. P.; Hogarth, M. P.; Thompsett, D.; Russell, A. E.. *Electrochim. Acta* **2005**, *50*, 5208-5217.

33. Maniguet, S.; Mathew, R. J.; Russell, A. E. *J. Phys. Chem. B* **2000**, *104*, 1998-2004.

34. McBreen, J.; O'Grady, W. E.; Pandya, K. I.; Hoffman, R. W.; Sayers, D. E. *Langmuir* **1987**, *3*, 428-433.

35. Mukerjee, S.; Srinivasan, S.; Soriaga, M. P.; McBreen, J. *J. Electrochem. Soc.* **1995**, *142*, 1409-1422.

36. Roth, C.; Benker, N.; Buhrmester, T.; Mazurek, M.; Loster, M.; Fuess, H.; Koningsberger, D. C.; Ramaker, D. E. *J. Am. Chem. Soc.* **2005**, *127*, 14607-14615.

37. Sasaki, K.; Zhang, L.; Adzic, R. R. *Phys. Chem. Chem. Phys.* **2008**, *10*, 159-167.

38. Scott, F. J.; Mukerjee, S.; Ramaker, D. E. *J. Electrochem. Soc.* **2007**, *5*, A396-A406.

39. Scott, F. J.; Roth, C.; Ramaker, D. E. *J. Phys. Chem. C* **2007**, *111*, 11403-11413.

40. Teliska, M.; O'Grady, W. E.; Ramaker, D. E. *J. Phys. Chem. B* **2004**, *108*, 2333-2344.

41. Teliska, M.; O'Grady, W. E.; Ramaker, D. E. *J. Phys. Chem. B* **2005**, *109*, 8076-8084.

42. Ravel, B.; Newville, M. *J. Synchrotron Rad.* **2005**, *12*, 537-541.

43. Rehr, J. J.; Albers, R. C. *Rev. Mod. Phys.* **2000**, *72*, 621-654.

44. Malakhov, I. V.; Nikitenko, S. G.; Savinova, E. R.; Kochubey, D. I.; Alonso-Vante, N. *Nucl. Instrum. Meth. A* **2000**, *448*, 323-326.

45. Ledesma-Garcia, J.; Garcia, I. L. E.; Rodriguez, F. J.; Chapman, T. W.; Godinez, L. A. *J. Appl. Electrochem.* **2008**, *38*, 515-522.

46. Santiago, E. I.; Giz, M. J.; Ticianelli, E. A. *J. Solid State Electrochem* **2003**, 7, 607-613.

47. Mayrhofer, K. J. J.; Arenz, M.; Blizanac, B. B.; Stamenkovic, V.; Ross, P. N.; Markovic, N. M. *Electrochim. Acta* **2005**, *50*, 5144-5154.

48. Armand, D.; Clavilier, J. *J. Electroanal. Chem.* **1989**, *270*, 331-347.

49. Rodes, A.; Clavilier, J.; Orts, J. M.; Feliu, J. M.; Aldaz, A. *J. Electroanal. Chem.* **1992**, *338*, 317-338.

50. Taguchi, S.; Aramata, A. *J. Electroanal. Chem.* **1998**, *457*, 73-81.

51. Cherstiouk, O. V.; Simonov, P. A.; Zaikovskii, V. I.; Savinova, E. R. *J. Electroanal. Chem.* **2003**, *554-555*, 241-251.

52. Bard, A. J.; Faulkner, L. R. *Electrochemical Methods: Fundamentals and Applications*; 2nd ed. John Wiley & Sons, Inc.: Hoboken, NJ, 2001.

53. Aschauer, E.; Fasching, R.; Varahram, M.; Jobst, G.; Urban, G.; Nicolussi, G.; Husinsky, W.; Friedbacher, G.; Grasserbauer, M. *J. Electroanal. Chem.* **1997**, *426*, 157-165.

54. Gilroy, D.; Conway, B. E. *Can J. Chemistry* **1968**, *46*, 875-890.

55. McCreery, R. L., *Carbon Electrodes: Structural Effects on Electron Transfer Kinetics*, in *Electroanalytical Chemistry: A Series of Advances*, A.J. Bard, Editor. 1991, Marcel Dekker: New York. p. 221-374.

56. Glasner, D.; Frenkel, A. I., *Geometrical characteristics of regular polyhedra: Application to EXAFS studies of nanoclusters*, in *XAFS 13, Proc. Int. Conf. X-ray Absorpt. Fine Struct.*, B. Hedman and P.

Painetta, Editors. 2007, Amer Inst Physics: Melville. p. 746-748.

57. Jentys, A. *Phys. Chem. Chem. Phys.* **1999**, *1*, 4059-4063.

58. Poverenov, E.; Efremenko, I.; Frenkel, A. I.; Ben-David, Y.; Shimon, L. J. W.; Leitus, G.; Marin, J. M. L.; Milstein, D. *Nature* **2008**, *255*, 1093-1096.

59. Yoshida, H.; Nonoyama, S.; Yazawa, Y.; Hattori, T. *Phys. Scripta* **2005**, *T115*, 813-815.

60. Ogletree, D. F.; Van Hove, M. A.; Somorjai, G. A. *Surf. Sci.* **1986**, *173*, 351-365.

61. Zhou, X.; Zhuang, G.; Chen, Y.; Kellar, S. A.; Moler, E. J.; Hussain, Z.; Shirley, D. A., *Determination of Adsorbed CO Molecular Orbital Positions by Photoelectron Diffraction*. 1998.

62. Newton, M. A.; Belver-Coldeira, C.; Martinez-Arias, A.; Fernandez-Garcia, M. *Nat. Mater.* **2007**, *6*, 528-532.

63. Yevick, A.; Frenkel, A. I. *Phys. Rev. B* **2010**, *81*, 115451-115457.

Chapter 7: Summary and Conclusions

This dissertation discusses the development of synthetic methods for preparing DENs and new characterization tools to determine their structure. The one technique central to this analysis is EXAFS. The Pt DENs system was described in Chapter 3. UV-vis spectroscopy, XPS, and EXAFS indicated that there was more than one reduction state for the Pt ion-dendrimer complex. Other techniques such as TEM and XRD-PDF detected nanoparticles of the expected, fully reduced size. The combination of information led to the hypothesis of a bimodal distribution of reduced nanoparticles and unreduced complexes.

Both Chapters 4 and 5 explained the characterization of bimetallic nanoparticles using EXAFS. The synthesis of PdAu nanoparticles by simultaneous reduction of the two metals was described in Chapter 4. This synthetic method resulted in an alloy structure. When extracting the nanoparticles from the protective dendrimer into an organic

phase using alkanethiols, the particles changed structure to a Au@Pd core-shell structure.

Chapter 5 focused on the sequential reduction of the two metals for the PdAu system. This synthetic method was found to form a Au@Pd core-shell structure, regardless of the order of reduction. Selective catalysis on Au of resazurin to resorufin was used to probe the surface structure of the nanoparticles. The catalytic results were consistent with the EXAFS results.

Chapter 6 described in-situ analysis of the Pt DENs system. An in-situ cell was developed to measure the structure of the Pt DENs during electrocatalytic oxidation of CO. The CO oxidation experiment was chosen for its control of the reaction rate on the time scale needed for EXAFS measurements (hours). The Pt DENs were found to fully reduce on the application of a reducting potential. Further, this reduced state was stable during the immobilization of CO on the Pt surface and its subsequent oxidation. This in-situ measurement identified the active catalytic structure for the Pt DENs system.

References

1. Zhao, M.; Sun, L.; Crooks, R. M. *J. Am. Chem. Soc.* **1998**, *120*, 4877-4878.

2. Scott, R. W. J.; Wilson, O. M.; Crooks, R. M. *J. Phys. Chem. B* **2005**, *109*, 692-704.

3. Foss, C. A., Jr.; Feldheim, D. L. *Metal Nanoparticles: Synthesis Characterization & Applications* Marcel Dekker: New York, 2002.

4. Vögtle, F.; Richardt, G.; Werner, N. *Dendrimer Chemistry: Concepts, Syntheses, Properties, Applications*. Wiley-VCH: Weinheim, 2009.

5. Liu, Y.; Bryantsev, V. S.; Diallo, M. S.; Goddard Iii, W. A. *J. Am. Chem. Soc.* **2009**, *131*, 2798-2799.

6. Tarazona-Vasquez, F.; Balbuena, P. B. *J. Phys. Chem. B* **2008**, *112*, 4172-4181.

7. Tarazona-Vasquez, F.; Balbuena, P. B. *J. Phys. Chem. B* **2008**, *112*, 4182-4193.

8. Sun, L.; Crooks, R. M. *J. Phys. Chem. B* **2002**, *106*, 5864-5872.

9. Tarazona-Vasquez, F.; Balbuena, P. B. *J. Phys. Chem. B* **2005**, *109*, 12480-12490.

10. Krot, K. A.; de Namor, A. F. D.; Aguilar-Cornejo, A.; Nolan, K. B. *Inorg. Chim. Acta* **2005**, *358*, 3497-3505.

11. Tran, M. L.; Gahan, L. R.; Gentle, I. R. *J. Phys. Chem. B* **2004**, *108*, 20130-20136.

12. Alexeev, O. S.; Siani, A.; Lafaye, G.; Williams, C. T.; Ploehn, H. J.; Amiridis, M. D. *J. Phys. Chem. B* **2006**, *110*, 24903-24914.

13. Diallo, M. S.; Christie, S.; Swaminathan, P.; Balogh, L.; Shi, X.; Um, W.; Papelis, C.; Goddard, W. A.; Johnson, J. H. *Langmuir* **2004**, *20*, 2640-2651.

14. Gomez, M. V.; Guerra, J.; Velders, A. H.; Crooks, R. M. *J. Am. Chem. Soc.* **2009**, *131*, 341-350.

15. Petkov, V.; Bedford, N.; Knecht, M. R.; Weir, M. G.; Crooks, R. M.; Tang, W.; Henkelman, G.; Frenkel, A. *J. Phys. Chem. C* **2008**, *112*, 8907-8911.

16. Xiangyang, S.; Su He, W.; Inhan, L.; Mingwu, S.; James, R. B., Jr. *Biopolymers* **2009**, *91*, 936-942.

17. Shi, X.; Wang, S. H.; Shen, M.; Antwerp, M. E.; Chen, X.; Li, C.; Petersen, E. J.; Huang, Q.; Weber, W. J.; Baker, J. R. *Biomacromolecules* **2009**, *10*, 1744-1750.

18. Lemon, B. I.; Crooks, R. M. *J. Am. Chem. Soc.* **2000**, *122*, 12886-12887.

19. Garcia-Martinez, J. C.; Scott, R. W. J.; Crooks, R. M. *J. Am. Chem. Soc.* **2003**, *125*, 11190-11191.

20. Garcia-Martinez, J. C.; Crooks, R. M. *J. Am. Chem. Soc.* **2004**, *126*, 16170-16178.

21. Templeton, A. C.; Wuelfing, W. P.; Murray, R. W. *Acc. Chem. Res.* **1999**, *33*, 27-36.

22. Knecht, M. R.; Garcia-Martinez, J. C.; Crooks, R. M.. *Langmuir* **2005**, *21*, 11981-11986.

23. Niu, Y.; Crooks, R. M. *Chem. Mater.* **2003**, *15*, 3463-3467.

24. Yeung, L. K.; Crooks, R. M. *Nano Lett.* **2000**, *1*, 14-17.

25. Kim, Y. G.; Oh, S. K.; Crooks, R. M. *Chem. Mater.* **2004**, *16*, 167-172.

26. Knecht, M. R.; Garcia-Martinez, J. C.; Crooks, R. M. *Chem. Mater.* **2006**, *18*, 5039-5044.

27. Knecht, M. R.; Crooks, R. M. *New J. Chem* **2007**, *31*, 1349-1353.

28. Satoh, N.; Nakashima, T.; Kamikura, K.; Yamamoto, K. *Nat. Nano* **2008**, *3*, 106-111.

29. Knecht, M. R.; Weir, M. G.; Myers, V. S.; Pyrz, W. D.; Ye, H.; Petkov, V.; Buttrey, D. J.; Frenkel, A. I.; Crooks, R. M. *Chem. Mater.* **2008**, *20*, 5218-5228.

30. Ozturk, O.; Black, T. J.; Perrine, K.; Pizzolato, K.; Williams, C. T.; Parsons, F. W.; Ratliff, J. S.; Gao, J.; Murphy, C. J.; Xie, H.; Ploehn, H. J.; Chen, D. A. *Langmuir* **2005**, *21*, 3998-4006.

31. Ye, H.; Crooks, R. M. *J. Am. Chem. Soc.* **2005**, *127*, 4930-4934.

32. Zhao, M.; Crooks, R. M. *Adv. Mater.* **1999**, *11*, 217-220.

33. Knecht, M. R.; Weir, M. G.; Frenkel, A. I.; Crooks, R. M. *Chem. Mater.* **2008**, *20*, 1019-1028.

34. Weir, M. G.; Knecht, M. R.; Frenkel, A. I.; Crooks, R. M. *Langmuir* **2009**.

35. Myers, S. V.; Frenkel, A. I.; Crooks, R. M. *Chem. Mater.* **2009**, *21*, 4824-4829.

36. Grohn, F.; Bauer, B. J.; Akpalu, Y. A.; Jackson, C. L.; Amis, E. J. *Macromolecules* **2000**, *33*, 6042-6050.

37. Gomez, M. V.; Guerra, J.; Myers, V. S.; Crooks, R. M.; Velders, A. H. *J. Am. Chem. Soc.* **2009**, *131*, 14634-14635.

38. Murray, R. W. *Chem. Rev.* **2008**, *108*, 2688-2720.

39. Wilson, O. M.; Knecht, M. R.; Garcia-Martinez, J. C.; Crooks, R. M. *J. Am. Chem. Soc.* **2006**, *128*, 4510-4511.

40. Bernechea, M. a.; de Jesus, E.; Lopez-Mardomingo, C.; Terreros, P. *Inorg. Chem.* **2009**, *48*, 4491-4496.

41. Carino, E. V.; Knecht, M. R.; Crooks, R. M. *Langmuir* **2009**, 25, 10279-10284.

42. Lang, H.; May, R. A.; Iversen, B. L.; Chandler, B. D. *J. Am. Chem. Soc.* **2003**, *125*, 14832-14836.

43. Lafaye, G.; Siani, A.; Marecot, P.; Amiridis, M. D.; Williams, C. T. *J. Phys. Chem. B* **2006**, *110*, 7725-7731.

44. Huang, W.; Kuhn, J. N.; Tsung, C.-K.; Zhang, Y.; Habas, S. E.; Yang, P.; Somorjai, G. A. *Nano Lett.* **2008**, *8*, 2027-2034.

45. Ye, H.; Crooks, J. A.; Crooks, R. M. *Langmuir* **2007**, *23*, 11901-11906.

46. Ye, H.; Crooks, R. M. *J. Am. Chem. Soc.* **2007**, *129*, 3627-3633.

47. Vijayaraghavan, G.; Stevenson, K. J. *Langmuir* **2007**, *23*, 5279-5282.

48. Shen, Y.; Xu, Q.; Gao, H.; Zhu, N. *Electrochem. Commun.* **2009**, *11*, 1329-1332.

49. Ye, H.; Scott, R. W. J.; Crooks, R. M. *Langmuir* **2004**, *20*, 2915-2920.

50. Garcia-Martinez, J. C.; Lezutekong, R.; Crooks, R. M. *J. Am. Chem. Soc.* **2005**, *127*, 5097-5103.

51. Hoover, N. N.; Auten, B. J.; Chandler, B. D. *J. Phys. Chem. B* **2006**, *110*, 8606-8612.

52. Narayanan, R.; El-Sayed, M. A. *J. Phys. Chem. B* **2004**, *108*, 8572-8580.

53. Niu, Y.; Yeung, L. K.; Crooks, R. M. *J. Am. Chem. Soc.* **2001**, *123*, 6840-6846.

54. Scott, R. W. J.; Wilson, O. M.; Oh, S.-K.; Kenik, E. A.; Crooks, R. M. *J. Am. Chem. Soc.* **2004**, *126*, 15583-15591.

55. Chandler, B. D.; Gilbertson, J. D. *Top. Organomet. Chem.* **2006**, *20*, 97-120.

56. Korkosz, R. J.; Gilbertson, J. D.; Prasfika, K. S.; Chandler, B. D. *Catal. Today* **2007**, *122*, 370-377.

57. Astruc, D. *Nanoparticles and Catalysis*; Wiley: New York, 2007.

58. Scott, R. W. J.; Ye, H.; Henriquez, R. R.; Crooks, R. M. *Chem. Mater.* **2003**, *15*, 3873-3878.

59. Mark, S. S.; Bergkvist, M.; Yang, X.; Angert, E. R.; Batt, C. A. *Biomacromolecules* **2006**, *7*, 1884-1897.

60. Zhu, H.; Zhu, Y.; Yang, X.; Li, C. *Chem. Lett.* **2006**, *35*, 326-327.

61. Tran, M. L.; Zvyagin, A. V.; Plakhotnik, T. *Chem. Commun.* **2006**, *2006*, 2400-2401.

62. Scott, R. W. J.; Datye, A. K.; Crooks, R. M. *J. Am. Chem. Soc.* **2003**, *125*, 3708-3709.

63. Scott, R. W. J.; Sivadinarayana, C.; Wilson, O. M.; Yan, Z.; Goodman, D. W.; Crooks, R. M. *J. Am. Chem. Soc.* **2005**, *127*, 1380-1381.

64. Wilson, O. M.; Scott, R. W. J.; Garcia-Martinez, J. C.; Crooks, R. M. *J. Am. Chem. Soc.* **2005**, *127*, 1015-1024.

65. Zheng, J.; Dickson, R. M. *J. Am. Chem. Soc.* **2002**, *124*, 13982-13983.

66. Zheng, J.; Petty, J. T.; Dickson, R. M. *J. Am. Chem. Soc.* **2003**, *125*, 7780-7781.

67. Zhao, M.; Crooks, R. M. *Angew. Chem., Int. Ed. Engl.* **1999**, *38*, 364-366.

68. Yeung, L. K.; Crooks, R. M. *Nano Lett.* **2001**, *1*, 14-17.

69. Pellechia, P. J.; Gao, J.; Gu, Y.; Ploehn, H. J.; Murphy, C. J. *Inorg. Chem.* **2004**, *43*, 1421-1428.

70. Lippard, S. J.; Berg, J. M. *Principals of Bioinorganic Chemistry*; 1 ed.; University Science Books: Mill Valley, California, 1994.

71. Rochon, F. D.; Fleurent, L. *Inorg. Chim. Acta* **1988**, *143*, 81-87.

72. Fu, X.; Wang, Y.; Wu, N.; Gui, L.; Tang, Y. *J. Colloid Interface Sci.* **2001**, *243*, 326-330.

73. Eberhardt, W.; Fayet, P.; Cox, D. M.; Fu, Z.; Kaldor, A.; Sherwood, R.; Sondericker, D. *Phys. Rev. Lett.* **1990**, *64*, 780-783.

74. You, T.; Niwa, O.; Horiuchi, T.; Tomita, M.; Iwasaki, Y.; Ueno, Y.; Hirono, S. *Chem. Mater.* **2002**, *14*, 4796-4799.

75. Tokuhisa, H.; Zhao, M.; Baker, L. A.; Phan, V. T.; Dermody, D. L.; Garcia, M. E.; Peez, R. F.; Crooks, R. M.; Mayer, T. M. *J. Am. Chem. Soc.* **1998**, *120*, 4492-4501.

76. Newville, M. *J. Synchrotron Rad.* **2001**, *8*, 322-324.

77. Elding, L. I.; Olsson, L. F. *J. Phys. Chem.* **1978**, *82*, 69-74.

78. Cotton, F. A.; Wilkinson, G.; Murillo, C. A.; Bochmann, M. *Advanced Inorganic Chemistry*; Wiley: New York, 1999.

79. Tarazona-Vasquez, F.; Balbuena, P. B. *J. Phys. Chem. A* **2007**, *111*, 945-953.

80. Zhang, Y.; Guo, Z.; You, X.-Z. *J. Am. Chem. Soc.* **2001**, *123*, 9378-9387.

81. Baik, M.-H.; Friesner, R. A.; Lippard, S. J. *J. Am. Chem. Soc.* **2003**, *125*, 14082-14092.

82. Fanizzi, F. P.; Intini, F. P.; Maresca, L.; Natile, G. *J. Chem. Soc., Dalton Trans.* **1990**, 199.

83. Grantham, L. R.; Elleman, T. S.; Martin, D. S. *J. Am. Chem. Soc.* **1955**, 77, 2965-2971.

84. Creighton, J. A.; Eadon, D. G. *J. Chem. Soc., Faraday Trans.* **1991**, *87*, 3881-3891.

85. Wagner, C. D.; Riggs, W. M.; Davis, L. E.; Moulder, J. F. *Handbook of X-Ray Photoelectron Spectroscopy*; Perkin-Elmer Corporation: Chanhassen, MN, 1995.

86. Matsumoto, K.; Sakai, K.; Nishio, K.; Tokisue, Y.; Ito, R.; Nishide, T.; Shichi, Y. *J. Am. Chem. Soc.* **1992**, *114*, 8110-8118.

87. Wang, J. J.; Ying, G. P.; Zhang, J.; Wang, Z. B.; Gao, Y. Z. *Electrochim. Acta* **2007**, *52*, 7042-7050.

88. Rehr, J. J.; Albers, R. C.; Zabinsky, S. I. *Phys. Rev. Lett.* **1992**, *69*, 3397-3400.

89. Ravel, B.; Newville, M. *J. Synchroton Rad.* **2005**, *12*, 537-541.

90. Glasner, D.; Frenkel, A. I. *XAFS13 Conference Proceedings* **2007**, *882*, 746-748.

91. Egami, T.; Billinge, S. J. L. *Underneath the Bragg Peaks*; Pergamon Press: Amsterdam, 2003.

92. Singh, A.; Chandler, B. D. *Langmuir* **2005**, *21*, 10776-10782.

93. Tomalia, D. A.; Baker, H.; Dewald, J.; Hall, M.; Kallos, G.; Martin, S.; Roeck, J.; Ryder, J.; Smith, P. *Polym. J.* **1985**, *17*, 117-132.

94. Crooks, R. M.; Zhao, M.; Sun, L.; Chechik, V.; Yeung, L. K. *Acc. Chem. Res.* **2001** 34 181-190

95. Wilson, O. M.; Scott, R. W. J.; Garcia-Martinez, J. C.; Crooks, R. M. *Chem. Mater.* **2004** 16 4202-4202

96. Toshima, N.; Yonezawa, T. *New J. Chem.* 1998 1179-1201

97. Toshima, N.; Harada, M.; Yamazaki, Y.; Asakura, K. *J. Phys Chem.* **1992** 96 9927-9933

98. Mizukoshi, Y.; Fujimoto, T.; Nagata, Y.; Oshima, R.; Maeda, Y. *J. Phys. Chem. B* **2000** 104 6028-6032

99. Slocik, J. M.; Naik, R. R. *Adv. Mater.* **2006** 18 1988-1992

100. Pârvulescu, V. I.; Pârvulescu, V.; Endruschat, U.; Filoti, G.; Wagner, F. E., Kubel, C.; Richards, R. *Chem. Eur. J.* **2006** 12 2343-2357

101. Chen, M.; Kumar, D.; Yi, C.-W.; Goodman, D. W. *Science* **2005** 310 291-293

102. Ferrer, D.; Torres-Castro, A.; Gao, X.; Sepúlveda-Guzmán, S.; Ortiz-Méndez, U.; José-Yacamán, M. *Nano Lett.* **2007** 7 1701-1705

103. Lee, A. F.; Baddeley, C. J.; Hardacre, C.; Ormerod, R. M.; Lambert, R. M.; Schmid, G.; West, H. *J. Phys. Chem.* **1995** 99 6096-6102

104. Luo, K.; Wei, T.; Yi, C.-W.; Axnanda, S.; Goodman, D.

W. *J. Phys. Chem. B* **2005** 109 23517-23522

105. Mejfia-Rosales, S. J.; Fernandez-Navarro, C.; Perez-Tijerina, E.; Blom, D. A.; Allard, L. F.; Yacaman, M.-J. *J. Phys. Chem. C* **2007** 111 1256-1260

106. Shiraishi, Y.; Ikenaga, D.; Toshima, N. Aust. *J. Chem.* **2003** 56 1025-1029

107. Solsona, B. E.; Edwards, J. K.; Landon, P.; Carley, A. F.; Herzing, A.; Kiely, C. J.; Hutchings, G. J. *Chem. Mater.* **2006** 18 2689-2695

108. Villa, A.; Champione, C.; Prati, L. *Catal. Lett.* **2007** 115 113-136

109. Wang, D; Villa, A.; Porta, F.; Su, D.; Prati, L. *Chem. Commun.* **2006** 2006 1956-1958

110. Wei, T.; Wang, J.; Goodman, D. W. *J. Phys. Chem. C* **2007** 111 8781-8788

111. Wu, M.-L.; Chen, D.-H.; Huang, T.-C. *Langmuir* **2001** 17 3877-3883

112. Mizukoshi, Y.; Okitsu, K.; Maeda, Y.; Yamamoto, T. A.; Oshima, R.; Nagata, Y. *J. Phys. Chem. B* **1997** 101 7033-7037

113. Ge, Z.; Cahill, D. G.; Braun, P. V. *J. Phys Chem. B* **2004** 108 18870-18875

114. Harpeness, R.; Gedanken, A. *Langmuir* 2004 20 3431-

3434

115. Nath, S.; Praharaj, S.; Panigrahi, S.; Ghosh, S. K.; Kundu, S.; Basu, S.; Pal, T. *Langmuir* **2005** 21 10405-10408

116. Hu, J.-W.; Li, J.-F.; Ren, B.; Wu, D.-Y.; Sun, S.-G.; Tian, Z.-Q. *J. Phys. Chem. C* **2007** 111 1105-1112

117. Henglein, A. *J. Phys. Chem. B* **2000** 104 6683-6685

118. Boennemann, H.; Endruschat, U.; Tesche, B.; Ruffinska, A.; Lehmann, C. W.; Wagner, F. E.; Filoti, G.; Parvulescu, V.; Parvulescu, V. I. *Eur. J. Inorg. Chem.* **2000** 2000 819-822

119. Crespilho, F. N.; Zucolotto, V.; Brett, C. M. A.; Oliveira, O. N.; Nart, F. C. *J. Phys. Chem. B* **2006** 110 17478-17483

120. Lang, H.; Maldonado, S.; Stevenson, K. J.; Chandler, B. D. *J. Am. Chem. Soc.* **2004** 126 12949-12956

121. Lemon, B. I.; Crooks, R. M. *J. Am. Chem. Soc.* **2007** 129 3627-3633

122. Scott, R. W. J.; Wilson, O. M.; Crooks, R. M. *Chem. Mater.* **2004** 16 5682-5688

123. Slocik, J. M.; Naik, R.; Stone, M. O.; Wright, D. W. *J. Mater. Chem.* **2005** 15 749-753

124. Garcia, M. E.; Baker, L. A.; Crooks, R. M. *Anal.*

Chem. **1999** 71 256-258

125. Lee, W. I.; Bae, Y.; Bard, A. J. *J. Am. Chem. Soc.* **2004** 126 8358-8359

126. Kim, Y.-G.; Garcia-Martinez, J. C.; Crooks, R. M. *Langmuir* **2005** 21 5485-5491

127. Wang, D.; Imae, T.; Miki, M. *J. Colloid Interface Sci.* **2007** 306 222-227

128. Nashner, M. S.; Frenkel, A. I.; Adler, D. L.; Shapley, J. R.; Nuzzo, R. G. *J. Am. Chem. Soc.* **1997** 119 7760-7771

129. Frenkel, A. I. *Z. Kristallogr.* **2007**, 222 605-611

130. Sun, Y.; Frenkel, A. I.; Isseroff, R.; Shonbrun, C.; Forman, M.; Shin, K.; Koga, T.; White, H.; Zhang, L.; Zhu, Y.; Rafallovich, M. H.; Sokolov, J. C. *Langmuir* **2006** 22 807-816

131. Frenkel, A. I.; Nemzer, S.; Pister, I.; Soussan, L.; Harris, T.; Sun, Y.; Rafallovich, M. H. *J. Chem. Phys.* **2005** 123 184701

132. Sellers, H.; Ulman, A.; Schnidman, Y.; Eilers, J. E. *J. Am. Chem. Soc.* **1993** 115 9389-9401

133. Zamborini, F. P.; Gross, S. M.; Murray, R. W. *Langmuir* **2001** 17 481-488

134. Frenkel, A. I.; Stern, E. A.; Voronel, A.; Qian, M.;

Newville, M. *Phys. Rev. Lett.* **1993** 71 3485-3488

135. Frenkel, A. I.; Stern, E. A.; Voronel, A.; Heald, S. *Solid State Commun.* **1996** 99 67-71

136. Boyce, J. B.; Mikkelsen, J. C. *Phys. Rev. B* **1985** 31 6903-6905

137. Frenkel, A. I.; Machavariani, V. S.; Rubshtein, A.; Rosenberg, Y.; Voronel, A.; Stern, E. A. *Phys. Rev. B* **2000** 62 9364-9371

138. CRC Handbook of Chemistry and Physics, 87th ed.; Lide, D. R., Ed.; Taylor and Francis: New York, **2006**

139. Xu, W.; Kong, J. S.; Yeh, Y.-T. E.; Chen, P. *Nature Mater.* **2008**, *7*, 992-996.

140. Endo, T.; Yoshimura, T.; Esumi, K. *J. Colloid Interface Sci.* **2005**, *286*, 602-609.

141. Beakley, L. W.; Yost, S. E.; Cheng, R.; Chandler, B. D. *Appl. Catal. A* **2005**, *292*, 124-129.

142. Bustos, E. B.; Jimenez, M. G. G.; Diaz-Sanchez, B. R.; Juaristi, E.; Chapman, T. W.; Godinez, L. A. *Talanta* **2007**, *72*, 1586-1592.

143. Chung, Y.-M.; Rhee, H.-K. *Catal. Lett.* **2003**, *85*, 159.

144. Gilbertson, J. D.; Vijayaraghavan, G.; Stevenson, K. J.; Chandler, B. D. *Langmuir* **2007**, *23*, 11239-11245.

145. Hendricks, T. R.; Dams, E. E.; Wensing, S. T.; Lee, I. *Langmuir* **2007**, *23*, 7404-7410.

146. Pittelkow, M.; Brock-Nannestad, T.; Moth-Poulsen, K.; Christensen, J. B. *Chem. Commun.* **2008**, 2358-2360.

147. Auten, B. J.; Hahn, B. P.; Vijayaraghavan, G.; Stevenson, K. J.; Chandler, B. D. *J. Phys. Chem. C* **2008**, *112*, 5365-5372.

148. Ferrando, R.; Jellinek, J.; Johnston, R. L. *Chem. Rev.* **2008**, *108*, 845-910.

149. Mandal, S.; Mandale, A. B.; Sastry, M. *J. Mater. Chem.* **2004**, *14*.

150. Perez-Tijerina, E.; Pinilla, M. G.; Mejia-Rosales, S.; Ortiz-Mendez, U.; Torres, A.; Jose-Yacaman, M. *Faraday Discuss.* **2008**, *138*, 353-362.

151. Jose, D.; Jagirdar, B. R. *J. Phys. Chem. C* **2008**, *112*, 10089-10094.

152. Kan, C., Cai, W.;Li, C.; Zhang, L.; Hofmeister, H. *J. Phys. D: Appl. Phys.* **2003**, *36*, 1609-1614.

153. Ferrer, D.; Blom, D. A.; Allard, L. F.; Mejia, S.; Perez-Tijerina, E.; Jose-Yacaman, M. *J. Mater. Chem.* **2008**, *18*, 2442-2446.

154. Liu, H. B.; Pal, U.; Perez, R.; Ascencio, J. A. *J. Phys. Chem. B* **2006**, *110*, 5191-5195.

155. Hwang, B. J.; Sarma, L. S.; Chen, J.-M.; Chen, C. H.; Shih, S.-C.; Wang, G. R.; Liu, D. G.; Lee, J. F.; Tang, M. T. *J. Am. Chem. Soc.* **2005**, *127*, 11140-11145.

156. Harada, M.; Asakura, K.; Toshima, N. *J. Phys. Chem.* **1993**, *97*, 5103-5114.

157. Chen, C.-H.; Sarma, L. S.; Chen, J.-M.; Shih, S.-C.; Wang, G.-R.; Liu, D.-G.; Tang, M.-T.; Lee, J.-F.; Hwang, B.-J. *ACS Nano* **2007**, *1*, 114-125.

158. Davis, R. J.; Boudart, M. *J. Phys. Chem.* **1994**, *98*, 5471-5477.

159. Reifsnyder, S. N.; Lamb, H. H. *J. Phys. Chem. B* **1999**, *103*, 321-329.

160. Zhang, P.; Zhou, X.; Tang, Y.; Sham, T. K. *Langmuir* **2005**, *21*, 8502-8508.

161. Kim, Y. H.; Nakano, Y. *Water Res.* **2005**, *39*, 1324.

162. Tait, C. D.; Janecky, D. R.; Rogers, P. S. Z. *Geochim. Cosmochim. Acta* **1991**, *55*, 1253-1264.

163. Zhao, M.; Crooks, R. M. *Chem. Mater.* **1999**, *11*, 3379-3385.

164. Alvarez, M. M.; Khoury, J. T.; Schaaff, T. G.; Shafigullin, M. N.; Vezmar, I.; Whetten, R. L. *J. Phys. Chem. B* **1997**, *101*, 3706-3712.

165. Daniel, M. C.; Astruc, D. *Chem. Rev.* **2004**, *104*, 293-346.

166. Roldughin, V. I. *Russ. Chem. Rev. (Engl. Transl.)* **2000**, *69*, 821-843.

167. Link, S.; El-Sayed, M. A. *Int. Rev. Phys. Chem.* **2000**, *19*, 409.

168. Pande, S.; Crooks, R. M. **2010**, In Preparation.

169. Mulvaney, P. *Langmuir* **1996**, *12*, 788-800.

170. Bauer, C.; Abid, J.-P.; Girault, H. H. *Chem. Phys.* **2005**, *319*, 409-421.

171. Lim, I. S.; Pan, Y.; Mott, D.; Ouyang, J.; Njoki, P. N.; Luo, J.; Zhou, S.; Zhong, C.-J. *Langmuir* **2007**, *23*, 10715-10724.

172. Link, S.; Burda, C.; Wang, Z. L.; El-Sayed, M. A. *J. Chem. Phys.* **1999**, *111*, 1255-1264.

173. Quinten, M. *Appl. Phys. B* **2001**, *73*, 317-326.

174. Jentys, A. *Phys. Chem. Chem. Phys.* **1999**, *1*, 4059-4063.

175. Frenkel, A. I.; Frankel, S. C.; Liu, T. *Phys. Scr.* **2005**, *T115*, 721-723.

176. Karakashev, D.; Galabova, D.; Simeonov, I. *World J. Microbiol. Biotechnol.* **2003**, *19*, 233-238.

177. Chapin, K. C.; Lauderdale, T.-L., Manual of Clinical Microbiology (Editor: P. R. Murray), ASM Press, Washington, D. C., 2007.

178. Bueno, C.; Villegas, M. L.; Bertolotti, S. G.; Previtali, C. M.; Neumann, M. G.; Encinas, M. V. *Photochem. Photobiol.* **2002**, *76*, 385-390.

179. Guilbault, G. G.; Kramer, D. N. *Anal. Chem.* **1965**, *37*, 1219-1221.

180. Gao, F.; Wang, Y.; Goodman, D. W. *J. Am. Chem. Soc.* **2009**, *131*, 5734-5735.

181. Jain, P. K.; Huang, X.; El-Sayed, I. H.; El-Sayed, M. A. *Acc. Chem. Res.* **2008**, *41*, 1578-1586.

182. Tang, W. J.; Henkelman, G. *J. Chem. Phys.* **2009**, *130*.

183. Gu, Y.; Xie, H.; Gao, J.; Liu, D.; Williams, C. T.; Murphy, C. J.; Ploehn, H. J. *Langmuir* **2005**, *21*, 3122-3131.

184. Tarazona-Vasquez, F.; Balbuena, P. B. *J. Phys. Chem. A* **2007**, *111*, 932-944.

185. Yamamoto, D.; Watanabe, S.; Miyahara, M. T. *Langmuir* **2009**.

186. Yamamoto, K.; Imaoka, T.; Chun, W.-J.; Enoki, O.; Katoh, H.; Takenaga, M.; Sonoi, A. *Nat. Chem.* **2009**, *1*, 397-402.

187. Arenz, M.; Mayrhofer, K. J. J.; Stamenkovic, V.; Blizanac, B. B.; Tomoyuki, T.; Ross, P. N.; Markovic, N. N. *J. Am. Chem. Soc.* **2005**, *127*, 6819-6829.

188. Gilman, S. *J. Phys. Chem.* **1962**, *66*, 2657-2664.

189. Maillard, F.; Eikerling, M.; Cherstiouk, O. V.; Schreier, S.; Savinova, E. R.; Stimming, U. *Faraday Discuss.* **2004**, *125*, 357-377.

190. Mayrhofer, K. J. J.; Blizanac, B. B.; Arenz, M.; Stamenkovic, V.; Ross, P. N.; Markovic, N. N. *J. Phys. Chem. B* **2005**, *109*, 14433-14440.

191. Andersson, K. J.; Calle-Vallejo, F.; Rossmeisl, J.; Chorkendorff, I. *J. Am. Chem. Soc.* **2009**, *131*, 2404-2407.

192. Maillard, F.; Schreier, S.; Hanzlik, M.; Savinova, E. R.; Weinkauf, S.; Stimming, U. *Phys. Chem. Chem. Phys.* **2005**, 7, 385-393.

193. McBreen, J.; Mukerjee, S. *J. Electrochem. Soc.* **1995**, *142*, 3399-3404.

194. Mukerjee, S.; McBreen, J. *J. Electrochem. Soc.* **1999**, *146*, 600-606.

195. Mukerjee, S.; Urian, R. C.; Lee, S. J.; Ticianelli, E. A.; McBreen, J. *J. Electrochem. Soc.* **2004**, *151*, A1094-A1103.

196. Rose, A.; Crabb, E. M.; Qian, Y.; Ravikumar, M. K.; Wells, P. P.; Wiltshire, R. J. K.; Yao, J.; Bilsborrow, R.; Mosselmans, F.; Russell, A. E. *Electrochim. Acta* **2007**, *52*, 5556-5564.

197. Russell, A. E.; Maniguet, S.; Mathew, R. J.; Yao, J.; Roberts, M. A.; Thompsett, D. *J. Power Sources* **2001**, *96*, 226-232.

198. Russell, A. E.; Rose, A. *Chem. Rev.* **2004**, *104*, 4613-4636.

199. Wiltshire, R. J. K.; King, C. R.; Rose, A.; Wells, P. P.; Hogarth, M. P.; Thompsett, D.; Russell, A. E.. *Electrochim. Acta* **2005**, *50*, 5208-5217.

200. Maniguet, S.; Mathew, R. J.; Russell, A. E. *J. Phys. Chem. B* **2000**, *104*, 1998-2004.

201. McBreen, J.; O'Grady, W. E.; Pandya, K. I.; Hoffman, R. W.; Sayers, D. E. *Langmuir* **1987**, *3*, 428-433.

202. Mukerjee, S.; Srinivasan, S.; Soriaga, M. P.; McBreen, J. *J. Electrochem. Soc.* **1995**, *142*, 1409-1422.

203. Roth, C.; Benker, N.; Buhrmester, T.; Mazurek, M.; Loster, M.; Fuess, H.; Koningsberger, D. C.; Ramaker, D. E. *J. Am. Chem. Soc.* **2005**, *127*, 14607-14615.

204. Sasaki, K.; Zhang, L.; Adzic, R. R. *Phys. Chem. Chem. Phys.* **2008**, *10*, 159-167.

205. Scott, F. J.; Mukerjee, S.; Ramaker, D. E. *J. Electrochem. Soc.* **2007**, *5*, A396-A406.

206. Scott, F. J.; Roth, C.; Ramaker, D. E. *J. Phys. Chem. C* **2007**, *111*, 11403-11413.

207. Teliska, M.; O'Grady, W. E.; Ramaker, D. E. *J. Phys. Chem. B* **2004**, *108*, 2333-2344.

208. Teliska, M.; O'Grady, W. E.; Ramaker, D. E. *J. Phys. Chem. B* **2005**, *109*, 8076-8084.

209. Rehr, J. J.; Albers, R. C. *Rev. Mod. Phys.* **2000**, *72*, 621-654.

210. Malakhov, I. V.; Nikitenko, S. G.; Savinova, E. R.; Kochubey, D. I.; Alonso-Vante, N. *Nucl. Instrum. Meth. A* **2000**, *448*, 323-326.

211. Ledesma-Garcia, J.; Garcia, I. L. E.; Rodriguez, F. J.; Chapman, T. W.; Godinez, L. A. *J. Appl. Electrochem.* **2008**, *38*, 515-522.

212. Santiago, E. I.; Giz, M. J.; Ticianelli, E. A. *J. Solid State Electrochem* **2003**, *7*, 607-613.

213. Mayrhofer, K. J. J.; Arenz, M.; Blizanac, B. B.; Stamenkovic, V.; Ross, P. N.; Markovic, N. M. *Electrochim. Acta* **2005**, *50*, 5144-5154.

214. Armand, D.; Clavilier, J. *J. Electroanal. Chem.* **1989**, *270*, 331-347.

215. Rodes, A.; Clavilier, J.; Orts, J. M.; Feliu, J. M.; Aldaz, A. *J. Electroanal. Chem.* **1992**, *338*, 317-338.

216. Taguchi, S.; Aramata, A. *J. Electroanal. Chem.* **1998**, *457*, 73-81.

217. Cherstiouk, O. V.; Simonov, P. A.; Zaikovskii, V. I.; Savinova, E. R. *J. Electroanal. Chem.* **2003**, *554-555*, 241-251.

218. Bard, A. J.; Faulkner, L. R. *Electrochemical Methods: Fundamentals and Applications*; 2nd ed. John Wiley & Sons, Inc.: Hoboken, NJ, 2001.

219. Aschauer, E.; Fasching, R.; Varahram, M.; Jobst, G.; Urban, G.; Nicolussi, G.; Husinsky, W.; Friedbacher, G.; Grasserbauer, M. *J. Electroanal. Chem.* **1997**, *426*, 157-165.

220. Gilroy, D.; Conway, B. E. *Can J. Chemistry* **1968**, *46*, 875-890.

221. McCreery, R. L., *Carbon Electrodes: Structural Effects on Electron Transfer Kinetics*, in *Electroanalytical Chemistry: A Series of Advances*, A.J. Bard, Editor. 1991, Marcel Dekker: New York. p. 221-374.

222. Poverenov, E.; Efremenko, I.; Frenkel, A. I.; Ben-David, Y.; Shimon, L. J. W.; Leitus, G.; Marin, J. M. L.; Milstein, D. *Nature* **2008**, *255*, 1093-1096.

223. Yoshida, H.; Nonoyama, S.; Yazawa, Y.; Hattori, T. *Phys. Scripta* **2005**, *T115*, 813-815.

224. Ogletree, D. F.; Van Hove, M. A.; Somorjai, G. A. *Surf. Sci.* **1986**, *173*, 351-365.

225. Zhou, X.; Zhuang, G.; Chen, Y.; Kellar, S. A.; Moler, E. J.; Hussain, Z.; Shirley, D. A., *Determination of*

Adsorbed CO Molecular Orbital Positions by Photoelectron Diffraction. 1998.

226. Newton, M. A.; Belver-Coldeira, C.; Martinez-Arias, A.; Fernandez-Garcia, M. *Nat. Mater.* **2007**, *6*, 528-532.

227. Yevick, A.; Frenkel, A. I. *Phys. Rev. B* **2010**, *81*, 115451-115457.